Nonlinear Dynamics and Chaos of Tethered Satellite Systems

by

Melina S. Nixon

Department of Mechanical Engineering
McGill University, Montréal

November 1996

This thesis was submitted to the Faculty of Graduate Studies and Research in partial fulfilment of the requirements for the Master of Engineering degree.

0-612-29619-9

Dedicated to the memory of my grandparents

Abstract

The equations of motion of a tethered satellite system are highly nonlinear and should possess many interesting related features: yet its nonlinear dynamics has never been thoroughly investigated in previous works. This thesis analyzes the nonlinear dynamics of two-body tethered satellite systems using numerical tools of analysis such as phase plane plots. power spectral densities (PSD's). Poincaré sections and first Lyapunov exponents. as well as approximate analytical methods including the method of Melnikov. Motion in the stationkeeping phase wherein the tethered system is just a gravity gradient pendulum is studied. first considering pitch motion only, and then considering the coupled pitch and roll motions. Regions of regular (periodic or quasi-periodic) and chaotic motions exist in the planar system for orbits of nonzero eccentricity, and also in the coupled system for both the circular and elliptic orbit cases. The size of the chaotic region grows with eccentricity, or in the coupled motion. circular orbit case. with increasing values of the Hamiltonian. Chaotic libration. observed in the coupled motion cases. limits the regular libration region to a region smaller than simply the libration region of non-tumbling motion. Melnikov's method applied to the planar motion perturbed by roll (assumed to be small and harmonic). showed that such a system will always have chaotic motion near the separatrix. The deployment/retrieval phases are studied next. For a circular orbit. pitch stability is examined for varying exponential length rates: for the unstable cases. it is compared to an equivalent uniform length rate scheme. which showed better stability behaviour. Application of Melnikov's method to planar motion of slow exponential deployment in a slightly elliptic orbit showed that chaotic separatrix motion will occur if eccentricity is greater than a critical value. proportional to the exponential length rate constant. Approximate analytical methods applied to coupled motion of retrieval under a length

rate control law in a circular orbit. predicted well the characteristics of the pitch and roll limit cycles response.

Résumé

Les équations du mouvement d'un système de satellites cablés sont grandement non linéaires et devraient comprendre plusieurs caractéristiques intéressantes: pourtant, cette dynamique non linéaire n'a jamais été étudiée en détail dans de précédents travaux. Cette thèse analyse la dynamique non linéaire de systèmes composés de deux corps cablés satellisés en utilisant des méthodes numériques d'analyse telles que les diagrammes de phase, la densité de puissance spectrale, les coupes de Poincaré, les premiers exposants de Lyapunov ainsi que des méthodes analytiques d'approximation incluant la méthode de Melnikov. Le mouvement pendant la phase de maintien en position, pour lequel le système correspond à un simple pendule soumis au gradient de gravité, est étudié en considérant premièrement, le mouvement de tangage seulement, et deuxièmement, les mouvements couplés de roulis et lacet. Les régions correspondant aux mouvements réguliers (périodiques et quasi-périodiques) et celles correspondant aux mouvements chaotiques existent dans le cas d'un système plan pour des orbites d'eccentricité non nulle, et également dans le cas d'un système couplé pour des orbites circulaires ou elliptiques. La taille de la région chaotique augmente avec l'eccentricité ou, dans le cas d'un système couplé pour une orbite circulaire, avec les valeurs croissantes de l'Hamiltonien. L'oscillation chaotique, observée dans les cas de mouvement couplé, limite la region correspondant aux mouvements réguliers à une région plus petite que celle correspondant simplement au mouvement de non renversement. La méthode de Melnikov appliquée au mouvement plan perturbé par le roulis (supposé faible et harmonique), a montré qu'un tel système a toujours un comportement chaotique près de la séparatrice. Les phases de déploiement et de repliement sont étudiées par la suite. Pour une orbite circulaire, la stabilité en tangage est étudiée à travers le taux de variation exponentiel de la longueur: dans les

cas instables, la stabilité est comparée avec celle obtenue par le procédé équivalent de variation uniforme de longueur, qui montre un meilleur comportement de stabilité. L'utilisation de la méthode de Melnikov pour le mouvement plan d'un déploiement faiblement exponentiel dans le cas d'une orbite légèrement elliptique a montré que le mouvement chaotique près de la séparatrice se produit si l'eccentricité est plus grande qu'une valeur critique, proportionelle à la constante de taux de changement exponentiel de la longueur. Des méthodes analytiques d'approximation, appliquées au mouvement couplé de repliement contrôlé par le taux de variation de la longueur pour une orbite circulaire, ont correctement prédit les caractéristiques des cycles limites pour les réponses de roulis et de tangage.

Acknowledgements

I would like to sincerely thank first my research supervisor, Professor A. K. Misra. Working with him has been an invaluable experience, and this thesis would not have been possible without his enthusiasm and encouragement.

I thank my fellow graduate students, especially those at "550", for their help, discussion and camaraderie. I thank Bertrand Petermann for the French translation of the abstract.

I must finally express my gratitude to my husband and my parents for their constant support and confidence.

I acknowledge a Postgraduate Scholarship awarded by the Natural Sciences and Engineering Research Council of Canada.

Contents

List of Figures

List of Tables

Nomenclature

a : orbit semi-major axis

a : pitch limit cycle amplitude

b : uniform length rate constant

b : roll limit cycle amplitude

c : exponential length rate constant

$\bar{c}$: exponential length rate constant $\mathcal{O}(1)$

c_{cr} : c critical

C : centre of mass

C_H : dimensionless Hamiltonian, Eq.(2.36)

d : distance between reference trajectory and nearby trajectory in calculation of Lyapunov exponent

ϵ : orbit eccentricity

ϵ_{cr} : ϵ critical

E : Chapter 3, twice the dimensionless Hamiltonian $\hat{H}$

F : a function of ϵ and θ, Eq.(2.28)

g : Chapter 1, the acceleration on the equator at mean sea level on the Earth's surface (9.81 m/s^2)

G : universal gravitational constant

G : a function of ϵ and θ. Eq.(2.28)

H : Hamiltonian

$\hat{H}$: dimensionless Hamiltonian. Eq.(3.3)

$\bar{i}, \bar{j}, \bar{k}$: unit vectors associated with axes x, y, z

$\bar{i}_o, \bar{j}_o, \bar{k}_o$: unit vectors associated with axes x_0, y_0, z_0

k : for initial conditions. $\alpha(0) = \gamma(0) = k$. $\alpha'(0) = \gamma'(0) = 0$

K_α, K_γ : pitch and roll gains of length rate control law

ℓ : tether length

ℓ_{ref} : reference tether length

ℓ_f : final tether length

m_1 : mass from/to which tether is deployed/retrieved

m_2 : other end mass (constant)

m_t : tether mass

m : total mass of tethered system

m_e : equivalent mass defined by Eq.(2.14)

M : mass of the Earth

M : Melnikov function

n : Chapter 2. mean orbital angular rate

p : generalized momentum

P_{mn} : periodic solution with m pitch oscillations in n roll oscillations, or regular region associated with that periodic solution

q_i : generalized coordinate i

Q_i : generalized force i

$\bar{r}, r$: position vector, distance with respect to tethered system centre of mass

$\bar{R}, R$: position vector, distance with respect to centre of Earth

t : time.

T, T_{att}, T_{orb} : kinetic energy, attitude and orbital

v : velocity

V, V_{att}, V_{orb} : potential energy, attitude and orbital

W^s : stable manifold of saddle point

W^u : unstable manifold of saddle point

x, y, z : tethered system coordinate axes, defined in Figure 2.1

x_o, y_o, z_o : initial coordinate axes

x', y', z' : intermediate coordinate axes

α : pitch angle, in-plane rotation about x_o axis

α_e : equilibrium pitch angle

α_0 : average value of pitch in limit cycle oscillations

γ : roll angle, out-of-plane rotation about z' axis

γ_e : equilibrium roll angle

λ : First Lyapunov exponent

μ : Earth gravitational constant

ϕ : Section 4.4, phase angle of roll limit cycle with respect to pitch limit cycle

ρ_t : the mass per unit length of the tether

θ : true anomaly

τ : for a circular orbit signifies true anomaly (Section 4.4)

τ_0 : measure of distance along unperturbed separatrix orbit in method of Melnikov

ω : nondimensional frequency

ω : roll limit cycle nondimensional frequency

$\vec{\omega}$: the angular velocity of the tethered system expressed in x, y, z coordinate axes

Dot ($\dot{}$) and prime ($'$) indicate differentiation with respect to t and θ respectively.

Superscript asterisk (*) refers to the unperturbed separatrix orbit in the method of Melnikov

Chapter 1

Introduction

1.1 Space Tether Systems

1.1.1 Historical Development

The idea of tethers in space is a century old. Tsiolkovsky (1895) suggested connecting large bodies in space by a long thin string to provide gravity gradient stabilization. When the space program became a reality, tethers were first considered as a means of rescuing stranded astronauts (Starly and Adlhoch, 1963). Two tether experiments were carried out during the last two Gemini missions, where the Gemini spacecraft was separated from an Agena rocket by a 30 m tether (Lang and Nolting, 1967). In the first experiment the system was spun, to provide some artificial gravity; in the second, the system demonstrated passive gravity-gradient stabilization. However, the era of tethers in space began in earnest with Colombo et al. (1974), the first to seriously consider connecting heavy masses in space with a very long tether. Colombo proposed a 'Shuttle-borne Skyhook', a scientific satellite extended below the Shuttle to conduct low orbital altitude research. Colombo's proposal led to investigations into the potential uses, dynamics and design of the Tethered Satellite System (TSS), as well as of other space tethered systems. Detailed historical recounts of space tethered systems include those of von Tiesenhausen (1984) and Grossi (1986).

TSS-1, the maiden mission of the American/Italian TSS program, flew in 1992 but with a limited success. The subsatellite could be deployed from the Atlantis Shuttle only up to 250 meters instead of the planned 20 km; however, tether motion was successfully controlled. TSS-1R, the reflight mission took place in early 1996. Although the tether eventually snapped so retrieval could not occur, the full 20 km length of the tether had been reached and maintained for several hours allowing much dynamical information to be obtained. NASA flew SEDS (Small Expendable-Tether Deployment System) I and II, in 1993 and 1994 respectively, succeeding to deploy a probe from the second stage of an orbiting Delta II rocket to a distance of 20 km. Several sub-orbital tethered flights have also taken place. Of note are the Canadian endeavours OEDIPUS A and C (Observations of Electric-field Distributions in the Ionospheric Plasma – a Unique Strategy), involving 1 km long tethers, launched in 1989 and 1995 respectively. Several other tethered missions are planned for the near future.

1.1.2 Applications

The motivation behind the research on the dynamics, control, design and testing of various space tether systems are the potential applications, which make up a whole new means for space utilization. The proposed applications are great in number and in variety. They can be free flying tethered systems, or involve the Shuttle or Space Station. Some have already been tested in the trial flights that have taken place, as cited in the preceding section; others are near, or strictly far term in demonstrability.

The proposed applications of tethered systems in space are well reviewed by Bekey (1983), and in a detailed and complete summary of their study to 1989 included in the NASA *Tethers in Space Handbook* edited by Penzo and Ammann (1989). The following is a brief discussion of the general categories of the potential uses of space tethered systems, with some examples.

Scientific Uses: Scientific study of regions of the earth's atmosphere, ionosphere and magnetosphere, which are otherwise inaccessible, and gravimetric measurements would be possible via a probe tethered below the orbiting Shuttle or space platform (low orbital altitude research). Similarly towing an aerodynamic model at such altitudes would create a space-based "wind tunnel" providing aerothermodynamic conditions not achievable in ground-based facilities. In the long term, tethered penetrators could be launched from a spacecraft to collect samples from the surfaces of asteroids or Mars.

Electrodynamic Uses: The motion of an orbiting insulated conductive tether through the earth's magnetic field induces a voltage across the tether: an electric current will be drawn from the the ionospheric plasma through the tether. The tether becomes a highly efficient generator of electric power for on-board electronics, at the expense of orbital energy. Alternatively, feeding current through the tether from an on-board power supply such as a solar array, reverses the process such that the tether acts as a motor, producing a propulsive thrust without the use of propellants. In another application, the tether current could be modulated to generate low frequency radio waves, such that the tether acts as a worldwide communications antenna.

Artificial Gravity Uses: Tether end-masses experience the tether tension as artificial gravity, in either a gravity-gradient stabilized configuration along the local vertical (rotating about its centre of gravity once per orbit) or in a rotating configuration (rotating more rapidly than once per orbit). The level attainable increases with the distance from the centre of mass of the system, and rotation rate. Artificial gravity approaching a magnitude of 1 g could be created on the Space Station by extending a counterweight along the local vertical with a very long tether; or, more practically, by using a moderate tether length and inducing a slow spin about the centre of mass. In the long term, a spinning tethered system could provide an artificial gravity environment acceptable for manned interplanetary travel. A number of controlled gravity applications for laboratory or industrial space uses have also been proposed, often in conjunction with the Space Station.

<u>Transportation Uses:</u> By permitting momentum exchange to occur between two spacecraft, tethers could replace or reduce the need of propellants in orbital transfer maneuvers. In a tethered system stable along the local vertical in a circular orbit, the upper mass travels at an orbital circular velocity too fast for its altitude, while the lower mass travels at an orbital circular velocity too slow for its altitude . If the constraining tether is cut, the upper mass will enter an elliptic orbit with a higher apogee and the lower mass will enter an elliptic orbit with a lower perigee. Thus, to cite two applications of "tether propulsion", the Shuttle could boost a payload into a higher orbit while simultaneously deboosting itself back to Earth, or the Shuttle could be deboosted from the Space Station while simultaneously boosting the Station itself into a higher orbit.

<u>Constellations:</u> A tethered constellation is a collection of more than two masses in space connected by tethers in a stable configuration. Various constellations have been proposed, in either one, two or three dimensions, using different combinations of stabilizing forces. A space elevator (or crawler) running along the connecting tether between the Space Station and a platform is one proposed three-body application

of a one-dimensional, gravity-gradient-stabilized constellation. A two-dimensional, gravity-gradient and air-drag stabilized "fish-bone" constellation has also been proposed, where via tethers a number of platforms are separated but remain physically connected to the Space Station for ready access and common power supply.

1.2 Literature Review

The equations governing the attitude dynamics of tethered systems are highly nonlinear and promise a rich body of nonlinear and possibly chaotic dynamics. The attention of the previous investigations of tethered satellite systems (well reviewed to 1986 in the survey by Misra and Modi, 1987 and by Beletskii and Levin, 1993) usually has focussed on the *control* of the tethered systems dynamics, specifically the control of the unstable retrieval dynamics, rather than on the fundamental nonlinear dynamical behaviour. The following is a review of literature which is of significance to the *nonlinear* dynamics of two-body tethered satellite systems (such as the Shuttle-supported TSS). The dynamical model of interest considers only rotational motions (elastic oscillations of the tether are ignored), point-mass end bodies, a tether of negligible mass in the variable length phases, and ignores aerodynamic drag, but the motion remains complex, with nonlinear coupling between pitch and roll motions.

This literature review considers first the stationkeeping stage of operation, and the deployment and retrieval stages together afterwards. In the stationkeeping stage the tether length is constant, while it varies during deployment and retrieval.

1.2.1 Stationkeeping Phase

In the stationkeeping phase, the tethered system is just a gravity gradient pendulum, or a dumb-bell satellite, for which there does exist a fair amount of study of its nonlinear dynamics, often considered as a special case of the general gravity gradient satellite.

Hughes (1986) reviews well the work done on gravity gradient satellites in the 1960's. These studies used approximate analytical and numerical techniques for both the circular and elliptic orbit cases, for both planar (pitch motion only), and three-dimensional coupled motion. Of note is the work done by Brereton and Modi (1967) and Modi and Brereton (1969a, 1969b) who used Poincaré sections to study the limiting stability region and periodic solutions of the planar, elliptic orbit problem. Modi and Brereton (1968) and Modi and Shrivastava (1971a, 1972) also used Poincaré sections in the stability analyses of the Hamiltonian problem of coupled motion in a circular orbit and observed 'island' and 'ergodic' solutions within the region of guaranteed stability (non-tumbling motion) defined by zero-velocity curves. The coupled motion, elliptic orbit case was studied by Modi and Shrivastava (1971b) who presented stability plots showing allowable impulsive disturbances for non-tumbling motion. More recently, Melvin (1988a) generated analytically and numerically the nonlinear normal mode of the gravity gradient pendulum in a circular orbit. In Melvin (1988a, 1988b) numerical integrations of the equations of motion also revealed some solutions which, plotted on the unit sphere, appeared pathological or chaotic, for the cases of a circular orbit and a slightly elliptic orbit. No attempt was made to confirm that these solutions are indeed chaotic as is defined in the nonlinear dynamics literature.

The gravity gradient pendulum, as a special case of the gravity gradient satellite, has been studied for the *planar* problem from a modern nonlinear dynamics approach.

where analytical and numerical nonlinear dynamic analysis techniques are used to study the nature of motion, regular or chaotic. (Numerical tools such as spectral analysis, Poincaré sections, and Lyapunov exponents, and the analytical method of Melnikov have been applied to a variety of nonlinear engineering systems in the last fifteen years. Their application and interpretation are well explained in Moon (1992) or Lichtenberg and Lieberman (1990), for example).

Tong and Rimrott (1991a) generated Poincaré maps for planar motion for a variety of orbit eccentricities, and found chaotic regions for non-zero eccentricity. They also applied the analytical technique of Melnikov to the system: the conclusion, chaotic motion possible for non-zero eccentricity, although valid only for small eccentricity due to approximating limitations imposed by the analytical method, corroborated their numerical investigation.

Karasopoulos and Richardson (1992) and (1993), extended the former analysis by numerical methods, including Poincaré maps, bifurcation diagrams and Lyapunov exponents.

The effect of damping on the system was studied numerically by Tong and Rimrott (1991b) and by Melnikov's method by Tong and Rimrott (1993). For other variations of the basic planar system, Melnikov's Method has been applied by: Seisl and Stendl (1989) (aerodynamic drag), Koch and Bruhn (1989) (oblate central body) and Gray and Stabb (1993) (control). All these works are for *planar* motion.

Other than the Poincaré sections presented by Modi and Brereton (1968) and Modi and Shrivastava (1971a, 1972) as mentioned above, the techniques of modern nonlinear dynamics have not been previously used to study the *three-dimensional coupled* motion of the gravity gradient satellite. However such numerical techniques have been applied to the three-dimensional dynamics of spinning satellites (Cole and

Calico. 1992 and Guran. 1993).

1.2.2 Deployment and Retrieval

In the cases of tether deployment and retrieval. no extensive nonlinear analysis. in terms of the geometric viewpoint of nonlinear dynamics, has been carried out. Some phase plane plots for exponential length rate retrieval for the planar system in a circular orbit were included in the work of Fleurisson et al. (1993). Proposed control schemes such as the length rate control law of Monshi (1992) and Monshi et al. (1991) were found in numerical simulations to confine growth of pitch and roll motions during retrieval to limit cycles. which are particular to nonlinear systems. In Monshi (1992) and Monshi et al. (1991) approximate analytical methods were applied to pure in-plane and out-of-plane motions.

1.3 Objectives and Scope of the Thesis

This objective of this thesis is to explore the fundamental three-dimensional dynamical behaviour of tethered satellites. using various techniques of nonlinear dynamics analysis. The analysis uses primarily the modern numerical tools of nonlinear dynamics. with numerical integration of the governing equations of motion and presentation of phase plane plots. time histories. power spectral densities (PSD's). Poincaré sections and Lyapunov exponents. The analytical method of Melnikov is also applied as well as classical approximate analytical methods.

The thesis considers the attitude dynamics of a two-body tethered system whose centre of mass travels in a Keplerian orbit. Aerodynamic forces are ignored. The end masses are considered as point masses so that their three dimensional rigid body dynamics is ignored. The tether is considered to have negligible mass in the variable length analyses. The elastic oscillations are ignored and the tether is assumed to remain straight. Thus only the librational dynamics of the tethered system is considered.

All the three phases of operation, stationkeeping, deployment and retrieval are considered.

The stationkeeping case considers planar as well as three-dimensional coupled motion, in circular and elliptic orbits. The numerical tools as well as Melnikov's Method (for an idealization of the coupled system), are used to identify regular or chaotic motions. As discussed, such a nonlinear dynamics analysis has been carried out earlier for a system that is similar to a tethered system in the stationkeeping phase, i.e., for the gravity gradient pendulum, in the *planar* case, but not for the *three-dimensional* case.

The deployment/retrieval phases are also studied. For a circular orbit, considering planar motion only, pitch stability is examined for different exponential length rates by analysis of the fixed points and the phase plane, which has not been carried out previously in any systematic manner. For the unstable cases, the exponential length rate scheme is compared to an equivalent uniform length rate scheme, using time-histories and the phase plane. Melnikov's Method is applied to the case of slow exponential deployment in a slightly elliptic orbit to determine the condition for chaotic motion. Coupled three-dimensional motion in a circular orbit is considered next; the limit cycle motion which has previously been observed to occur in numerical simulations of controlled retrieval, is examined here for a given length rate law by application of approximate analytical methods to the coupled motion.

1.4 Organization of the Thesis

The equations of motion of the system are derived in the following Chapter. The stationkeeping case is analyzed in Chapter 3. The planar motion is examined first, for a circular orbit as well as for elliptic orbits with varying eccentricities. The coupled pitch and roll motion in circular and elliptic orbits is studied next in the same Chapter. Chapter 4 examines dynamics for various cases of the deployment and retrieval phases. Finally, Chapter 5 contains the conclusions and recommendations for future work.

Chapter 2

Dynamical Formulation

2.1 Introduction

This Chapter begins with a general description of the system under study and a statement of assumptions. Then after describing the kinematics, the kinetic and potential energy expressions are derived and the equations of motion are obtained using the Lagrangian procedure. A brief analysis of the Hamiltonian ends the chapter.

2.2 System Description

The two-body tethered satellite system considered in this thesis is shown in Figure 2.1. The two end-bodies are assumed to be point masses. The connecting tether is assumed to remain straight. The elastic oscillations of the tether (including twist) are neglected. Gravity is considered to be the only external force acting on the system. The centre of mass of the system is assumed to follow a Keplerian orbit.

At any instant, the tether has a length ℓ and corresponding mass m_t (constant during stationkeeping, variable during deployment/retrieval). The mass from/to which the tether is deployed/retrieved, denoted by m_1, thus also may depend on time: the other end-mass is denoted by m_2 and is constant.

The librational motion of the system is described by two rotations of the tether from the local vertical: a pitch angle α and a roll angle γ, given in that order in and out of the orbital plane, respectively.

The energy expressions and equations of motion of the system are known (e.g. Modi et al. (1982) for a circular orbit, Xu (1984) for an elliptic orbit and additionally accounting for elastic vibrations of the tether) but are rederived here for completeness. In this thesis the length rate is specified and thus is not considered a generalized coordinate when deriving the equations of motion.

2.3 Kinematics of the System

Referring again to Figure 2.1, the kinematics of the system can be described as follows.

The position of the centre of mass of the system C in its orbit around the Earth is defined by the true anomaly θ and the radial coordinate R_c. Two rotating coordinate systems are used with origin at the centre of mass of the system. The coordinate system x_o, y_o, z_o has x_o axis along the orbit normal, y_o axis radially outward away from the earth along the local vertical, and z_o axis along the local horizontal completing the right hand triad. The coordinate system x, y, z is obtained via the rotation α (pitch) about the x_o axis, yielding the axes x', y', z' followed by the rotation γ (roll) about the z' axis. At any instant, the y axis and the tetherline coincide. Rotation about the tether axis (yaw) is assumed to be of no consequence. The set of unit vectors associated with the axes x_o, y_o, z_o and x, y, z are $\bar{i}_o, \bar{j}_o, \bar{k}_o$ and $\bar{i}, \bar{j}, \bar{k}$, respectively.

The position vectors of masses m_1, m_2 and an elemental mass of the tether with respect to the centre of the earth, are respectively

$$\overline{R}_1 = \overline{R}_c + \overline{r}_1, \quad \overline{R}_2 = \overline{R}_c + \overline{r}_2, \quad \overline{R}_t = \overline{R}_c + \overline{r}_t . \tag{2.1}$$

Here, $\overline{R}_c$ is the position vector of the centre of mass of the system with respect to the centre of the earth, and $\overline{r}_1$, $\overline{r}_2$ and $\overline{r}_t$, respectively denote the position vectors of masses m_1, m_2 and an elemental mass of the tether, with respect to the centre of mass of the system.

$\overline{R}_c$ can be expressed as

$$\overline{R}_c = R_c \, \bar{j}_o . \tag{2.2}$$

By definition of the location of the centre of mass of a system, the following relation holds:

$$m_1 \, \overline{r}_1 + m_2 \, \overline{r}_2 + \int_{m_t} \overline{r}_t \, dm_t = 0 . \tag{2.3}$$

Referring to the x, y, z coordinate system, one has

$$\overline{r}_1 = -r_1 \, \bar{j}, \quad \overline{r}_2 = r_2 \, \bar{j} = (\ell - r_1) \, \bar{j}, \quad \overline{r}_t = r_t \, \bar{j} = (s - r_1) \bar{j} . \tag{2.4}$$

where r_1, r_2 and r_t are the magnitudes of the position vectors $\overline{r}_1$, $\overline{r}_2$, and $\overline{r}_t$, while the spatial variable s is measured along the tetherline from mass m_1 to an elemental mass of the tether. The magnitudes r_1 and r_2 can be solved for by substituting Eq. (2.4) into Eq. (2.3), and noting that $m_t = \rho_t \ell$, where ρ_t is the mass per unit length of the tether. Thus

$$\left[-m_1 \, r_1 + m_2(\ell - r_1) + \rho_t \int_o^\ell (s - r_1) ds \right] \bar{j} = 0 .$$

which yields

$$r_1 = \ell(m_2 + m_t/2)/m , \quad r_2 = \ell(m_1 + m_t/2)/m , \quad r_t = s - \ell(m_2 + m_t/2)/m . \tag{2.5}$$

with $m = m_1 + m_2 + m_t$, the total system mass.

The velocities of masses m_1, m_2 and an elemental mass of the tether with respect to the centre of the earth, are given by, respectively

$$\dot{\overline{R}}_1 = \dot{\overline{R}}_c + \dot{\bar{r}}_1, \quad \dot{\overline{R}}_2 = \dot{\overline{R}}_c + \dot{\bar{r}}_2, \quad \dot{\overline{R}}_t = \dot{\overline{R}}_c + \dot{\bar{r}}_t \,. \tag{2.6}$$

The velocity $\dot{\overline{R}}_c$ of the centre of mass of the system with respect to the centre of the earth, can be expressed as

$$\dot{\overline{R}}_c = \dot{R}_c\, \bar{j}_o + R_c\dot{\theta}\, \bar{k}_o \,. \tag{2.7}$$

where $\dot{\theta}$ is the orbital angular velocity.

The velocities of masses m_1, m_2 and an elemental mass of the tether, with respect to the centre of mass, $\dot{\bar{r}}_1$, $\dot{\bar{r}}_2$ and $\dot{\bar{r}}_t$, are respectively

$$\dot{\bar{r}}_1 = -\dot{r}_1\, \bar{j} + \bar{\omega} \times \bar{r}_1 \,. \tag{2.8}$$

$$\dot{\bar{r}}_2 = \quad \dot{r}_2\, \bar{j} + \bar{\omega} \times \bar{r}_2 \,. \tag{2.9}$$

$$\dot{\bar{r}}_t = \quad \dot{r}_t\, \bar{j} + \bar{\omega} \times \bar{r}_t \,. \tag{2.10}$$

Here $\bar{\omega}$ is the angular velocity of the system, expressed in the x, y, z system as

$$\bar{\omega} = (\dot{\theta} + \dot{\alpha}) \cos\gamma\; \bar{i} - (\dot{\theta} + \dot{\alpha}) \sin\gamma\; \bar{j} + \dot{\gamma}\; \bar{k} \,. \tag{2.11}$$

In determining $\dot{r}_1, \dot{r}_2$, and $\dot{r}_t$ using Eq. (2.5), one takes into account that although m_2 and total mass m are constant, $\dot{m}_t = \rho_t\dot{\ell} = m_t(\dot{\ell}/\ell)$, and $\dot{m}_1 = -\dot{m}_t$; one also recognizes that $\dot{s} = \dot{\ell}$.

2.4 Kinetic Energy of the System

The kinetic energy of the system is

$$\begin{aligned}
T &= T_1 + T_2 + T_t \\
&= \frac{1}{2} m_1 \dot{\overline{R}}_1 \cdot \dot{\overline{R}}_1 + \frac{1}{2} m_2 \dot{\overline{R}}_2 \cdot \dot{\overline{R}}_2 + \frac{1}{2} \int_{m_t} \dot{\overline{R}}_t \cdot \dot{\overline{R}}_t dm_t \\
&= \frac{1}{2} m_1 \left(\dot{\overline{R}}_c + \dot{\overline{r}}_1\right) \cdot \left(\dot{\overline{R}}_c + \dot{\overline{r}}_1\right) + \frac{1}{2} m_2 \left(\dot{\overline{R}}_c + \dot{\overline{r}}_2\right) \cdot \left(\dot{\overline{R}}_c + \dot{\overline{r}}_2\right) \\
&+ \frac{1}{2} \int_{m_t} \left(\dot{\overline{R}}_c + \dot{\overline{r}}_t\right) \cdot \left(\dot{\overline{R}}_c + \dot{\overline{r}}_t\right) dm_t \,.
\end{aligned}$$

That is.

$$\begin{aligned}
T = \frac{1}{2} \; m \quad & \dot{\overline{R}}_c \cdot \dot{\overline{R}}_c + \dot{\overline{R}}_c \cdot \left[m_1 \, \dot{\overline{r}}_1 + m_2 \, \dot{\overline{r}}_2 + \int_{m_t} \dot{\overline{r}}_t \, dm_t\right] \\
&+ \frac{1}{2} \left[m_1 \, \dot{\overline{r}}_1 \cdot \dot{\overline{r}}_1 + m_2 \, \dot{\overline{r}}_2 \cdot \dot{\overline{r}}_2 + \int_{m_t} \dot{\overline{r}}_t \cdot \dot{\overline{r}}_t \, dm_t\right] .
\end{aligned}$$

Since Eq. (2.3) holds, the second term is zero and

$$T = \frac{1}{2} \, m \, \dot{\overline{R}}_c \cdot \dot{\overline{R}}_c + \frac{1}{2} \left[m_1 \, \dot{\overline{r}}_1 \cdot \dot{\overline{r}}_1 + m_2 \, \dot{\overline{r}}_2 \cdot \dot{\overline{r}}_2 + \int_{m_t} \dot{\overline{r}}_t \cdot \dot{\overline{r}}_t \, dm_t\right] . \tag{2.12}$$

The first term is the orbital kinetic energy of the centre of mass, T_{orb}. Using Eq. (2.7), $T_{orb} = \frac{1}{2} \, m \left(\dot{R}_c^2 - R_c^2 \, \dot{\theta}^2\right)$. However the orbit has been assumed to be Keplerian and only the attitude dynamics, the motion of the system about the centre of mass and to which the second term in Eq.(2.12) is related, is of interest. Rewriting this term by substituting Eqs. (2.4) -(2.5) and Eqs. (2.8) -(2.11) into Eq.(2.12) and carrying out some algebra, one obtains:

$$T = T_{orb} + \frac{1}{2} \, m_e \, \ell^2 \left[(\dot{\theta} + \dot{\alpha})^2 \cos^2 \gamma + \dot{\gamma}^2\right] + \frac{1}{2} \left[m_1 (m_2 + m_t)/m\right] \dot{\ell}^2 \,. \tag{2.13}$$

where m_e is an equivalent mass dependent on time defined by

$$m_e = \left[m_1 (m_2 + m_t/3) + (m_t/3)(m_2 + m_t/4)\right]/m \tag{2.14}$$

2.5 Potential Energy of the System

The potential energy of the system arises due to the gravitational field of the earth and is given by

$$\begin{aligned} V &= -\mu\left[\frac{m_1}{|\overline{R}_1|}+\frac{m_2}{|\overline{R}_2|}+\int_{m_t}\frac{dm_t}{|\overline{R}_t|}\right] \\ &= -\mu\left[\frac{m_1}{|\overline{R}_c+\overline{r}_1|}+\frac{m_2}{|\overline{R}_c+\overline{r}_2|}+\int_{m_t}\frac{dm_t}{|\overline{R}_c+\overline{r}_t|}\right], \end{aligned}$$

where μ is the gravitational constant of the earth (i.e., product of the universal gravitational constant and the mass of the earth).

Now

$$\begin{aligned} \frac{1}{|\overline{R}_c+\overline{r}_1|} &= \left[\left(\overline{R}_c+\overline{r}_1\right)\cdot\left(\overline{R}_c+\overline{r}_1\right)\right]^{-\frac{1}{2}} = \left[R_c^2+2\,\overline{R}_c\cdot\overline{r}_1+\overline{r}_1\cdot\overline{r}_1\right]^{-\frac{1}{2}} . \\ &= R_c^{-1}\left[1+\frac{2\,\bar{j}_o\cdot\overline{r}_1}{R_c}+\frac{\overline{r}_1\cdot\overline{r}_1}{R_c^2}\right]^{-\frac{1}{2}} . \end{aligned} \tag{2.15}$$

where Eq. (2.2), $\overline{R}_c = R_c\,\bar{j}_o$, has been used. Expanding binomially the right hand side and ignoring third and higher powers of $|\overline{r}_1|/R_c$, one obtains

$$\frac{1}{|\overline{R}_c+\overline{r}_1|} = R_c^{-1}\left[1-\frac{\bar{j}_o\cdot\overline{r}_1}{R_c}-\frac{\overline{r}_1\cdot\overline{r}_1-3(\bar{j}_o\cdot\overline{r}_1)^2}{2\,R_c^2}\right] . \tag{2.16}$$

Substituting this expression and the corresponding expressions for $\frac{1}{|\overline{R}_c+\overline{r}_2|}$ and $\frac{1}{|\overline{R}_c+\overline{r}_t|}$ into Eq. (2.15) and rearranging, gives

$$\begin{aligned} V = &-\frac{\mu\,m}{R_c}-\frac{\mu}{R_c^2}\left[m_1\,\overline{r}_1+m_2\overline{r}_2+\int_{m_t}\overline{r}_t dm\right]\cdot\bar{j}_o \\ &+\frac{\mu}{2\,R_c^3}\left\{m_1\left[\overline{r}_1\cdot\overline{r}_1-3(\bar{j}_o\cdot\overline{r}_1)^2\right]+m_2\left[\overline{r}_2\cdot\overline{r}_2-3(\bar{j}_o\cdot\overline{r}_2)^2\right]\right. \\ &\left.+\int_{m_t}\left[\overline{r}_t\cdot\overline{r}_t-3(\bar{j}_o\cdot\overline{r}_t)^2\right]dm\right\}. \end{aligned} \tag{2.17}$$

The first term is the orbital potential energy of the centre of mass, V_{orb}. The second term is zero due to Eq. (2.3). The third term is found by substituting Eqs. (2.4)-(2.5), and the following relation for the unit vector $\bar{j}_o$ expressed in the x, y, z system:

$$\bar{j}_o = \cos\alpha \ \sin\gamma \ \bar{i} + \cos\alpha \ \cos\gamma \ \bar{j} - \sin\alpha \ \bar{k} \,. \tag{2.18}$$

Then, after some algebra, one obtains

$$V = V_{orb} + \frac{\mu}{2\,R_c^3} \, m_e \, \ell^2 \left[1 - 3\cos^2\alpha \ \cos^2\gamma\right] \,, \tag{2.19}$$

where m_e is given by Eq. (2.14), i.e., the same equivalent mass that appeared in the kinetic energy expression.

2.6 Equations of Motion

The Lagrange equation is used to obtain the equations of motion from the kinetic and potential energy expressions:

$$\frac{d}{dt}\left(\frac{\partial T}{\partial \dot{q}_i}\right) - \frac{\partial T}{\partial q_i} + \frac{\partial V}{\partial q_i} = Q_i \,, \tag{2.20}$$

where q_i are the generalized coordinates, and Q_i are the associated respective generalized forces resulting from the nonconservative external forces.

The generalized coordinates relevant to the attitude motion are α and γ. In the deployment/retrieval schemes considered in this thesis, ℓ is specified through an algebraic or differential equation and is not a generalized coordinate. The equations of motion governing pitch and roll are then found to be

$$\begin{aligned} \cos^2\gamma \ \Big\{(\ddot{\alpha} + \ddot{\theta}) \ &+ \ \left[2(\dot{\ell}/\ell)\left[m_1\left(m_2 + \tfrac{1}{2}\,m_t\right)/m\,m_e\right] - 2\,\dot{\gamma}\,\tan\gamma\right](\dot{\alpha} + \dot{\theta}) \\ &+ \ (3\,\mu/R_c^3)\,\sin\alpha\,\cos\alpha\Big\} = Q_\alpha/m_e\,\ell^2 \,, \end{aligned} \tag{2.21}$$

$$\begin{aligned} \ddot{\gamma} \ &+ \ 2(\dot{\ell}/\ell)\left[m_1\left(m_2 + \tfrac{1}{2}\,m_t\right)/m\,m_e\right]\dot{\gamma} \\ &+ \ \left[(\dot{\alpha} + \dot{\theta})^2 + (3\,\mu/R_c^3)\,\cos^2\alpha\right]\sin\gamma\,\cos\gamma = Q_\gamma/m_e\,\ell^2 \end{aligned} \tag{2.22}$$

Environmental effects and control torques are not considered in this thesis and thus Q_α and Q_γ are zero.

The independent variable can be changed from time t to true anomaly θ using the second and third of the following relations which hold for a Keplerian orbit.

$$R_c = a(1-\epsilon^2)/(1+\epsilon\cos\theta)\,. \tag{2.23}$$

$$\dot{\theta} = \left[(1+\epsilon\cos\theta)^2/(1-\epsilon^2)^{3/2}\right] n\,. \tag{2.24}$$

$$n = \left[GM/a^3\right]^{1/2}\,. \tag{2.25}$$

where ϵ, a and n are the orbit eccentricity, semi-major axis, and mean orbital angular rate, respectively. Then, Eqs.(2.21) and (2.22) transform to (with Q_α and $Q_\gamma = 0$),

$$\begin{aligned} \cos^2\gamma\ \{\alpha'' &- \left[2(\ell'/\ell)\left[m_1\left(m_2+\tfrac{1}{2}m_t\right)/m\,m_e\right] - 2\gamma'\tan\gamma - F\right](\alpha'+1) \\ &+ 3G\sin\alpha\cos\alpha\} = 0. \end{aligned} \tag{2.26}$$

$$\begin{aligned} \gamma'' &- \left[2(\ell'/\ell)\left[m_1\left(m_2+\tfrac{1}{2}m_t\right)/m\,m_e\right] - F\right]\gamma' \\ &- \left[(\alpha'+1)^2+3G\cos^2\alpha\right]\sin\gamma\cos\gamma = 0. \end{aligned} \tag{2.27}$$

where prime refers to differentiation with respect to θ, and F and G are functions of eccentricity ϵ and θ as follows:

$$F = 2\epsilon\sin\theta/(1+\epsilon\cos\theta), \quad G = 1/(1+\epsilon\cos\theta)\,. \tag{2.28}$$

The equations of motion of the two-body tethered system considered here are shown above in their most general form. During the stationkeeping phase of operation, the length of the tether is constant, i.e., $\ell' = 0$. During deployment and retrieval, the tether length varies with time along with the tether mass; to simplify the equations somewhat the tether mass is assumed negligible compared to m_1 and m_2. The equations are analyzed along with the equation specifying the length rate.

The equations of motion remain, even with such simplifications, non-autonomous for eccentric orbits, and highly nonlinear, including nonlinear coupling of in-plane and out-of-plane motions. Thus, an analytical exact solution can be obtained only for a very special case. As described in Chapter 1, some approximate nonlinear analysis is carried out in the thesis, but mostly numerical solutions of different cases of the above equations are obtained.

2.7 Hamiltonian of the System

The Hamiltonian H of a dynamic system is constant if there are no nonconservative external forces and time does not appear explicitly in the energy expressions. The Hamiltonian can be expressed as

$$H = T_2 - T_0 + V\,. \tag{2.29}$$

where the general expression for T is

$$T = T_2 + T_1 + T_0\,. \tag{2.30}$$

In the above equation, T_2, T_1, and T_0 are functions respectively quadratic in, linear in and independent of the generalized velocities $\dot{q}_i$.

There are no nonconservative external forces in the present system. The attitude motion is under consideration assuming a Keplerian orbit which implies absence of environmental disturbances. If the energy expressions corresponding to the attitude motion, $T_{att} = T - T_{orb}$ and $V_{att} = V - V_{orb}$ do not involve time explicitly, then the corresponding Hamiltonian for the attitude motion is a constant of motion.

T_{att} and V_{att} can be expressed with true anomaly as the independent time variable using the Keplerian relations Eqs.(2.24) -(2.25) as:

$$\begin{aligned} T_{att} &= E^2\left\{\frac{1}{2}m_e\ell^2\left[(1+\alpha')^2\cos^2\gamma+\gamma'^2\right]\right. \\ &\qquad \left.+\frac{1}{2}(m_1(m_2-m_t)/m)\ell'^2\right\} . \end{aligned} \tag{2.31}$$

$$V_{att} = \mu D^{-3}(\frac{1}{2}m_e\ell^2)\left[1-3\cos^2\alpha\,\cos^2\gamma\right] . \tag{2.32}$$

where D and E are both functions of θ, given by the right hand sides of Eqs.(2.24) and (2.25), respectively.

As seen, for an eccentric orbit, θ appears explicitly in the energy expressions and the Hamiltonian is not conserved.

For a circular orbit, the expressions reduce to

$$\begin{aligned} T_{att} &= n^2\left\{\frac{1}{2}m_e\ell^2\left[(1+\alpha')^2\cos^2\gamma+\gamma'^2\right]\right. \\ &\qquad \left.+\frac{1}{2}(m_1(m_2-m_t)/m)\ell'^2\right\} . \end{aligned} \tag{2.33}$$

$$V_{att} = n^2(\frac{1}{2}m_e\ell^2)\left[1-3\cos^2\alpha\,\cos^2\gamma\right] . \tag{2.34}$$

The equation specifying the variation of length when $\ell' \neq 0$ (for deployment/retrieval case) introduces θ explicitly into the above energy expressions. However, during stationkeeping, ℓ is constant and for a circular orbit the energy expressions are clearly autonomous. Thus the corresponding Hamiltonian is a constant of motion. It is found to be

$$H = n^2(\frac{1}{2}m_e\ell^2)\left\{\gamma'^2+\cos^2\gamma(\alpha'^2-1-3\cos^2\alpha)-1\right\} . \tag{2.35}$$

or in a dimensionless form

$$2H/n^2m_e\ell^2+1 = \gamma'^2+\cos^2\gamma(\alpha'^2-1-3\cos^2\alpha) = C_H . \tag{2.36}$$

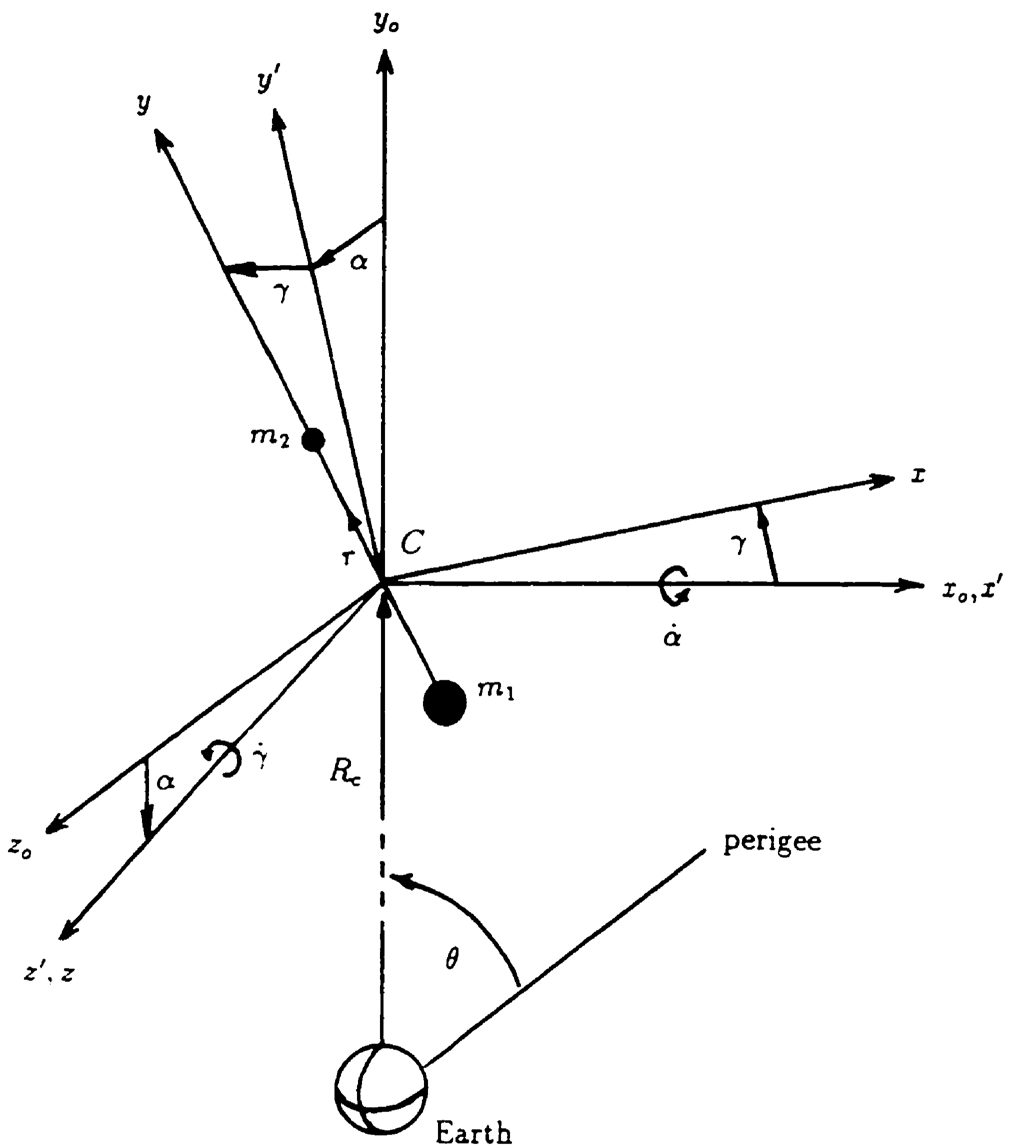

Figure 2.1: Geometry of the System

Chapter 3

Stationkeeping Phase

3.1 Introduction

For the stationkeeping case, the tether length is constant, i.e., $\ell' = 0$. Hence the governing equations of motion given by Eqs. (2.26) and (2.27) reduce to

$$\cos^2\gamma\,\{\alpha'' - [2\gamma'\tan\gamma - F](\alpha' - 1) - 3G\sin\alpha\cos\alpha\} = 0\,, \tag{3.1}$$

$$\gamma'' - F\gamma' - [(\alpha' - 1)^2 - 3G\cos^2\alpha]\sin\gamma\cos\gamma = 0 \tag{3.2}$$

with expressions (2.28)

$$F = 2\epsilon\sin\theta/(1 - \epsilon\cos\theta), \quad G = 1/(1 - \epsilon\cos\theta)\,.$$

These are the equations of motion of a gravity gradient pendulum. The gravity gradient pendulum is a special case (inertia ratio=1, a dumb-bell satellite) of the general gravity gradient stabilized satellite. As described in Chapter 1, the planar motion of a gravity gradient pendulum has been well-studied by both classical and modern nonlinear dynamic analysis techniques, but in the case of the three-dimensional coupled motion, only a more classical analysis has been made.

This Chapter examines both planar and coupled motion for the circular and elliptical orbits using the methods of modern nonlinear dynamics. The numerical techniques are used mainly but the analytical method of Melnikov has also been applied. to identify regular or chaotic motions. The equations of motion are integrated numerically to produce Poincaré sections. PSD's and Lyapunov exponents (computational tests which decide the nature of motion) as well as the phase plane plots and time histories. Details and some discussion on the numerical integration of the equations and construction of the power spectra. Poincaré sections and Lyapunov exponents are given at the end of the Chapter in Section 3.4.

Some general remarks regarding the dynamics of the tethered system during the stationkeeping phase are made here.

One notes that the equations of motion for the stationkeeping case are independent of the tether length. The gravity gradient restoring force which acts when the system is displaced from the local vertical grows with the tether length in the same manner as the moment of inertia. so the libration frequencies about the local vertical of the gravity gradient pendulum are independent of the tether length.

During stationkeeping. there are no dissipative forces: such a system is called a Hamiltonian system. As discussed in Section 2.7. the Hamiltonian of the system is conserved only for the stationkeeping phase in a circular orbit. in which case there are no dissipative forces and the energy expressions are autonomous: it is then given in dimensionless form by Eq. (2.36). repeated here for convenience:

$$\tilde{H} = H/n^2 m_e \ell^2 = \frac{1}{2}\left\{\gamma'^2 - \cos^2\gamma\,(\alpha'^2 - 1 - 3\cos^2\alpha) - 1\right\} . \tag{3.3}$$

When the eccentricity is non-zero. the time variable θ appears explicitly in the equations of motion as well as in the energy expressions. Hence the equations of motion are autonomous for a circular orbit. but non-autonomous for an elliptic orbit.

3.2 Planar Motion

From the equations of motion, one can notice that if roll motion is initially unexcited, the motion remains confined to the orbital plane. Then Eq. (3.1) reduces to

$$\alpha'' - F(\alpha' + 1) + 3G \sin\alpha \cos\alpha = 0 . \tag{3.4}$$

Equation (3.4) is the equation of motion of a planar gravity gradient pendulum. The circular orbit case is examined first, followed by the elliptic orbit case.

3.2.1 Circular Orbit

The nonlinear dynamics is analyzed starting from the simplest case, which is the case of a constant length tethered system in a circular orbit.

For zero eccentricity, Eq. (3.4) becomes

$$\alpha'' + 3 \sin\alpha \cos\alpha = 0 , \tag{3.5}$$

a nonlinear but autonomous equation of one degree of freedom. The phase space has two dimensions, α and α'. It was shown in Section 2.6 that the energy expressions are autonomous and since there are no dissipative forces acting in the stationkeeping phase, the Hamiltonian is a constant of motion. The system is integrable, and Eq. (3.5) has an analytical closed-form solution in terms of Jacobi elliptic functions. The dynamical behaviour is well understood, as reviewed by Hughes (1986) and others discussed in Section 1.2.

Equation (3.5) is similar to that of a simple pendulum and its motion differs only in the position of its equilibria. A simple pendulum has its centres at $\alpha = \pm 2n\pi$ and saddle points at $\alpha = \pm(2n + 1)\pi$, $n = 0, 1, 2..$; the gravity gradient pendulum has centres at $\alpha = \pm n\pi$ (the local vertical) and saddlepoints at $\alpha = \pm(2n+1)\pi/2$ (the local horizontal), $n = 0, 1, 2..$.

The phase plane trajectories, shown in Figure 3.1, are found analytically simply from the first integral of Eq. (3.5),

$$\alpha'^2 - 3\cos^2\alpha = E\,, \tag{3.6}$$

where E is twice the dimensionless Hamiltonian $\hat{H}$ of the system. $E \geq -3$ as is clear from Eq. (3.6). The separatrices ($E = 0$) separate the periodic (trajectories are closed) libration ($E < 0$) and the tumbling ($E > 0$) motions. The initial conditions determine E; the amplitude of the libration solutions α_{max} is a function of E, $\cos\alpha_{max} = \sqrt{-\frac{E}{3}}$, $E < 0$ for libration.

Figure 3.2 gives the PSD's constructed from numerical solutions with two sets of initial conditions, both in the libration range: $\alpha = 10°$, $\alpha' = 0$, and $\alpha = 80°$, $\alpha' = 0$.

The frequencies shown are nondimensionalized with respect to the orbital frequency, i.e. the number of oscillations per orbit.

The first PSD shows the peak at approximately the frequency of the linearized equation, $\sqrt{3}$, but also a small contribution from the third harmonic, which distorts the periodic motion from harmonic motion. The second shows the effects of larger amplitude motion, i.e., decreased effective stiffness and a lower fundamental frequency, and the appearance of odd harmonics up to the eleventh.

The dependency of the frequency of the periodic librations on amplitude is characteristic of nonlinear systems. The tumbling motion contains a periodic part whose frequency also depends on E. The solution at a given E has contribution from harmonics of the fundamental frequency at that E. The fundamental frequency at a specific E can be determined expressly in terms of E, involving the complete elliptic integral of the first kind. Conversely, the E required to produce a solution with a specific frequency is also obtainable. For instance, the frequency of libration coincides with the orbital frequency if the system has $E = -0.224$, an E produced by initial conditions $\alpha(0) = 74.2°, \alpha'(0) = 0$ or $\alpha(0) = 0, \alpha'(0) = 1.67$ for example; similarly the frequency of the periodic part of tumbling motion coincides with the orbital frequency if the system has $E = 0.195$, an E produced by initial conditions $\alpha(0) = 0, \alpha'(0) = 1.79$ for example.

The separatrix trajectory represents the system aperiodically and asymptotically approaching the horizontal. The frequency of the periodic component of the motion and its harmonics all tend to zero in the neighbourhood of the separatrix.

Note that if a driving frequency were applied, resonance could occur wherever harmonics or subharmonics of this frequency occur on the system frequency vs. E spectrum. In the neighbourhood of the separatrix there would always be an infinite number of resonances regardless of the forcing frequency. (This is well illustrated by Reichl (1992), Lin and Reichl (1985) for the forced pendulum system.) Nonlinear resonances are the root of chaos in nondissipative systems. In the elliptic orbit case, considered next, the system is a driven oscillator problem.

3.2.2 Eccentric Orbit

Let us now return to the motion in eccentric orbits, that is the motion governed by Eq. (3.4).

As discussed in Section 1.2, this equation has been studied by several authors as a special case (inertia ratio of unity) of the *planar* gravity gradient satellite. In particular, Karasopoulos and Richardson (1992, 1993) and Tong and Rimrott (1991a) applied modern nonlinear analysis techniques to this case.

This is a nonlinear forced one-degree of freedom system, with parametric coefficients; the equation is non–autonomous; its phase space is spanned by the three dimensions α, α' and θ.

Pitch oscillations are forced in an eccentric orbit by the nonuniform rotational rate of the local vertical (position vector). This is seen clearly from the rotational acceleration appearing in the equation of motion with time as the independent variable, i.e., Eq. (2.21) with $Q_\alpha = 0, \dot{\ell} = 0, \gamma = \gamma' = 0$,

$$\ddot{\alpha} + (3\,\mu/R_c^3)\,\sin\alpha\,\cos\alpha = -\ddot{\theta}. \qquad (3.7)$$

Returning to the equation under consideration, Eq. (3.4), one notes that there are no equilibrium points, as when the time derivatives (θ acts as the time variable) are put to zero, a constant solution for α does not exist. (Note that F and G depend on θ.)

While the stationkeeping system is Hamiltonian, the Hamiltonian is not conserved in the eccentric orbit case, as the energy expressions contain θ explicitly (Section 2.7).

This Hamiltonian system is near–integrable, as shown for small ϵ by Tong and Rimrott (1991a) using Melnikov's Method. Melnikov's Method, described in more detail and applied in the following Section, examines the behaviour of trajectories in the neighbourhood of the separatrix in terms of a small parameter which perturbs the system from an integrable one (in the present case, $\epsilon = 0$). In a conservative (Hamiltonian) system, Melnikov's Method determines whether the system is integrable or near-integrable, for small values of the perturbation parameter. Integrable systems will exhibit only regular motion. Near-integrable systems are characterized by the simultaneous presence of regular and chaotic trajectories.

Chaotic motion refers to that motion in deterministic (no random inputs or parameters) systems whose time history has a sensitive dependence on initial conditions. When initial conditions lie in a chaotic region, a small difference in the initial conditions results in an exponential divergence of the corresponding trajectories, such that the motion is unpredictable. Moon (1992) is a very readable introduction to chaotic motion in engineering systems; chaotic motion in Hamiltonian (conservative) systems in particular is treated thoroughly by Lichtenberg and Lieberman (1992) and is also well discussed by Reichl (1992) and Percival (1987).

In a conservative system each set of initial conditions leads to a unique trajectory which (apart from being stationary) may be periodic, quasi-periodic or chaotic.

The regular trajectories (periodic or quasi-periodic) of libration of the present system may be viewed as lying on a torus with the motion occurring around the minor axis at the pitch frequency and the major axis at the forcing orbital frequency. When the frequencies making up the oscillation solution have an irrational ratio, the solution is quasi periodic. When the ratio is rational the solution is a resonance, and is periodic.

The motion may be studied by taking a Poincaré section which lies in a two-dimensional space, via sampling the states at the forcing frequency. Then periodic motion is shown as a discrete set of points and quasi-periodic motion as a closed orbit. Chaotic motion, in this conservative system, appears in the Poincaré section as a cloud of disorganized points. The phase space of a nonlinear system must have at least three dimensions for chaotic motion to be possible.

Numerical solutions from different initial conditions of Eq. (3.4) were used to construct Poincaré maps, sampled at period 2π, α plotted mod 2π. No chaotic region was found for zero eccentricity as expected. However, when the eccentricity was increased, chaotic regions separating orderly librational and tumbling solutions appeared (Figure 3.3 for $e = 0.003$ and 0.1). This region, represented by finely scattered points in Figure 3.3, grows with an increase in eccentricity. This chaotic region appears to grow from the separatrices of the circular orbit phase plane. The librational solutions shown are quasi-periodic (closed orbits). Note that for larger initial conditions the orbits break-up: the tori break up as the chaotic region is approached in the phase space. Tong and Rimrott (1991a) and Karasopoulos and Richardson (1992) have presented more detailed Poincaré maps for planar motion of a general gravity gradient satellite including resonant solutions. Tong and Rimrott (1991a) observe that a state of global chaos, where most of the phase space is covered by chaotic trajectories, occurs at about eccentricity $e = 0.3$.

Figure 3.4 is a PSD taken from a solution with the smaller set of initial conditions used in the PSD's of the previous section, but with eccentric orbit, $\epsilon = 0.1$; this set of initial conditions lies in the regular region of the corresponding Poincaré map. The PSD now shows the forcing frequency of unity (i.e. the orbital frequency) in addition to the pitch frequency; this is because for small motions and eccentricity Eq.(3.4) can be approximated as

$$\alpha'' + 3\alpha \sim 2\epsilon \sin\theta + \mathcal{O}(\epsilon^2) \ . \tag{3.8}$$

The other peaks are combination tones of these two frequencies as shown. As the motion is made up of pitch and true anomaly frequencies which are incommensurate, the motion is quasi-periodic.

The occurrence and growth of the chaotic region is explained briefly here. When a near-integrable system is perturbed from an integrable one by a parameter, in this case ϵ, chaos will always occur in the separatrix region due to the infinite number of resonance zones that accumulate there. The separatrix trajectory is no longer smooth and develops a complex behaviour which the Melnikov Method examines. The chaotic region is initially confined to the separatrix region by the regular quasi-periodic closed curves, known in the conservative chaos literature as KAM (Kolmogorov, Arnold, Moser) curves, which separate resonance zones throughout the phase space. As the perturbation strength increases, the higher order resonances successively destroy the KAM curves (resonance overlap), and the chaotic region grows (Lichtenberg and Lieberman, 1992).

3.3 Coupled Motion in Stationkeeping Phase

Considering now both pitch and roll degrees of freedom, the motion in the stationkeeping phase is governed by Eqs. (3.1)-(3.3). The circular orbit case is studied first. A study of the elliptic orbit case follows.

3.3.1 Circular Orbit

In the case of a circular orbit, $F = 0$ and $G = 1$; thus Eqs. (3.1) and (3.2) reduce to

$$\cos^2\gamma \; \{\alpha'' + (-2\gamma' \tan\gamma)(\alpha' + 1) + 3 \sin\alpha \cos\alpha\} = 0 . \tag{3.9}$$

$$\gamma'' + \left[(1 + \alpha')^2 + 3 \cos^2\alpha\right] \sin\gamma \cos\gamma = 0 . \tag{3.10}$$

The system described by these equations is a gravity gradient pendulum with motion in three dimensions, in a circular orbit. As discussed in Section 1.2, these equations have been studied by several authors as a case (inertia ratio of unity) of the gravity gradient satellite in a circular orbit using classical approaches; however it has not been studied in the modern sense of regular or chaotic motion.

This system of equations is autonomous and involves nonlinear coupling between the two degrees of freedom. The phase space has the four dimensions α, α', γ, and γ'.

The equilibrium points are $(\alpha_e, \gamma_e) = (\pm n\pi, \pm n\pi), (\pm(2n+1)\pi/2, \pm n\pi), (constant, \pm(2n+1)\pi/2)$, $n = 0, 1, 2...$ i.e., the local vertical, the local horizontal in the orbital plane, and the orbit normal. A linear analysis around these fixed points shows that only the first one is stable.

As shown in Section 2.7, the Hamiltonian for this system is conserved: Eq. (2.36) is repeated here for convenience:

$$2H/n^2 m_e \ell^2 - 1 = \gamma'^2 + \cos^2\gamma(\alpha'^2 - 1 - 3\cos^2\alpha) = C_H \ .$$

Any one of the four dimensions can be eliminated for a given C_H, allowing a three dimensional state space representation of the motion. Setting $\gamma' = 0$ in Eq. (2.36) for a given C_H gives a motion envelope in α, α', γ space surrounding the region of possible motion. Setting $\alpha' = \gamma' = 0$ in Eq. (2.36), (just the cross section of the motion envelope at $\alpha' = 0$), defines the zero velocity curves in α - γ space which bound regions of possible motion, such that (Modi and Brereton(1968), Modi and Shrivastava (1971a)): for $C_H < -4$ no motion is possible; for $-4 \leq C_H \leq -1$ motion is bounded; for $-1 < C_H \leq 0$ motion is bounded in γ only; and for $0 < C_H$ unbounded motion (tumbling) is possible in both α and γ.

In the following two sections the nature of the motion governed by Eqs. (3.9) - (3.10) is studied through numerical techniques. The equations are integrated numerically to produce time histories, phase plane plots, Poincaré Sections, PSD's and Lyapunov exponents (numerical details are given in Section 3.4). In Section 3.3.1.3 the approximate analytical method of Melnikov is applied to an idealized version of the system.

3.3.1.1 Series of Poincaré Sections for Increasing Values of Hamiltonian Constant C_H (Several Initial Conditions at a Given C_H)

First, a series of Poincaré sections for increasing C_H are presented (Figures 3.5 (a)-(d)).

A discussion of the generation of a Poincaré section of a two degree of freedom autonomous Hamiltonian system is discussed by Henon and Heiles (1964), and Lichtenberg and Lieberman (1992). Trajectories of the system lie in the three-dimensional surface C_H =constant in the four dimensional phase space, its bounds being the bounds of motion at that C_H. In the system under consideration here, a Poincaré section of a trajectory can be taken by sampling α and α' when $\gamma = 0$ and $\gamma' > 0$. The Poincaré section lies in three dimensions (α, α', γ'), and the $\alpha - \alpha'$ plot is its two–dimensional projection. The motion of the system can be viewed thus in a two–dimensional Poincaré plot made up of trajectories from different initial conditions for a given C_H, lying within the bounds of possible motion at that C_H. The boundary of the region of possible motion for a given C_H in this two dimensional plot is determined from Eq. (2.36), setting $\gamma' = 0$ as well as $\gamma = 0$ (the cross section at $\gamma = 0$ of the aforementioned motion envelope $\gamma' = 0$ in α, α', γ space).

In this Poincaré section, a periodic solution or resonance, where the ratio between pitch and roll frequency is rational will appear as a discrete set of points: n points indicates some integer number of pitch oscillations in n roll oscillations. A resonant quasiperiodic solution, where the ratio is irrational, appears as a set of closed curves or islands, each island surrounding a periodic point. A periodic (or resonant quasiperiodic) trajectory successively visits each periodic point (or resonant quasiperiodic closed curve). Nonresonant quasiperiodic orbits will trace out a curve covering all values of pitch; these are limited to tumbling solutions. A chaotic solution appears as a diffused set of points: it will fill the region of possible motion for a given C_H, where motion is not regular (neither periodic nor quasiperiodic).

Poincaré sections generated for a number of initial conditions at each C_H show the development of chaotic regions in the phase space in two degree of freedom, conservative Hamiltonian systems which are near-integrable. In such a system, separatrices surround the resonances: the regions near these separatrices are always chaotic, as is observable when shown on a large enough scale. The growth of the chaotic region occurs via the mechanism of resonance overlap as the system Hamiltonian is increased. An excellent detailed discussion of chaotic motion in such systems is found in Lichtenberg and Lieberman (1992).

Figures 3.5 (a)-(d) present Poincaré sections for C_H =-1.5, -1.25, -1 and -0.5, respectively: each is made up of several trajectories of varying initial conditions. Each trajectory was computed to a minimum of 500 orbits. The boundary of the region of possible motion in each plot is shown as well: the growth of this region with increasing C_H and the possibility of tumbling in pitch for $C_H > -1$ is illustrated.

For low C_H, $C_H = -1.5$ of Figure 3.5 (a), the Poincaré section of five trajectories from varying initial conditions were taken. Three resonant quasiperiodic solutions i.e., three sets of closed curves, are shown: those associated with the resonances of some number of pitch oscillations for one, five and three roll oscillations. The periodic points were not isolated in this work, but Modi and Shrivastava (1972) isolated these solutions and from time histories identified them as P_{21}, P_{45}, and P_{23}, respectively, where P_{mn} signifies m pitch oscillations in n roll oscillations. In addition the separatrix associated with the P_{45} resonance is shown: also, the separatrix associated with a P_{m4} solution is shown, where m has not been identified. These separatrices are actually very thin chaotic layers: on a large enough scale they are shown to consist of a scatter of points. At this C_H the motion is mainly regular.

For a larger C_H, $C_H = -1.25$ of Figure 3.5 (b), the Poincaré section of four trajectories were taken. A chaotic region is observed and was created by a single chaotic trajectory. It fills the region of possible motion where motion is not regular. The regular region associated with the P_{m4} resonance discussed earlier has disappeared; those associated with the P_{21}, P_{45}, and P_{23} resonances remain.

For $C_H = -1$ of Figure 3.5 (c), the Poincaré section of four trajectories are shown. The chaotic region has grown such that only the regular regions associated with the P_{21} and P_{23} resonances remain. One may also observe the reduction in the proportion of the region of the possible motion taken up by the regular region associated with the fundamental P_{21} resonance (as outlined by the chaotic region). This figure includes two quasiperiodic trajectories associated with the P_{21} resonance.

Trajectories from three initial conditions generated the Poincaré section of Figure 3.5 (d) for $C_H = -0.5$. Solutions which tumbled in α were plotted for mod 2π. The chaotic region appears to have grown such that the regular region associated with the P_{21} resonance is the only regular region associated with libration remaining. Also the chaotic region is unbounded in terms of tumbling. Note that a regular region of nonresonant quasiperiodic tumbling has appeared for positive pitch rate.

In summary, for a given C_H, the type of motion depends on the initial conditions. As C_H was increased, the region of possible motion possessed: (i) mainly regular libration; (ii) regular and chaotic libration, with the chaotic region taking a larger and larger proportion of the region of possible motion; (iii) regular libration, regular and chaotic tumbling.

The present work has presented a series of Poincaré plots, over a range of C_H documenting the change in behaviour, as interpreted by Hamiltonian chaotic dynamics.

This was not done in earlier work on stability and periodic solutions of this system by Modi and Shrivastava (1972, 1971a). Modi and Brereton (1968) who did include some Poincaré plots and noted 'ergodic' solutions. It is instructive, however, to make comparisons with the results they present.

They presented Poincaré plots for $C_H = -1.25$ and $C_H = -1$ similar to those presented here except that, other than having isolated the periodic solutions for $C_H = -1.25$ and the limiting (largest) orbits of the resonant quasiperiodic regions at least for $C_H = -1.25$, each trajectory was only integrated for 40-50 orbits (the computers in the late sixties were slow). In each case, the chaotic region was not entirely filled out, as was done here using a single chaotic trajectory. They called the trajectories appearing as scattered points, now known as chaotic, as 'ergodic'; they speculated that they 'may involve periodicity over a large number of orbits' which they do not. The significance of the closed curves as quasiperiodic motion was not emphasized.

These are the only $(\alpha - \alpha')$ Poincaré plots actually presented, but they make observations about the change in behaviour for increasing C_H. They state that 'ergodic' trajectories appear for C_H greater than a critical value, -2.56. This was not verified in the present work. However, it is expected that at a large enough scale, chaos can be observed for all C_H. From theory and other numerical work in Hamiltonian dynamics, chaos is always present near the separatices associated with resonances in near-integrable two degrees of freedom systems; there should be no sudden transition to chaos at some critical C_H.

They observed an increasing tendency for motion other than of the P_{21} regular region as C_H approaches -1, with which the results here agreed. The results here also agreed with their observation that for greater C_H the only stable solutions are those associated with the P_{21} regular region.

Finally at $C_H = 0.827$, they observed that the P_{21} regular region reduces to just the periodic solution, so that beyond this value gravity-gradient stabilization is not possible. That this occurs at that value of C_H was not verified in this work.

3.3.1.2 Series of Poincaré Sections, Phase Plane Plots, Time Histories, PSD's and Lyapunov Exponents, for Increasing Initial Conditions $\alpha(0) = \gamma(0) = k$, $\alpha'(0) = \gamma'(0) = 0$

The nature of motion in this system is now documented numerically further, through several numerical tools of nonlinear dynamics and chaos. The analysis covers the change from regular to chaotic motion for the initial conditions of initial angles $\alpha(0) = \gamma(0) = k$, where k is a given angle, and zero initial velocities, as k is increased. Power spectra and Lyapunov exponents as well as Poincaré sections are computational tests which identify regular or chaotic motion: all three of these tests, as well as phase plane plots and time histories, were taken for the individual trajectories (comments on numerical analysis issues can be found in the last section of the chapter). As discussed below, the Poincaré sections, power spectra and Lyapunov exponents show excellent agreement in identifying a change from regular to chaotic motion, as k is increased, at $k = 13°$, and an increase in the degree of the chaotic motion as k is increased further.

Poincaré sections were taken of individual trajectories as done earlier, i.e., recording α and α' when $\gamma = 0$ and $\gamma' > 0$, and are shown in Figure 3.6(a)-(d). They are all taken over 500 orbits. Note that C_H increases with k for $0 < k \leq 90°$. Thus, each trajectory moves on a different surface C_H =constant with respective bounds (discussed earlier).

Figure 3.6(a) shows the Poincaré sections of trajectories with $k = 10°, 20°, 30°$.

and 40° plotted on one graph for convenience: as C_H is not constant for the trajectories shown in this figure the trajectories cross. Figure 3.6(b) is the section for the trajectory with $k = 42°$. These figures show the closed curves characteristic of quasi-periodic oscillation, although they appear to deform and begin to break up as the initial angles are increased. At $k = 43°$ however the motion is chaotic as shown by the scatter of points in the section of the trajectory of Figure 3.6(c). The section of the chaotic trajectory at $k = 49°$ of Figure 3.6(d) covers a much larger region and shows tumbling occurs in pitch (the trajectory was plotted for mod 2π in α).

From the previous discussion of the series of Poincaré sections for constant C_H (Figure 3.5) one recognizes the quasiperiodic trajectories shown here as belonging to the quasiperiodic region associated with the P_{21} resonance. Also, one recognizes the chaotic trajectory of Figure 3.6 (c) for $k = 43°$ as the separatrix trajectory of the P_{45} resonance, shown in Figure 3.5, the Poincaré section for $C_H = -1.5$; the trajectory for $k = 43°$ has $C_H = -1.39$. The chaotic trajectory of Figure 3.6 (d), $k = 49°$ fills the chaotic region for the respective C_H, $C_H = -0.99$. Just inside the limit for tumbling in pitch ($C_H > -1$) tumbling has occurred: the chaotic trajectory is otherwise identical to that of Figure 3.5 (c) for $C_H = -1$, with the regular regions associated with the P_{21} and P_{23} resonances outlined (compare also with Figure 3.5 (d) for $C_H = -0.5$).

The motion $k = 43°$ exhibits limited chaos which is characterized by chaotic phase space orbits remaining close to some regular motion orbit. For larger k, $k = 49°$ the motion has developed large-scale chaos where chaotic orbits traverse a broad region of phase space.

Figure 3.7 gives the phase planes and time histories, to 80 orbits, of the trajectories with $k = 40°, 42°, 43°$ and $49°$ respectively. The change from regular to chaotic motion cannot be discriminated conclusively from phase planes and time histories, and thus computational tests such as Poincaré sections, PSD's and Lyapunov exponents are used. A subtle difference in their appearance could be noted when carefully comparing the quasiperiodic and chaotic vibrations, namely the wandering in the phase plane and aperiodicity of the time histories for the chaotic trajectories were somewhat greater. Many of the chaotic trajectories also showed, more obviously, an interesting exchange of energy between the two degrees of freedom in the time histories. These differences are seen in this figure, comparing the quasiperiodic ($k = 40°, 42°$) and chaotic ($k = 43°, 49°$) oscillations. The exchange of energy between the two degrees of freedom appears to begin towards the end of the time history of the $k = 43°$ case, and is quite striking in the $k = 49°$ case. Note that this figure shows that the $k = 49°$ trajectory, which was shown to tumble in the Poincaré section taken over 500 orbits, does not tumble to at least 80 orbits (recall this case is just inside the $C_H > -1$ tumbling limit).

The following PSD's were taken from trajectory solutions, under 80 orbits.

Figure 3.8 (a)-(b) shows the pitch and roll PSD's for small initial conditions, $\alpha(0) = \gamma(0) = k = 10°$, $\alpha'(0) = \gamma'(0) = 0$ and for comparison, $\alpha(0) = 0$, $\gamma(0) = 10°$, $\alpha'(0) = \gamma'(0) = 0$. The frequency spectrum is composed of combination tones of the two natural frequencies of the linearized system, $\sqrt{3}$ and 2. Their being incommensurate results in quasi-periodic motion. Pitch motion α has a forcing frequency of twice the fundamental roll frequency as seen from the equations approximated for small motions:

$$\alpha'' + 3\alpha \sim 2\gamma'\gamma + \mathcal{O}(\epsilon^3) \sim \sin(4\theta). \tag{3.11}$$

This can be verified in the PSD's. The contribution of this forcing frequency is smaller than the natural α frequency, as it is of second order. Its relative contribution is larger for the case (a) where α was initially undisturbed compared to the case (b) where both angles were initially present.

Figure 3.8 (b) along with Figures 3.9 (a)-(d) make up a series of pitch and roll PSD's for trajectories with increasing initial angles k, $k = 10°$ and $k = 40°, 42°, 43°$ and $49°$, respectively. As the initial angles are increased, the PSD's have more frequency components, and contain distinct and identifiable combination tones up to $k = 42°$. For larger k the spectrum broadens, as characteristic of chaotic vibration. This indicates the change from quasi-periodic to chaotic motion. The PSD's of the motion for $k = 43°$ exhibit the characteristic of limited or, equivalently, narrow-band chaos, which is narrow or limited broadening of certain frequency spikes. For $k = 49°$, the PSD's of motion have developed the characteristic of large-scale or, equivalently, broad-band chaos, that is a broad range of frequencies.

Finally, the largest Lyapunov exponents of the trajectories were calculated. Chaotic motion is characterized by great sensitivity of the motion to small changes in initial conditions. Closely neighbouring orbits which are chaotic, diverge exponentially locally (only locally since the phase space may be bounded). The Lyapunov exponents of a given trajectory characterize the mean rate of exponential separation of trajectories surrounding it. An n dimensional system has n Lyapunov exponents, but the first or largest Lyapunov exponent λ, associated with the direction of most rapid growth, dominates the dynamics over time. It can be obtained from Moon (1992):

$$\lambda = \lim_{N \to \infty} \frac{1}{t_N - t_0} \sum_{k=1}^{N} \log_2 \frac{d(t_k)}{d_0(t_{k-1})} \tag{3.12}$$

One considers a reference trajectory; d_0 is a measure of the initial distance in the phase space between this trajectory and a nearby trajectory, d is the distance at a small but later time. One measures d/d_0, then considers a new nearby trajectory and defines a new d_0. Since the exponential divergence of chaotic orbits is only local, the growth must be averaged at many points along the trajectory in this way. It approaches a constant value for large N. Details of the calculation of λ using Eq. (3.12), including the determination of the length ratio d/d_0 in Eq. (3.12), is given in Section 3.4.

Thus the first Lyapunov exponent is a quantitative test for chaos: a chaotic trajectory has $\lambda > 0$, and a regular trajectory has $\lambda = 0$ (for a Hamiltonian system). It also is a measure of the degree of chaotic behaviour of a trajectory: the greater its value, the more chaotic the trajectory.

Figure 3.10 plots the first Lyapunov exponents for trajectories with $k = 10°$, $40°$, $42°$, $43°$, $45°$ and $49°$, over 200 orbits. For $k = 10°$, $40°$, $42°$, λ appears to tend to zero, with the $40°$ and $42°$ curves indistinguishable from each other. However for $k = 43°$, the exponent tends to a positive value, about 0.05. This value increases as k is increased to $k = 45°$ and $49°$ (λ is equal to about 0.1 and 0.16, respectively). The calculated Lyapunov exponent is by definition more accurate the longer the time over which it is averaged. The first Lyapunov exponent was calculated over 1000 orbits for trajectories with $k = 10°$, $40°$,$42°$ and $49°$ and are plotted again as a function of orbits in Figure 3.11. In this figure the tendency to zero for large time of the $k = 10°$,$40°$,$42°$ cases is clear. The exponent for the $k = 49°$ case shows only a slight variation from 200 to 1000 orbits (its value is 0.15 at 1000 orbits): one expects that the $k = 43°$, $45°$ would also show little variation, and that the values of the three cases indicated in Figure 3.10 up to 200 orbits are accurate at least relative to each other. Thus these figures show that the first Lyapunov exponent (in the limit for large time) has zero value for $k = 10°$, $40°$, $42°$ and positive value that increases with k for $k = 43°$,$45°$ and $49°$. Thus regular motion is indicated for $k = 10°$, $40°$, $42°$; a mean rate of exponential divergence of trajectories that increases with k, that is chaotic motion of increasing degree with k, is indicated for $k = 43°$,$45°$ and $49°$.

The Poincaré sections, PSD's and first Lyapunov exponents presented show excellent agreement in identifying a change from regular to chaotic motion, as k is increased, at $k = 43°$, and an increase in the degree of chaotic motion as k is increased further.

Previous work of relevance to this system, other than by Modi and Shrivastava (1971a, 1972) and Modi and Brereton (1968), is that of Melvin (1988a, b). The results here confirm, by modern nonlinear dynamics numerical analysis techniques, the existence of some chaotic solutions suggested by Melvin for the gravity gradient pendulum. His work included the numerical integration of the equations of motion of this system, but not the modern techniques. He plotted the two degrees of freedom of solutions as well as zero velocity curves on a unit sphere. For certain conditions he observed libration solutions characterized by the filling of a large portion of the zero velocity surface, and interpreted them as chaotic. Based on the present work, this appears a valid interpretation, as the zero velocity surface in $\alpha - \gamma$ space is just a cross section of the motion envelope $\gamma' = 0$ in α, α', γ space, like the boundary of possible motion in the $\alpha - \alpha'$ Poincaré plots presented: most (but not all) chaotic libration solutions, unlike regular libration solutions, filled large portions of the regions of possible motion in the Poincaré plots. Also, his results and the results here agree, where comparisons were made, as discussed below. The computational tests of modern nonlinear dynamics, which decide the nature of a solution (Poincaré sections, PSD's, Lyapunov exponents) were applied in the present work, but not in Melvin's work.

Specifically, Melvin (1988b) observes a chaotic libration region for motions from rest with small initial roll angle and large initial pitch angle. In Melvin (1988a) on the other hand solutions were taken with initial conditions on various zero velocity curves, that is *from rest* for various values of the Hamiltonian constant. In terms of C_H used here, Melvin found solutions with $C_H > -1$ quickly tumbled and did not examine their behaviour. For $C_H = -1$ he found chaotic solutions for $\alpha(0) > 47.5°$. He also found chaotic solutions for C_H slightly less than -1. Comparisons are made now with the results of the latter paper and the results of the present work.

The results in the paper by Melvin (1988a) allow easy comparison with the results obtained here, for the initial conditions $\alpha(0) = \gamma(0) = k, k, \alpha'(0) = \gamma'(0) = 0$ (i.e. also from rest), when respective C_H is calculated. The solutions taken with k such that $C_H > -1$ did quickly tumble, apart from the solution at $k = 49°$ where $C_H = -0.99$ and tumbling occurs after some time. With C_H so close to $C_H = -1$, the chaotic $k = 49°$ solution of this thesis can be compared with his result, and it is in agreement. Here chaotic solutions were observed to begin for $k \geq 43°$ or $C_H \geq -1.39$.

A careful comparison of the results of Melvin (1988a) and the Poincaré plots for given C_H presented here (Figures 3.5) can also be made. Libration solutions are seen for $C_H > -1$ in the plots: note that the plot is not limited to trajectories beginning from rest as are his results. The plot for $C_H = -1$ allows for his result, recognizing that an initial condition on the plot has $\gamma(0) = 0$ only and at rest corresponds to only $|\alpha(0)| = 90°$, where the boundary $\gamma' = 0$ and the $\alpha' = 0$ axis meet: the plot suggests that chaotic solutions exist for $|\alpha(0)| > 45°$ appoximately, when $\gamma(0) = 0, \alpha' = 0, \gamma' > 0$. That he found chaotic solutions for C_H slightly less than -1, is within the results of the plots here for $C_H < -1$, recalling that the chaotic region becomes appreciable as $C_H = -1$ is approached from smaller values.

Sections 3.3.1.1 and 3.3.1.2 have applied the numerical techniques of modern Hamiltonian nonlinear dynamics analysis to the coupled motion of a constant length tethered system, or equivalently, a gravity gradient pendulum. The present work has presented a detailed series of Poincaré plots. each made up of several trajectories for a given Hamiltonian constant. over a range of the constant. to document the change in behaviour as interpreted by modern nonlinear dynamics. i.e.. the regions of regular and chaotic motion. This was not done in the early work by Modi and Shrivastava (1972. 1971a) and Modi and Brereton (1968) who presented a few Poincaré plots in studies of stability and periodic solutions of the system. and observed 'ergodic' solutions. The present work has also presented a series of Poincaré sections. PSD's. and Lyapunov exponents. that is the computational tests which decide the nature of motion. as well as phase plane plots and time histories. to document the change from regular to chaotic motion for trajectories starting from rest with equivalent initial pitch and roll angles. as the angle is increased. Together with the Poincaré plots for constant C_H. these results confirm the existence of chaotic solutions in this system. suggested by Melvin (1988a. 1988b) who observed 'chaotic' libration solutions plotted in the pitch-roll zero velocity surface.

3.3.1.3 Melnikov's Method Applied to the Idealized System

The near integrability of the system and presence of chaotic motion is shown in Sections 3.3.1.1 and 3.3.1.2 by numerical means. As mentioned in Section 3.2. the analytical method of Melnikov could be used to determine whether a conservative system is integrable or near-integrable. where the system can be considered as a perturbation of an integrable system. This is done for an idealized version of the system as detailed presently.

Melnikov's Method is usually applied to planar (two dimensional) systems. Adaptation of the theory to higher dimensional systems is given briefly in Guckenheimer and Holmes (1983) and in detail in Wiggins (1988). and has been applied by Gray and Stabb (1993) to study the controlled pitch dynamics of a gravity gradient satellite. Application of Melnikov's Method to a two degree of freedom system assumes that the system can be considered as a perturbation of an integrable two degree of freedom system. Although it may be possible to apply the method to the full two degrees of freedom system considered here, in the following, assumptions are made which idealize the system such that the standard planar Melnikov theory can be used: the near-integrability of the idealized system will be shown.

The assumption made is that roll is small and is harmonic. Assuming first alone that roll is small such that $\gamma = \mathcal{O}(\sqrt{\epsilon})$, where ϵ is a small parameter, then, keeping to order ϵ, Eq. (3.10) becomes

$$\gamma'' + \left[(1 + \alpha')^2 + 3\cos^2\alpha\right]\gamma = 0\,. \tag{3.13}$$

One assumes now that the bracketed term is approximately a constant k^2 or that roll is harmonic; then with initial conditions $\gamma(0) = \gamma_0 = \sqrt{\epsilon}$, $\gamma'(0) = 0$, one has

$$\gamma = \sqrt{\epsilon}\cos k\theta. \tag{3.14}$$

With the roll described by Eq. (3.14), the pitch equation Eq. (3.9) becomes, to order ϵ

$$\alpha'' + \epsilon k \sin 2k\theta(\alpha' - 1) + 3\sin\alpha\,\cos\alpha = 0\,. \tag{3.15}$$

Assuming roll to be small and harmonic has reduced the system to a planar system with a time-periodic forcing perturbation. The unperturbed system $\epsilon = 0$, just the planar system described by Eq. (3.5), is integrable with a saddle point and separatrix orbit. The standard planar theory of Melnikov can now be applied.

A description of the planar theory of Melnikov can be found in Moon (1992), Reichl (1992), Lichtenberg and Lieberman (1992), and in more mathematical detail in Wiggins (1990.1988) and Guckenheimer and Holmes (1983). Suppose the system equations of motion can be written as

$$\dot{q} = \frac{\partial H}{\partial p} + \epsilon g_1 \tag{3.16}$$

$$\dot{p} = -\frac{\partial H}{\partial q} + \epsilon g_2 \tag{3.17}$$

where (q, p) are the generalized coordinate and momentum variables. $\bar{g} = \bar{g}(p, q, t) = (g_1, g_2)$ is periodic in time. ϵ is a small parameter and $H(q, p)$ is the Hamiltonian for the (undamped. unforced) integrable problem ($\epsilon = 0$). The Melnikov function is

$$M(\tau_0) = \int_{-\infty}^{+\infty} \bar{g}^* \cdot \overline{\nabla} H(q^*, p^*) d\tau \tag{3.18}$$

where $\bar{g}^* = \bar{g}(q^*, p^*, t + t_0)$; $q^*(t)$ and $p^*(t)$ are the solutions for the separatrix of the saddle point in the phase plane of the unperturbed problem. and t_0 is a measure of the distance along this separatrix. In the phase plane of an integrable system the stable and unstable manifolds of the saddle point join smoothly; however these manifolds separate and oscillate and may intersect transversely in the Poincaré section of the perturbed problem where integrability has been destroyed (Figure 3.12). Transverse intersection leads to chaotic motion near the separatrix. The Melnikov function is a measure of the separation between stable and unstable manifolds of the saddle point in the Poincaré section of the perturbed problem. If $M(\tau_0)$ has simple zeros they intersect. In a conservative system if the manifolds separate they will always have transverse intersection: Melnikov's Method can be used to demonstrate whether a conservative system is integrable or near-integrable. and whether chaotic motion will occur. In a dissipative system the manifolds separate and oscillate but need not cross. and Melnikov's Method yields at what parameter values the crossing. and thus chaos. occurs.

Returning to Eq. (3.15), one first rewrites it in the following form:

$$\alpha'' + (3/2)\ \sin 2\alpha = \epsilon[-k \sin 2k\theta(\alpha' + 1)]\,. \tag{3.19}$$

The left hand side can be written as that of the normalized pendulum equation by making the substitutions $\phi = 2\alpha$ and $\tau = \sqrt{3}\theta$, and then after some algebra,

$$\frac{d^2\phi}{d\tau^2} + \sin\phi = \epsilon[A \sin\omega\tau(\frac{d\phi}{d\tau} + a)]\,, \tag{3.20}$$

where $(\omega = 2/\sqrt{3})\,k$, $A = -(1/\sqrt{3})\,k$ and $a = 2/\sqrt{3}$.

In Eqs. (3.16)-(3.17) one has $t = \tau$, $q \equiv \phi$ and $p \equiv v = d\phi/d\tau$, $g_1 = 0$ and $g_2 = [A \sin\omega\tau(\frac{d\phi}{d\tau} - a)]$. The Hamiltonian for the unforced problem $(\epsilon = 0)$ is

$$H = (1/2)\ v^2 + (1 - \cos\phi)\,. \tag{3.21}$$

and

$$\frac{\partial H}{\partial\phi} = \sin\phi, \quad \frac{\partial H}{\partial v} = v\,. \tag{3.22}$$

Thus

$$\bar{g}\cdot\overline{\nabla}H = g_2 v. \tag{3.23}$$

On the unperturbed separatrix orbit from the saddle point ($\phi = \pi \pmod{2\pi}, v = 0$) $H = 2$. Considering just the positive branch of the unperturbed separatrix orbit the solution is found to be

$$\phi^* = 2\tan^{-1}(\sinh\tau)\,. \tag{3.24}$$

$$v^* = \frac{d\phi^*}{d\tau} = 2\,\text{sech}\,\tau\,. \tag{3.25}$$

The Melnikov function from Eq. (3.18) thus becomes

$$M(\tau_0) = 2A\left[2\int_{-\infty}^{+\infty} \sin\omega(\tau + \tau_0)\,\text{sech}^2\tau d\tau + a\int_{-\infty}^{+\infty} \sin\omega(\tau + \tau_0)\,\text{sech}\,\tau d\tau\right] \tag{3.26}$$

The integrals

$$\int_{-\infty}^{+\infty} \sin\omega(\tau)\,\text{sech}^2\tau d\tau = 0\,. \tag{3.27}$$

$$\int_{-\infty}^{+\infty} \sin\omega(\tau)\,\mathrm{sech}\,\tau d\tau = 0\,. \tag{3.28}$$

since the integrands are odd. The integrals

$$\int_{-\infty}^{+\infty} \cos\omega(\tau)\,\mathrm{sech}^{2}\tau d\tau = \pi\omega\,\mathrm{csch}\,\frac{\pi\omega}{2}\,, \tag{3.29}$$

$$\int_{-\infty}^{+\infty} \cos\omega(\tau)\,\mathrm{sech}\,\tau d\tau = \pi\,\mathrm{sech}\,\frac{\pi\omega}{2}\,, \tag{3.30}$$

evaluated by the method of residues.

Thus the Melnikov function of the system is evaluated to be

$$M(\tau_0) = -2\omega\pi\left(\omega\,\mathrm{csch}\,\frac{\pi\omega}{2} + \frac{1}{\sqrt{3}}\,\mathrm{sech}\,\frac{\pi\omega}{2}\right)\sin\omega\tau_0\,. \tag{3.31}$$

The two perturbed manifolds, stable and unstable, will touch transversely when $M(\tau_0)$ has a simple zero. As τ_0 is varied along the unperturbed separatrix, $M(\tau_0)$ varies in sign. Thus the system described by Eq. (3.15), that is the planar system in a circular orbit, perturbed by roll defined to be small and harmonic, is near-integrable and has chaotic motion near the separatrix.

One might compare this Melnikov analysis with that of Tong and Rimrott (1991), for the system consisting of the *planar* gravity gradient satellite in an orbit of small eccentricity (the system of Section 3.2.2 but general inertia ratio, small eccentricity only), or that of Koch and Bruhn (1989), for the same system but in addition small oblateness of the central body. Similarly to the system under consideration, in the above-mentioned cases small forcing but no dissipation was present and the systems were chaotic for all values of the system parameters. Later in this thesis, Melnikov's Method will be applied to the planar system in an orbit of small eccentricity and small exponential tether length rate, where the system is no longer conservative.

The system here was idealized such that the system could be considered as a peturbation of an integrable, planar system. The application of Melnikov's Method to a two degrees of freedom system assumes that the system can be considered as a perturbation of an integrable two degrees of freedom system, but this was not considered due to the complexity. The analysis presented here might lead one to expect that an application of Melnikov's Method to the more complex two degree of freedom, four dimensional system, considered as a perturbation of an integrable system, would conclude chaotic dynamics also. Note that the validity of such an analysis would be limited to small values of the perturbation parameter. In Sections 3.3.1.1 and 3.3.1.2 the near-integrability and nature of motion of the two degree of freedom system in a circular orbit, with no limiting assumptions, was seen by numerical methods.

3.3.2 Eccentric Orbit

Considering now eccentricity, the coupled motion in the stationkeeping case is governed by the equations of motion Eqs. (3.1)-(3.2), repeated here for convenience:

$$\cos^2\gamma\ \{\alpha'' - [2\gamma'\tan\gamma + F](\alpha' + 1) + 3G\sin\alpha\cos\alpha\} = 0\,,$$

$$\gamma'' - F\gamma' + \left[(1+\alpha')^2 + 3G\cos^2\alpha\right]\sin\gamma\cos\gamma = 0\,,$$

with expressions (2.28)

$$F = 2e\sin\theta/(1+e\cos\theta), \quad G = 1/(1+e\cos\theta)\,.$$

These are the governing equations of coupled motion of a gravity gradient pendulum in an elliptic orbit. This system has been studied by other authors as discussed in Section 1.2, but not in terms of the nature of (regular or chaotic) motion.

The system is nonlinear, coupled between the two degrees of freedom, and, due to the presence of eccentricity, non-autonomous. Both pitch and roll equations have parametric coeffients (due to eccentricity). Roll has no nonhomogeneous forcing; pitch is nonhomogeneously forced both by eccentricity and roll terms.

The equations of motion written with time as the independent variable, i.e., Eqs. (2.21)-(2.22) with $Q_\alpha = Q_\gamma = 0$, $\dot{\ell} = 0$ and rearranging, are

$$\ddot{\alpha} - 2\,\dot{\gamma}\,\tan\gamma\,\dot{\alpha} + (3\,\mu/R_c^3)\,\sin\alpha\,\cos\alpha = -\ddot{\theta} + 2\,\dot{\gamma}\,\tan\gamma\,\dot{\theta}\,. \tag{3.32}$$

$$\ddot{\gamma} + \left[(\dot{\alpha} + \dot{\theta})^2 + (3\,\mu/R_c^3)\,\cos^2\alpha\right]\,\sin\gamma\,\cos\gamma = 0\,. \tag{3.33}$$

From these equations, one sees clearly the excitations due to eccentricity of the orbit present in the motion. The excitation caused by the nonuniform rotation of the local vertical (position vector) appears as $\dot{\theta}(t)$ and $\ddot{\theta}(t)$. The excitation caused by the varying magnitude of the position vector appears as $R_c(t)$. The latter appears as parametric excitation for both pitch and roll motions. $\dot{\theta}(t)$ is a parametric excitation for the roll motion, while $\dot{\theta}(t)$ and $\ddot{\theta}(t)$ are nonhomogeneous excitations for the pitch motion.

Returning now to Eqs. (3.1)-(3.2), one notes that there are no equilibrium configurations (putting time derivatives to zero no constant solution can be obtained for α and γ). The system Hamiltonian is not a constant since the energy expressions are non-autonomous (Section 2.7). These effects of eccentricity were already seen in the planar case.

The system (3.1)-(3.2) is a nonautonomous, two degree of freedom system. The phase space has five dimensions, $\alpha, \alpha', \gamma, \gamma', \theta$.

The high dimensionality of the system allows in theory for the phenomenon of Arnold diffusion (see Lichtenberg and Lieberman, 1992). Consider an N degree of freedom autonomous Hamiltonian system, or an $N-1$ degree of freedom nonautonomous Hamiltonian system. Trajectories move on $2N-1$ dimensional energy surface, in $2N$ dimensional phase space for autonomous system, or in $2N-1$ dimensional phase space for nonautonomous system. Regular (integrable) KAM surfaces are N dimensional. They cannot divide space into distinct regions for $N \geq 3$, in which case all chaotic regions are connected into a single complex network, the Arnold web.

Thus, in an autonomous, two degree of freedom Hamiltonian system, or a nonautonomous one degree of freedom Hamiltonian system (as, respectively, the coupled circular orbit case, and planar elliptic orbit case studied here), in the three dimensional energy surface, or phase space, the chaotic trajectories may be isolated from one another by two dimensional KAM surfaces. In the nonautonomous, two degree of freedom system (the case of the coupled, elliptic orbit under study here), in the five dimensional phase space the chaotic trajectories are not isolated by the three dimensional KAM surfaces, but are connected in the chaotic web.

In a near-integrable Hamiltonian system of $N \geq 3$, as for smaller N, chaotic layers in phase space form near the resonances of the motion. The thickness of the layers expands with increasing perturbation away from integrability. As shown, for $N \geq 3$ the chaotic layers or regions are connected in the Arnold web. The web permeates the entire phase space. For any initial condition within the web, the chaotic trajectory will eventually intersect every finite region of the phase space, even the predominantly regular regions where the fraction of chaotic initial conditions is small. The rate at which this Arnold diffusion occurs along the web depends on the thickness of the chaotic layers and is slow, but diffusion occurs for any finite perturbation. Note that for small perturbation, for $N < 2$, chaotic motion exists but is confined to thin layers bound by regular surfaces. For $N \geq 3$ the chaotic motion is no longer confined and can diffuse throughout the phase space, but for small perturbation this diffusion along the thin layers is extremely slow.

A surface of section (Poincaré section) is a reduced phase space of dimension $2N - 2$ (see Lichtenberg and Lieberman, 1992). As shown in the previous sections, when the surface of section is two dimensional and is computed for a large number of initial conditions on the same energy surface (autonomous system) or in the phase space (nonautonomous system) it can give an immediate picture of the phase space structure. This is not the case of the present system, where the surface of section is four dimensional and more difficult to display and interpret on a two dimensional piece of paper.

The following is an analysis similar to that applied in the last section, in that numerical techniques (phase plane and time histories, PSD's, Poincaré sections, Lyapunov exponents) are used to examine the change in the nature of motion of trajectories with initial conditions at perigee $\alpha(0) = \gamma(0) = k$, $\alpha'(0) = \gamma'(0) = 0$ for increasing k, but an elliptical orbit of eccentricity of $e = 0.1$ is now considered.

From phase plane plots and time histories calculated to 80 orbits and Poincaré sections calculated to 200 orbits, it was found that for $k \leq 30°$ trajectories do not tumble up to 200 orbits, while for $k > 30°$, trajectories tumble quickly, in less than 15 orbits. The nature of motion of the libration trajectories $k \leq 30°$ is examined in the following.

Lyapunov exponents λ were calculated for the libration trajectories for increasing k, some of which are shown in Figure 3.13 (a)-(b). All λ were calculated over 200 orbits. For $k \leq 26°$, orbits appear regular, λ approaching zero over time. This is shown in Figure 3.13 (a) for $k = 10°$ and $26°$ (along with the positive λ for the chaotic orbit of $k = 30°$ for comparison) over 200 orbits. However for $k > 26°$, λ approaches a positive value denoting chaotic orbits. Figure 3.13 (b) shows this for for $k = 27°, 28°, 30°$ (along with λ for the regular orbit $k = 10°$ for comparison). Note that these positive values are low. λ, for both the cases of $28°$ and $30°$, has a value of about 0.025 at 200 orbits. λ for the $27°$ case has a value of about 0.01

at 200 orbits, very close to the value for the regular orbit $k = 26°$ (these have been plotted separately for clarity). For $k \leq 26°$, λ appears to approach zero smoothly, if asymptotically. For $k = 27°$, λ over time appears to approach a low positive value and thus indicate the limit of weak chaos.

From Figure 3.13 (b), the $k = 28°$ and $30°$ trajectories can be considered to share the same λ and to belong to the same chaotic region; however, the $k = 27°$ trajectory has a clearly distinct λ, denoting another, segregated chaotic region. This serves as an argument that if Arnold diffusion occurs, it occurs too slowly to be observed numerically over 200 orbits. In theory, the chaotic regions of a high dimensional system such as this one are connected by the Arnold web, through which a chaotic trajectory will diffuse. In this case a trajectory beginning in a weak chaotic region should after sufficient time be found in a strong region, and take on the λ of the strong region (the trajectory will rarely return to the thin layers of a weak region since they make up a negligible fraction of the web). Lichtenberg and Lieberman (1992) review the work of Benettin et al. (1980) and Contopoulos et al. (1978) who made similar observations for their particular high dimensional system. They found that chaotic trajectories belonged to apparently segregated chaotic regions with distinct λ, and it was concluded that Arnold diffusion, if it occurs at all, happens too slowly to be observed numerically over the time frame studied.

In summary, for libration trajectories $k \leq 30°$, the Lyapunov exponents show that up to 200 orbits, two main regions exist for increasing k: a regular region for $k \leq 26°$, and a weakly chaotic region for $27° \leq k \leq 30°$. The chaotic region appears to be subdivided into unconnected component regions. Arnold diffusion, if it exists as predicted by theory, occurs too slowly to be observed numerically over 200 orbits.

The transition from regular to chaotic motion as k is increased, for the libration trajectories $k \leq 30°$, was examined further, using phase planes and time histories, PSD's and Poincaré sections.

Phase planes and time histories were taken of the trajectories to 80 orbits. Some of these ($k = 10°, 22°, 23°, 26°, 27°, 28°, 30°$) are shown in Figure 3.14. While in the phase plane trajectories appear to wander more as k is increased, little can be extracted from the phase planes and time histories (thus the need for other computational tests such as Lyapunov exponents to identify the nature of motion).

Power spectra were taken of the libration trajectories under 80 orbits, some of which (those corresponding to the phase planes and time histories presented in Figure 3.14) are shown in Figure 3.15.

The PSD for $k = 10°$, that is initial conditions $\alpha(0) = \gamma(0) = 10°$, $\alpha'(0) = \gamma'(0) = 0$, can be compared with Figure 3.8 (b), with the same initial conditions in a circular orbit, and Figure 3.4, with initial conditions $\alpha(0) = 10°$, $\alpha'(0) = 0$ in a planar orbit of the same eccentricity as considered here ($\epsilon = 0.1$). Frequency components are combination tones of the three frequencies of the orbital frequency, and the pitch and roll natural frequencies of the linearized system (1, $\sqrt{3}$, and 2 times the orbital frequency, respectively). The frequency components of the pitch PSD's of the planar, elliptic case and coupled, circular orbit case appear in the pitch PSD as well as other combinations. In particular, both forcing frequencies, the parametric and nonhomogeneous forcing orbital frequency and the nonhomogeneous forcing frequency of twice the roll fundamental, are seen. The frequency components of the roll PSD of the coupled, circular orbit case appear as well as other combinations. In particular, the parametric forcing orbital frequency can be seen.

The transition to chaotic motion as k is increased cannot be sharply defined in this case using the PSD's, due to the weak nature of the chaotic motion for libration.

As k is increased the PSD contains more frequency components. The PSD's for $k \leq 22°$ definitely indicate regular motion with distinct and identifiable components. Local broadening of a few frequency spikes which should indicate a very weak chaotic motion can be found for $23° \leq k \leq 26°$. This broadening of the spectra is more predominant for $k \geq 27°$, but still somewhat local, as chaos is weak. Trajectories for $k < 27°$ are judged regular however, as indicated by the Lyapunov exponents, due to the somewhat more subjective interpretation of weak chaotic motion as it appears in the power spectra.

Finally, surface of sections were taken of the individual libration trajectories for increasing k. As mentioned above the surface of section has $2N - 2$ dimensions (see Lichtenberg and Lieberman, 1992). For $N \geq 3$, the $N - 1$ number of two dimensional (generalized coordinate-velocity) projections of the surface of section may be used to visualize the trajectory. However for $N \geq 3$, even for a regular trajectory, the trajectory intersections generally fill an annulus of finite area on each projection, with thickness related to the nearness to exact separability of the trajectory in the coordinates (if regular and exactly separable, the annulus reduces to a smooth curve). The intersections of such a regular trajectory with the surface of section lie in an $N - 1$ dimensional surface, whose projection is a finite area. The intersections of a chaotic trajectory fills a $2N - 2$ dimensional volume within the $2N - 2$ dimensional surface of section, whose projection is also an area. Thus for $N \geq 3$ the surface of section is less useful for determining nature of motion. The surface of section has been used to illustrate Arnold diffusion over long times in some systems, where the intersections of the chaotic trajectory eventually spread throughout the projections.

For the present case the four dimensional surface of section was taken by sampling $\alpha, \alpha', \gamma, \gamma'$ at $\theta = constant \equiv n2\pi$, $n = 0, 1, 2, \ldots$, i.e., at perigee, and the $\alpha - \alpha'$ and

$\gamma-\gamma'$ projections examined. Surfaces of section were taken of the libration trajectories over 200 orbits. The projections of some of these are shown in Figure 3.16 (those corresponding to the presented phase planes, time histories and PSD's, $k = 10°$, $22°$, $23°$, $26°$, $27°$, $28°$, $30°$). For $k = 10°$, the annuli approximate smooth curves, indicating a regular trajectory which is separable: for small motions the equations approximately decouple. As k is increased, the thickness of the annuli generally increases, since the coupling is stronger. The pitch annuli gradually approach a form resembling that of the libration chaotic region observed for the circular orbit case: however, the figures give little indication as to at what k motion changes from regular to chaotic motion, which is not unexpected from the discussion above. The projections for larger k known to be chaotic from the Lyapunov exponents and PSD's ($k \geq 27°$) were observed also at intermediate times: motion is well confined to the annuli from early times and there is no evidence of diffusion to the 200 orbits taken.

The results presented above for the coupled motion elliptic orbit case can be summarized as follows. Numerical techniques were applied to examine the change in the nature of motion of trajectories with initial conditions $\alpha(0) = \gamma(0) = k$, $\alpha'(0) = \gamma'(0) = 0$, in an orbit of eccentricity $e = 0.1$, as k is increased. The Lyapunov exponents show that, for libration trajectories $k \leq 30°$ up to 200 orbits, two main regions exist for increasing k: a regular region for $k \leq 26°$, and a weakly chaotic region for $27° \leq k \leq 30°$. The chaotic region appears to be subdivided into unconnected component regions. Arnold diffusion, if it exists as predicted by theory, occurs too slowly to be observed numerically over 200 orbits. The transition from regular to chaotic libration with increasing k is not sharply defined by power spectra due to the weak level of chaos of libration, but power spectra confirm that the libration trajectories of $27° \leq k \leq 30°$ are weakly chaotic. Due to the high dimensionality of the system. the Poincaré sections as viewed in projections were not useful in identifying the change from regular to chaotic libration with increasing k; however. those of the libration trajectories known to be chaotic from Lyapunov exponents and power spectra. $27° \leq k \leq 30°$. confirm that Arnold diffusion is not observed numerically over 200 orbits.

The results are now compared with those obtained in the coupled motion circular orbit case and the planar motion elliptic orbit case of the previous sections.

First the effects of eccentricity and out-of-plane motion on the size of the regular libration region is examined.

Results can be compared directly with those of the series of computational tests for increasing initial conditions $\alpha(0) = \gamma(0) = k$. $\alpha'(0) = \gamma'(0) = 0$ carried out similarly in the coupled motion circular orbit case. In that case a change from regular to chaotic libration was observed at $k = 43°$; in the present case of orbit eccentricity $\epsilon = 0.1$. the change to chaotic libration was observed at $k = 27°$. The eccentricity causes chaotic libration to occur at a lower k. i.e. a reduction of the regular libration region for those initial conditions. One expects the regular libration region as a whole (all possible initial conditions) is decreased. and that it decreases with increasing eccentricity in general. as observed in the planar case: results at other initial conditions and eccentricity to show this could be obtained in future work. In the planar case. of course. chaotic motion exists only with nonzero eccentricity.

Results can also be compared with Figure 3.3 for the planar case of an elliptic orbit of $\epsilon = 0.1$. Inspection of the Poincaré section showed that a change from regular pitch libration to chaotic pitch tumbling occurs. for zero initial pitch rate. at the initial pitch angle $\alpha(0) \sim 40°$. i.e. initial conditions $\alpha(0) \sim 40°$. $\gamma(0) = \alpha'(0) = \gamma'(0) = 0$. In the present case where roll was given identical initial angle as pitch. the change from regular to chaotic libration was observed at $\alpha(0) = \gamma(0) = 27°$, $\alpha'(0) = \gamma'(0) = 0$. Introduction of a disturbance in roll angle identical to that in pitch angle for zero disturbances in the velocities, causes chaotic motion to occur at a lower pitch angle disturbance, i.e., reduces the regular pitch libration region for initial conditions of initial pitch angle and zero initial pitch rate. One expects the regular pitch libration region as a whole (all possible initial conditions) decreases with the introduction of any roll motion, for any given eccentricity; this was the case in the circular orbit problem. Of course in the circular orbit case chaotic motion exists only when both degrees of freedom are present. The above discussion is understood by recognizing that both eccentricity and out of plane motion introduce additional dimensions to the phase space and possible resonances of motion; chaotic layers form near the associated separatrices.

The regular libration region may be smaller or equal to just the the libration region of non-tumbling motion, depending on whether chaotic libration or chaotic tumbling occurs. In the planar motion, elliptic orbit case, chaotic motion is only chaotic tumbling, and the regular libration region is equal to the total libration region, as seen in the Poincaré sections (Figure 3.3). In the Poincaré sections (Figure 3.5) for constant Hamiltonian of the coupled motion, circular orbit case, one sees the regular libration region is surrounded by chaotic libration or chaotic tumbling, depending on the Hamiltonian. In the $\alpha(0) = \gamma(0) = k$, $\alpha'(0) = \gamma'(0) = 0$ series of that system, k for regular libration was limited by chaotic libration for $43° \leq k \leq 48°$, with tumbling motion occurring only for $k \geq 49°$. In the same series for the coupled elliptic orbit case with $e = 0.1$, k for regular libration was limited by chaotic libration for $27° \leq k \leq 30°$, with tumbling motion occurring only for $k \geq 31°$. Thus the coupled motion elliptic orbit case is more similar to the coupled motion circular orbit case than the planar elliptic orbit case in that chaotic libration may occur, which limits regular libration to a region smaller than that of just the libration region of non-tumbling motion.

The Lyapunov exponents taken in the chaotic libration range of the $\alpha(0) = \gamma(0) = k$, $\alpha'(0) = \gamma'(0) = 0$ series of the coupled motion circular and $e = 0.1$ orbit cases, that is $43° \leq k \leq 48°$, $27° \leq k \leq 30°$ respectively, can be seen from Figures 3.10 and 3.13(b) to show that chaotic libration in the $\epsilon = 0.1$ case is weaker than in the circular case. The range in itself is smaller for the $\epsilon = 0.1$ case, 4° compared to 6°.

For the initial conditions studied for the elliptic orbit case $e = 0.1$ the difference in size between libration region and regular libration region due to chaotic libration is small (a few degrees), and the chaotic libration is weakly chaotic. However the desirable region of operation when the nature of motion is considered is reduced, and one must recognize this may occur for all initial conditions and for all eccentricity.

A comparison is made finally of the coupled motion elliptic orbit case, with previous work of interest. Modi and Shrivastava (1971b) presented design plots indicating allowable impulsive disturbances (initial pitch rate, roll rate, zero initial angles) at perigee for nontumbling motion over a range of ϵ of this system, showing a decrease in the libration region with eccentricity. They did not consider the nature of libration however, and one expects chaotic libration would restrict the desirable region of operation to a smaller regular libration region, also decreasing with eccentricity, as shown in this work for equal angular disturbances (initial pitch angle, roll angle, from rest) at perigee in orbits of $\epsilon = 0$ and $\epsilon = 0.1$. For a slightly elliptical orbit, Melvin (1988b) observed a similar type of instability (chaos) for the two degrees of freedom plotted on a unit sphere, for the same region, that is motions from rest with small initial roll angle, large initial pitch angle, as he observed for the circular orbit case; in addition he observed in this region that the tether sometimes inverts (tumbling).

However, Melvin (1988b) did not apply any of the computational tests which decide the nature of solution, as carried out here. The results here presented PSD's and Lyapunov exponents which decide the nature of motion in this system, as well as Poincaré sections, phase plane plots and time histories, to document the change from regular to chaotic motion for trajectories starting at perigee from rest with equivalent initial pitch and roll angles as the angle is increased, in an orbit of $e = 0.1$. The regular libration region for those initial conditions and eccentricity was determined and the existence of chaotic solutions in this system (coupled motion, elliptic orbit), as suggested by Melvin (1988b), was confirmed.

From a practical point of view the results of importance presented in this Section and Chapter is the determination of the regular libration region of the phase space, the desirable region of operation of the system. This region is clear for the circular orbit case from its phase plane: chaos does not occur in this one degree of freedom system. This region can also be seen from the Poincaré section of the planar elliptic case for initial conditions at perigee ($e = 0.003, 0.1$), and the Poincaré sections for constant values of the Hamiltonian for the coupled motion circular orbit case. In these cases the regular libration region of desired operation should exclude the 'island' regions which are surrounded by chaos, although they correspond to regular libration trajectories. In these systems (nonautonomous one degree of freedom, autonomous two degrees of freedom) chaotic trajectories exist from theory even in regular regions: however, they are very weakly chaotic, confined to very thin layers between regular trajectories and in practice behave as regular trajectories. Only when these chaotic layers overlap and create a large chaotic region are the characteristics of chaos shown. Large excursions of the trajectories may occur within the region, and motion is unpredictable. The regular libration region was also determined for the coupled motion circular orbit case and coupled motion $e = 0.1$ orbit case for initial conditions at perigee of equal pitch and roll angles, zero velocities. The elliptic case is a non-autonomous two degrees of freedom system. In this case the theory predicts chaotic trajectories even in the regular regions: however, they are very weakly chaotic, whose rate of diffusion in very thin layers is so slow that although the layers are connected in a chaotic web throughout the phase space the trajectories in practice behave as regular trajectories.

3.4 Computational Notes

In this Chapter, as well as Chapter 4, numerical solutions of the differential equations of motion were obtained using the IMSL subroutine DIVPRK, which uses Runge Kutta formulas of order five and six. The routine is a variable step size scheme which attempts to keep the global error proportional to a user-specified tolerance. In this work absolute error control was selected, with tolerance of 5×10^{-5}.

Validation of the scheme is particularly important for the solutions of this Chapter. Error arises due to the discretization involved in the numerical work, specifically the truncation error of the numerical integration routine and the roundoff error produced in the computer. One would like to ensure that the chaotic numerical solutions represent the dynamics and are not spurious, produced by discretization effects. The essential correctness of the solutions can be checked by varying the numerical precision of the routine, and the algorithm itself; the Hamiltonian can also be used as a check for the case where the dynamics require it to be a constant of the motion.

The Hamiltonian is a constant of the motion for the circular orbit case. The Hamiltonian was checked for all numerical results presented in the coupled motion, circular orbit section, Section 3.3.1, that is the trajectories associated with all Poincaré sections, phase plane plots and time histories, PSD's and Lyapunov exponents. All showed excellent behaviour of the Hamiltonian, that is constant with time, within at most ± 0.0001 of the value of the Hamiltonian constant C_H (Figure 3.17, C_H as a function of time for the chaotic trajectory included in Figure 3.5 (d), is an example). As the minimum absolute value of C_H of all presented trajectories was 0.5, this corresponds to a maximum percentage variation of $\pm 0.02\%$. This variation is small, ensuring the validity of the computed trajectories.

For the trajectory of coupled motion, elliptic orbit, $\alpha(0) = \gamma(0) = 30°$, $\alpha'(0) = \gamma'(0) = 0$, the Lyapunov exponent was recomputed over 200 orbits using a stricter tolerance, 5×10^{-10}, and also by another numerical integrator altogether. As the alternate integrator the IMSL subroutine DIVPBS was used. DIVPBS employs the algorithm of Burlisch and Stoer, which uses rational function extrapolation and is based on the midpoint rule in a slightly modified form. Like DIVPRK the routine is a variable step size scheme which attempts to keep the global error proportional to a user-specified tolerance. Absolute error control and tolerance of 5×10^{-5} was selected as done originally with DIVPRK.

In Figure 3.18 these Lyapunov exponents are shown for comparison with the original calculated Lyapunov exponent included in Figure 3.13. Discrepancy in the values, which signify a weakly chaotic orbit, is observable only after 150 orbits and remains small to the 200 orbits shown. The numerical calculation can be considered essentially independent of the precision of the integrator and the integrator itself. Although other results of the elliptic orbit coupled motion case were not directly verified in this way, they are assumed to be also valid.

Finally one notes the agreement obtained where direct comparisons could be made with numerical results available in the literature, that is some Poincaré sections for the planar motion elliptic orbit case and the coupled motion circular orbit case.

For the solutions of this Chapter. the integrator subroutine was called 150 times per orbit. that is every $\Delta\theta = 2\pi/150 \simeq 0.042$ radian or $2.4°$.

To plot the time histories. the angular displacement is taken at every $\Delta\theta = 2\pi/75$. Likewise angular displacement and velocity is taken at every $\Delta\theta = 2\pi/75$ to construct the phase plane plots.

To construct the power spectra. the time history sampled at every $\Delta\theta = 2\pi/75$ is used. A $n = 4096$ point fast Fourier transform (FFT) is taken. using the FFT subroutine provided in MATLAB. The power spectral density is found as the square of the absolute value of the complex transform. normalized by the number of data points. It is converted to a decibel scale. and the first $n/2$ points are graphed against the nondimensional frequency vector $\omega_{i+1} = 2\pi i/(n\Delta\theta)$. $i = 0, 1, \ldots, n/2 - 1$.

Concerning the Poincaré sections. for the elliptic orbit planar and coupled motion cases. angular dispacement(s) and velocity(-ies) are sampled at perigee every orbit as discussed. For the circular orbit coupled motion case. where pitch and pitch rate are to be sampled when $\gamma = 0$ and $\gamma' > 0$ as discussed. the former condition is effected by testing for a change of sign after every call.

Details of the computation of the first Lyapunov exponent λ can be found in Moon (1987). Rasband (1990). Lichtenberg and Lieberman (1992) and Tabor (1989).

To determine the length ratio d/d_0 in Eq.(3.12). that is

$$\lambda = \lim_{N\to\infty} \frac{1}{t_N - t_0} \sum_{k=1}^{N} \log_2 \frac{d(t_k)}{d_0(t_{k-1})} \tag{3.34}$$

the variational equations can be used.

For the system

$$\dot{x}_i = f_i(\bar{x}, t), \quad i = 1, \ldots, n \tag{3.35}$$

the variational vector function $\bar{\eta}$ of trajectories in the neighbourhood of the reference trajectory $\bar{x}^*(t)$ is solved from

$$\dot{\bar{\eta}} = [A] \cdot \bar{\eta} \, . \tag{3.36}$$

where

$$[A] = \frac{\partial \bar{f}}{\partial \bar{x}}(\bar{x}^*(t)) \tag{3.37}$$

is the Jacobian matrix function for the vector field $\bar{f}$ evaluated along the trajectory $\bar{x}^*(t)$.

Eqs.(3.35) and (3.36) can be integrated simultaneously: the former solves for the given trajectory $\bar{x}^*(t)$, the latter for the variational vector function $\bar{\eta}(t)$ along the trajectory $\bar{x}^*(t)$. One chooses for convenience $|\bar{\eta}(0)| = 1$, but the initial direction is chosen arbitrarily (it will then likely have a component in the direction of most rapid growth, associated with the first Lyapunov exponent, to which the solution $\bar{\eta}(t)$ converges). After a given time interval $t_{k+1} - t_k = \tau$, one takes

$$\frac{d(t_{k+1})}{d(t_k)} = \frac{|\bar{\eta}(\tau; t_k)|}{|\bar{\eta}(0; t_k)|} \tag{3.38}$$

Before beginning the next time interval in Eq.(3.34) the distance is renormalized:

$$\bar{\eta}(0; t_k) = \frac{\bar{\eta}(\tau; t_k)}{|\bar{\eta}(\tau; t_k)|} \tag{3.39}$$

In this work the true anomaly θ acts as the time variable. Renormalization was carried out every $2\pi/15 \simeq 0.42$ radians (15 times per orbit).

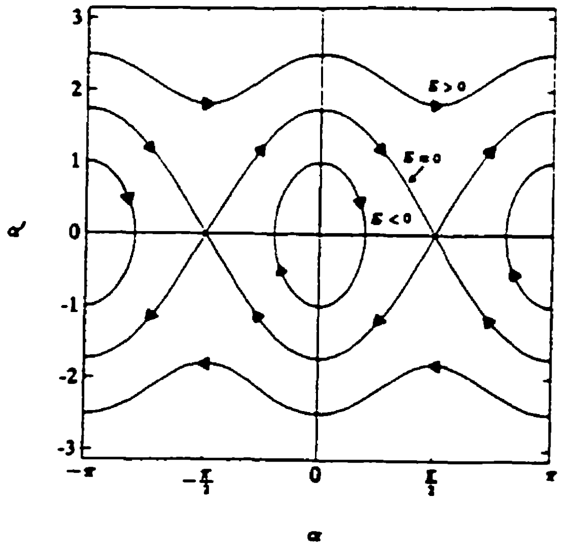

Figure 3.1: Phase Plane of Planar Constant Length Tethered System (Gravity Gradient Pendulum) in a Circular Orbit

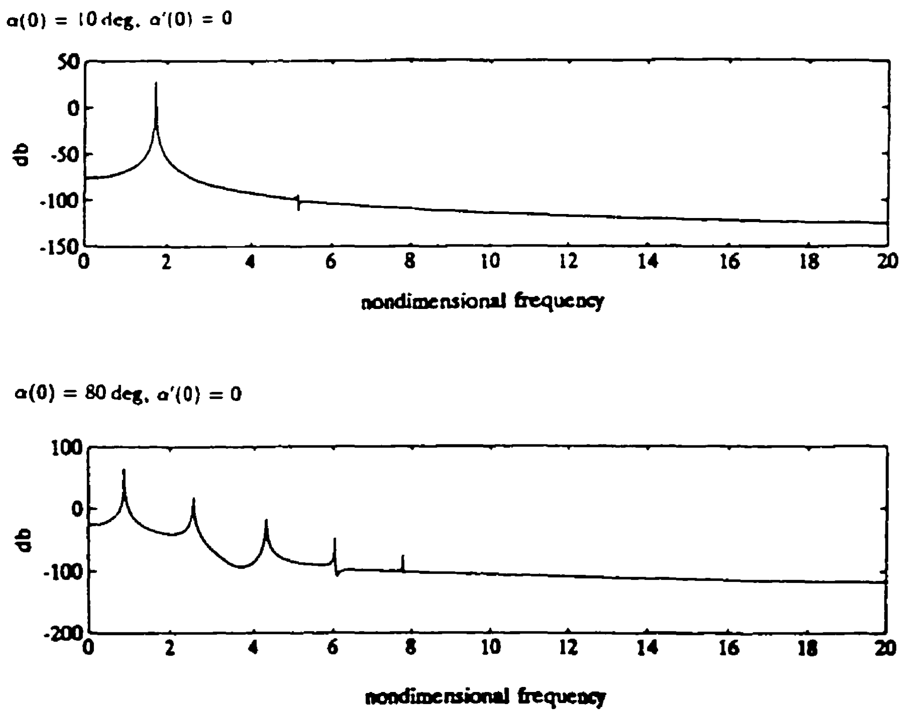

Figure 3.2: PSD's of Motion of Planar Constant Length Tether in a Circular Orbit with Initial Conditions as Shown

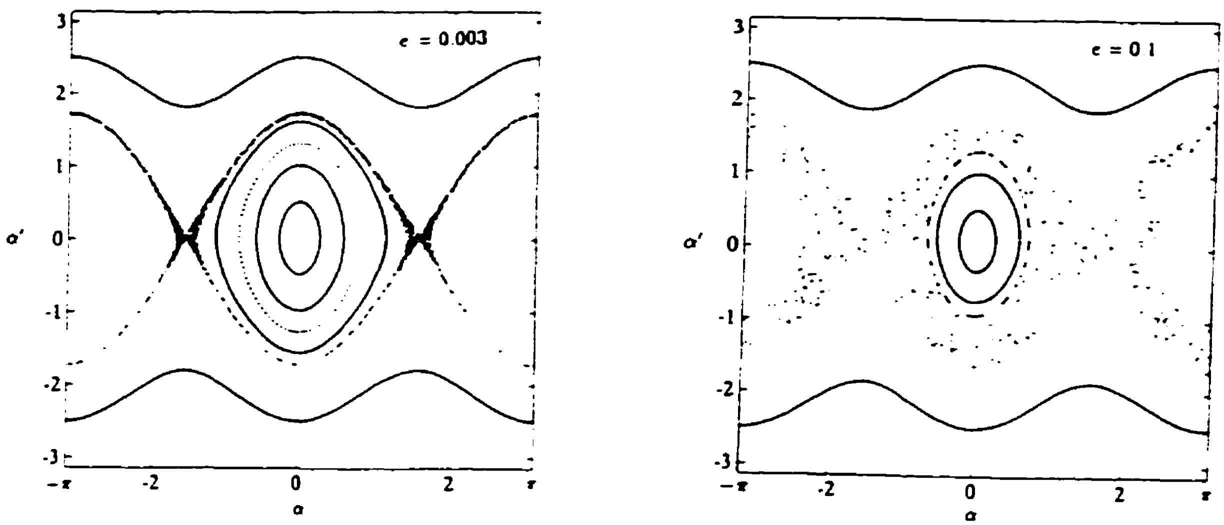

Figure 3.3: Poincaré Plots for Motion of a Planar Constant Length Tethered System in Orbits of Eccentricity $e = 0.003$ and $e = 0.1$

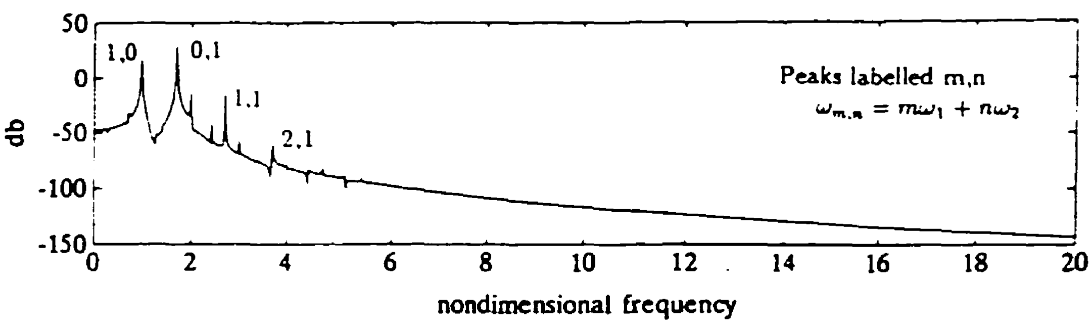

Figure 3.4: PSD of Motion of Planar Constant Length Tethered System in an Orbit of Eccentricity $e = 0.1$, with Initial Conditions $\alpha(0) = 10°, \alpha'(0) = 0$

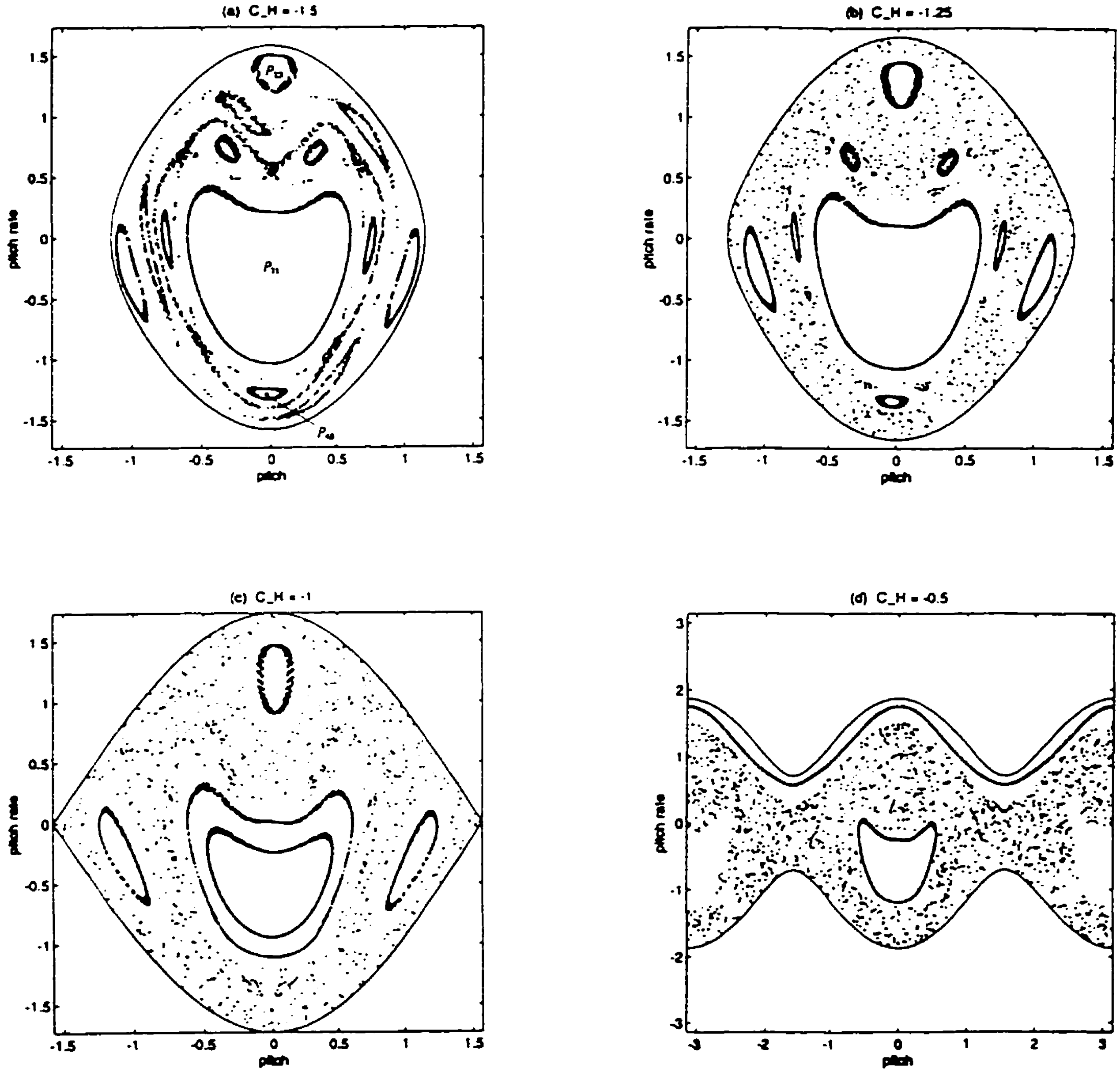

Figure 3.5: Series of Poincaré Sections for Increasing Values of Hamiltonian Constant C_H (Several Initial Conditions at a Given C_H), Constant Length Tethered System in a Circular Orbit. Note P_{mn} in the figure is meant to identify the regular regions associated with the periodic solution, not the periodic solution itself. Note $P_m n$ has n regular regions of which only one is labelled here.

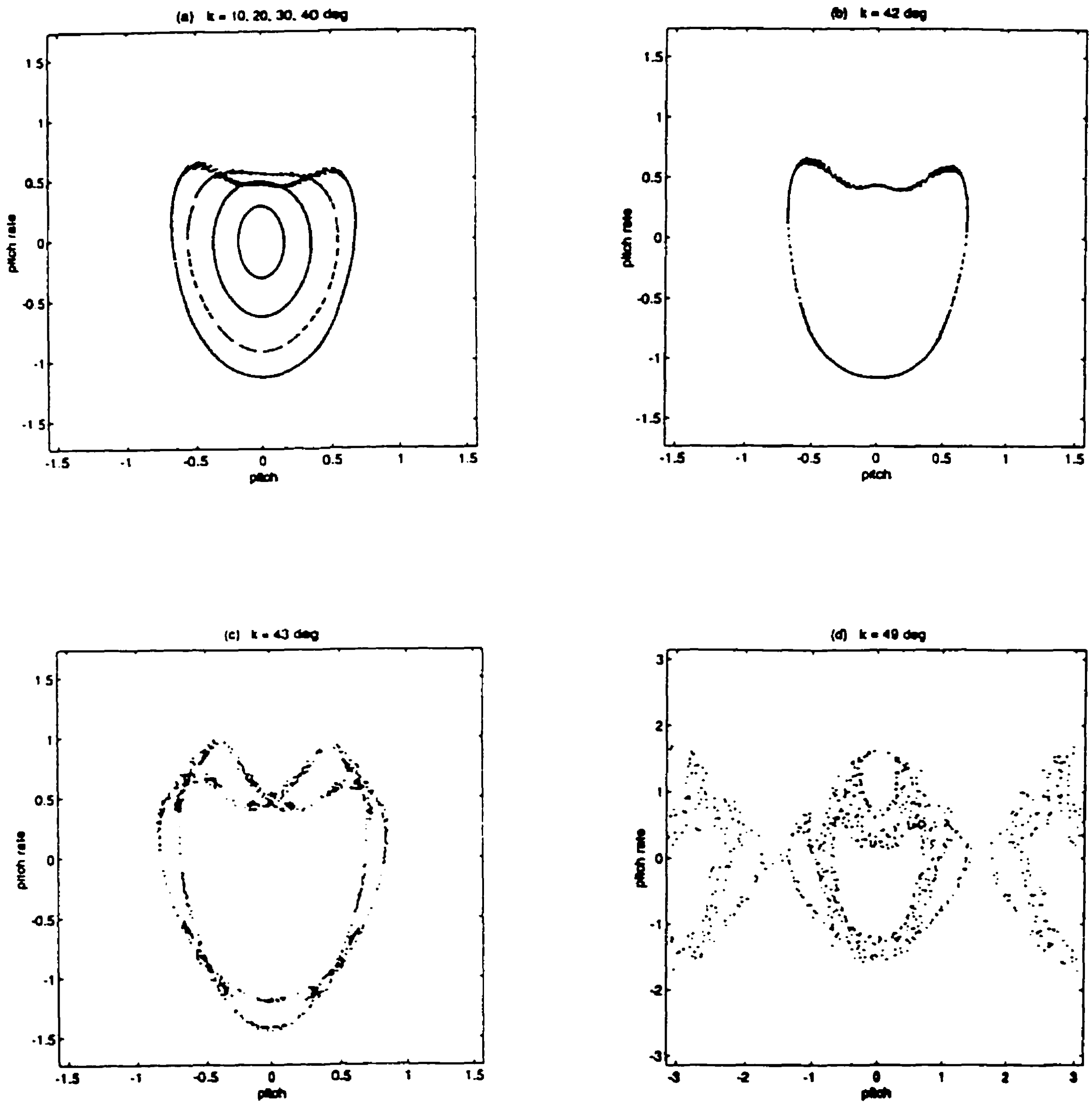

Figure 3.6: Poincaré Sections of Motion with Initial Conditions $\alpha(0) = \gamma(0) = k$, k as shown, $\alpha'(0) = \gamma'(0) = 0$, Constant Length Tethered System in a Circular Orbit

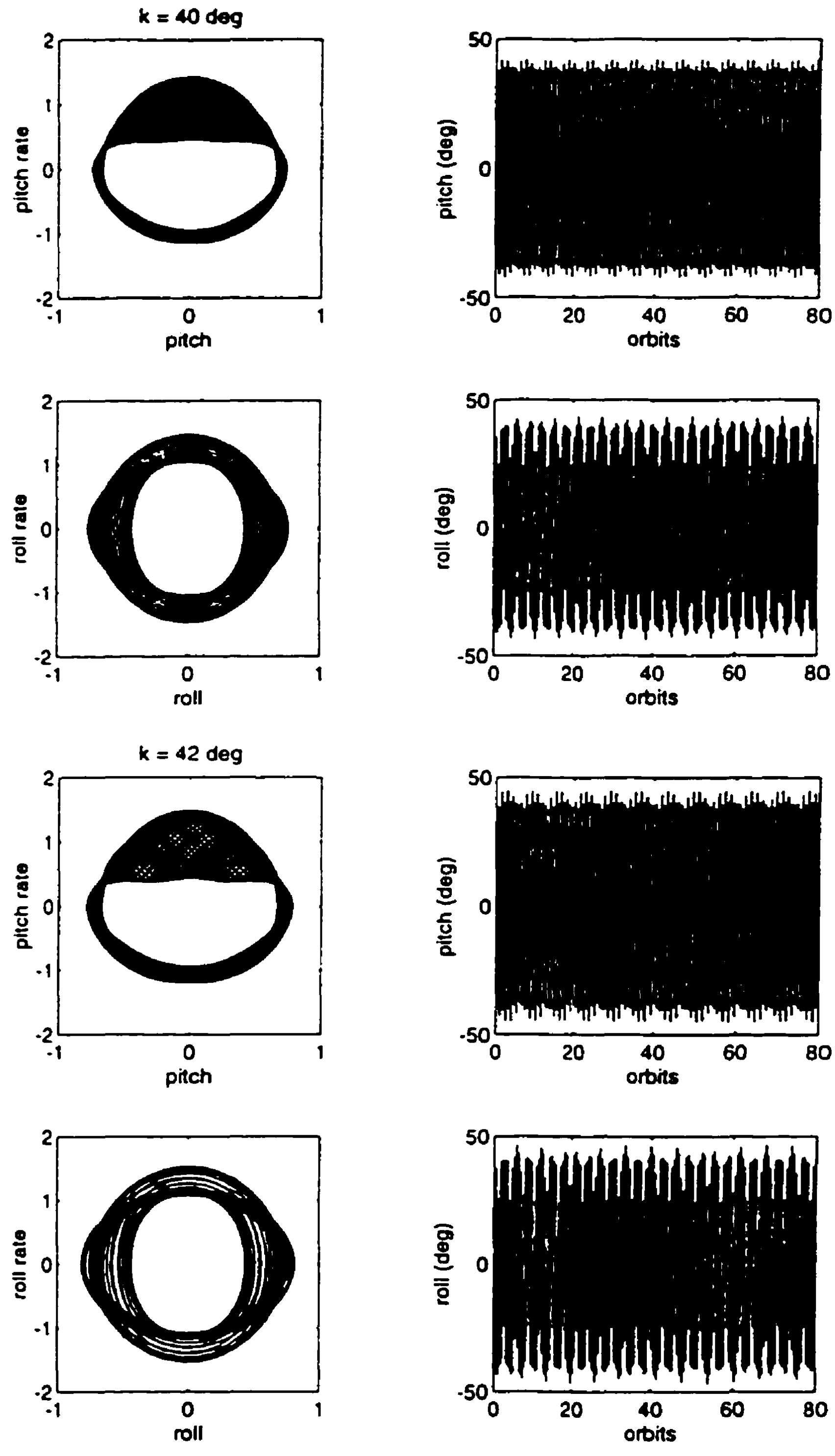

Figure 3.7: Phase Planes and Time Histories of Motion with Initial Conditions $\alpha(0) = \gamma(0) = k$, k as shown, $\alpha'(0) = \gamma'(0) = 0$, Constant Length Tethered System in a Circular Orbit

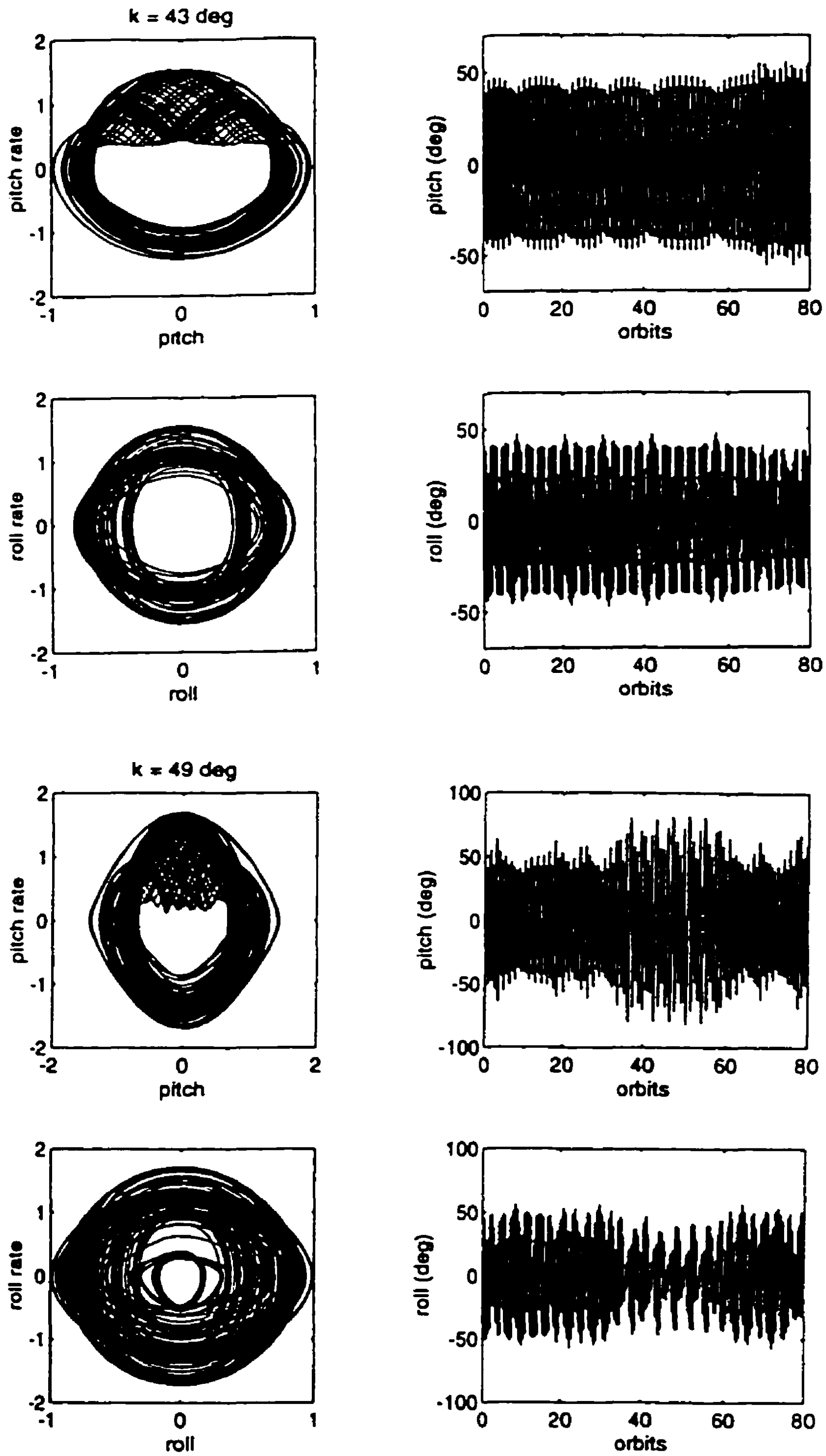

Figure 3.7 (continued)

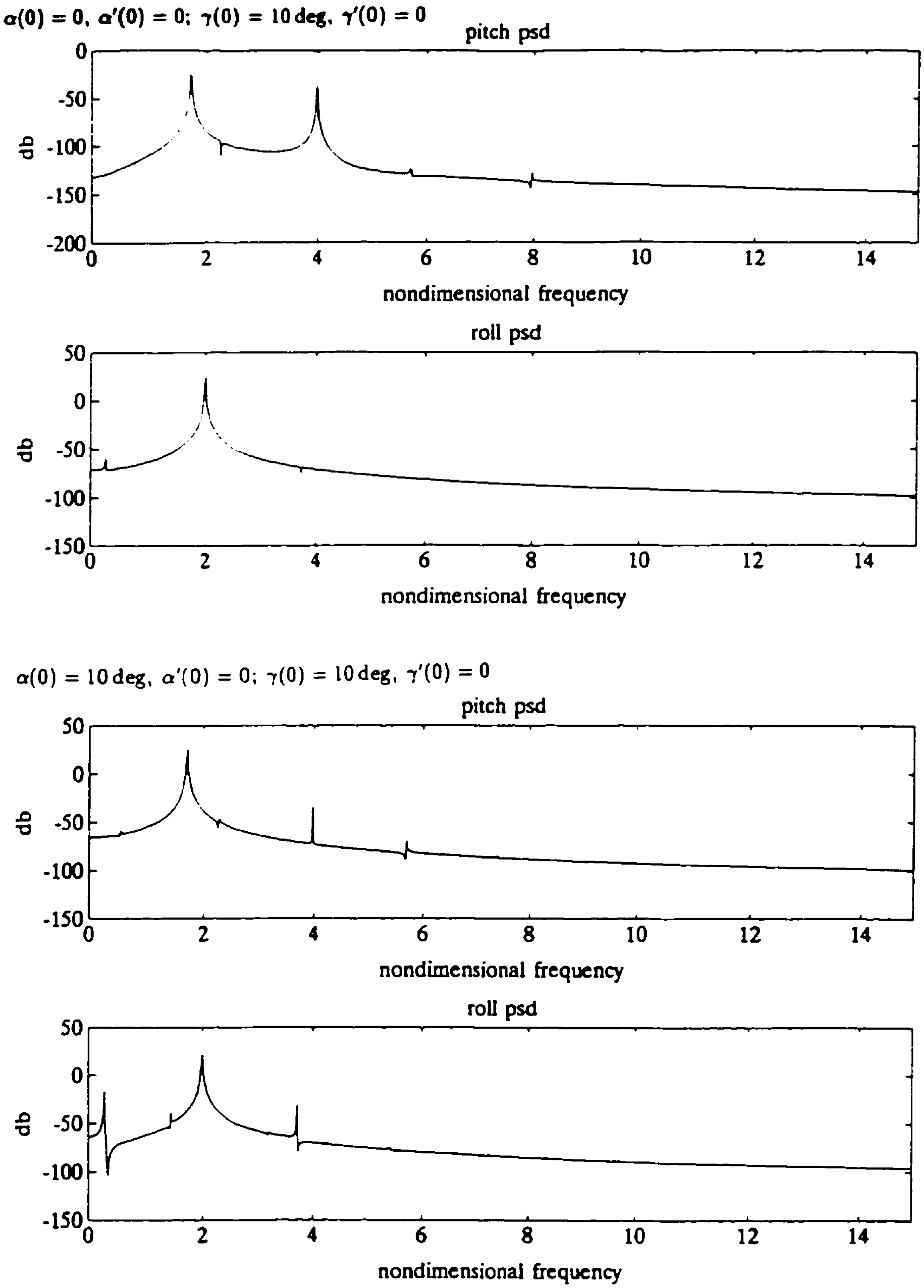

Figure 3.8: PSD's of Motion with Initial Conditions (a) $\alpha(0) = 0, \gamma(0) = 10°$, $\alpha'(0) = \gamma'(0) = 0$ (b) $\alpha(0) = \gamma(0) = k = 10°$, $\alpha'(0) = \gamma'(0) = 0$, Constant Length Tethered System in a Circular Orbit

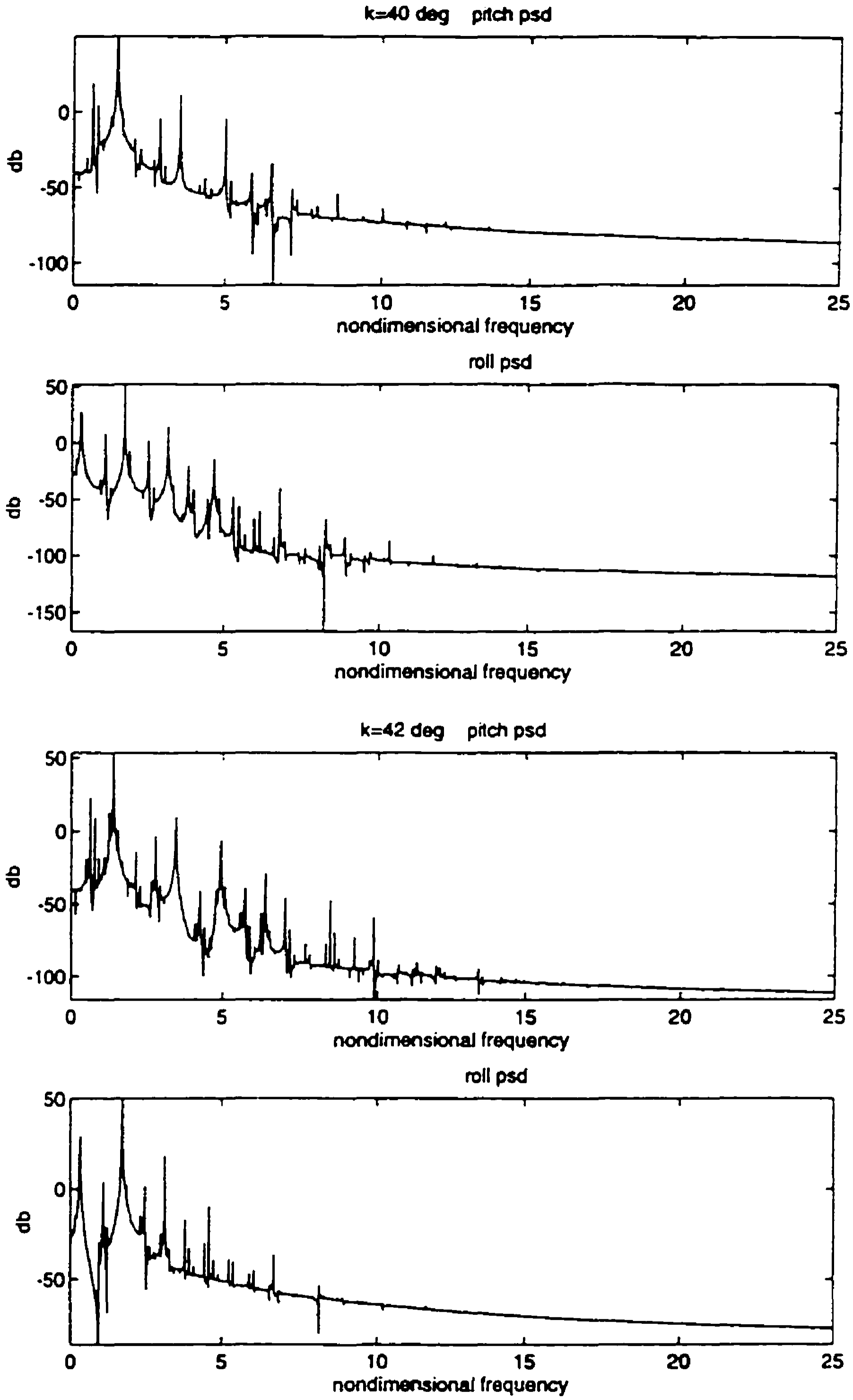

Figure 3.9: PSD's of Motion with Initial Conditions $\alpha(0) = \gamma(0) = k$, k as shown, $\alpha'(0) = \gamma'(0) = 0$, Constant Length Tethered System in a Circular Orbit

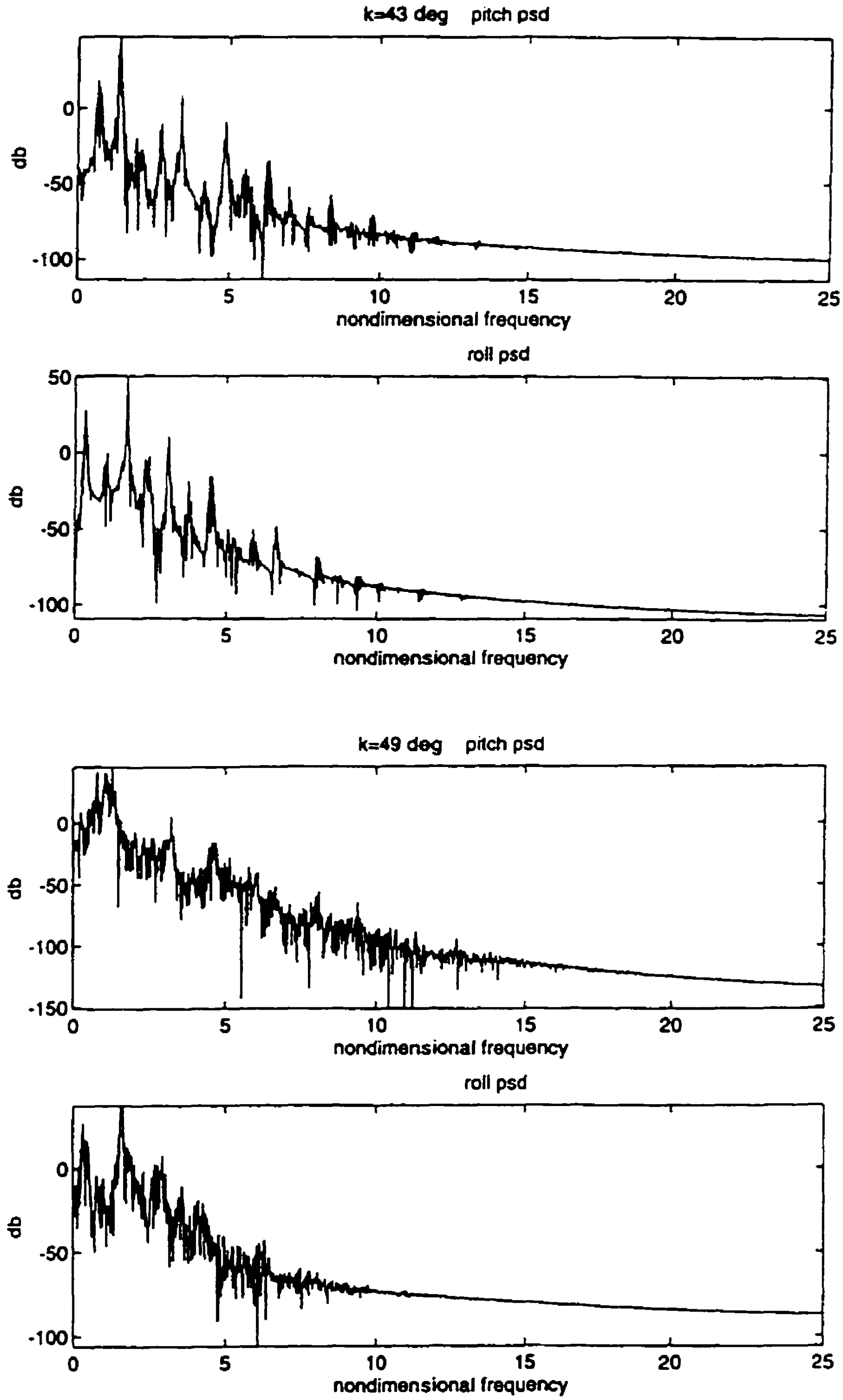

Figure 3.9 (continued)

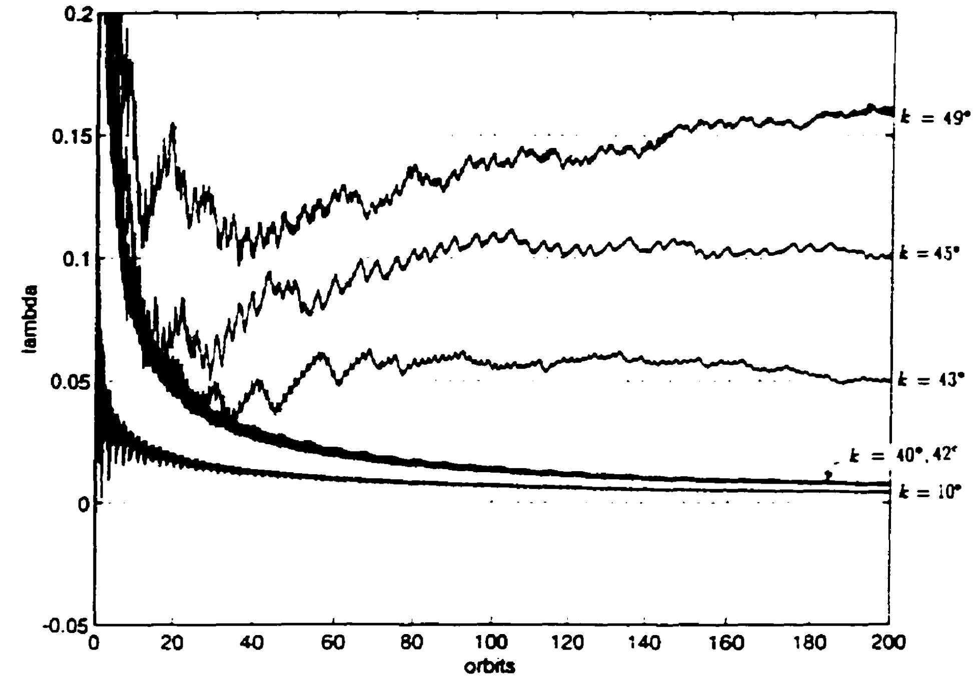

Figure 3.10: Lyapunov Exponents of Motion with Initial Conditions $\alpha(0) = \gamma(0) = k$, k as shown. $\alpha'(0) = \gamma'(0) = 0$. Plotted Over 200 Orbits. Constant Length Tethered System in a Circular Orbit

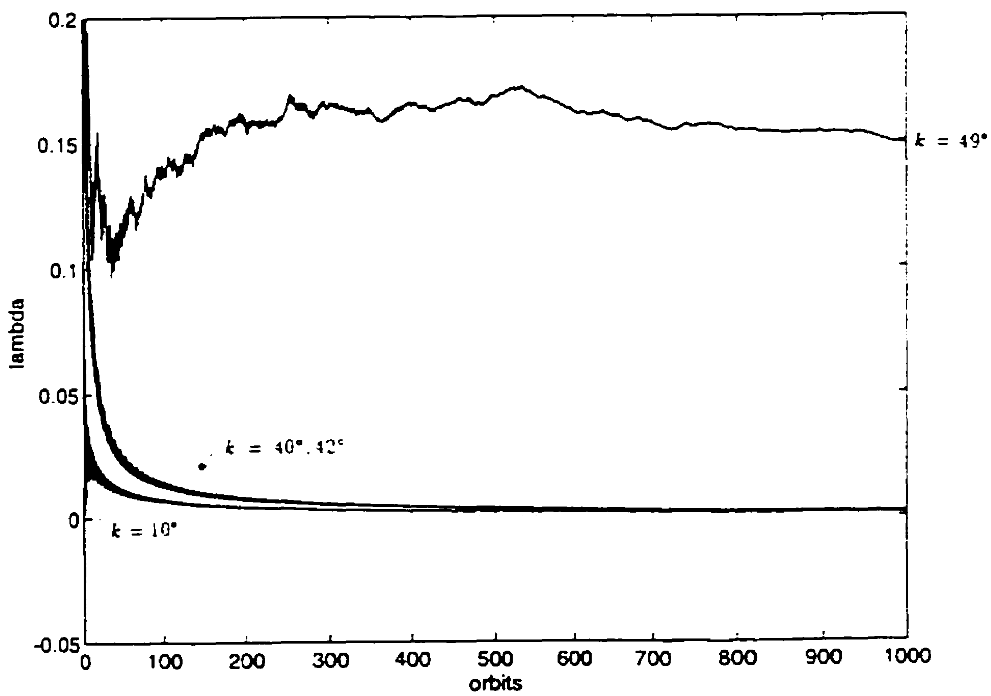

Figure 3.11: Lyapunov Exponents of Motion with Initial Conditions $\alpha(0) = \gamma(0) = k$, k as shown. $\alpha'(0) = \gamma'(0) = 0$. Plotted Over 1000 Orbits. Constant Length Tethered System in a Circular Orbit

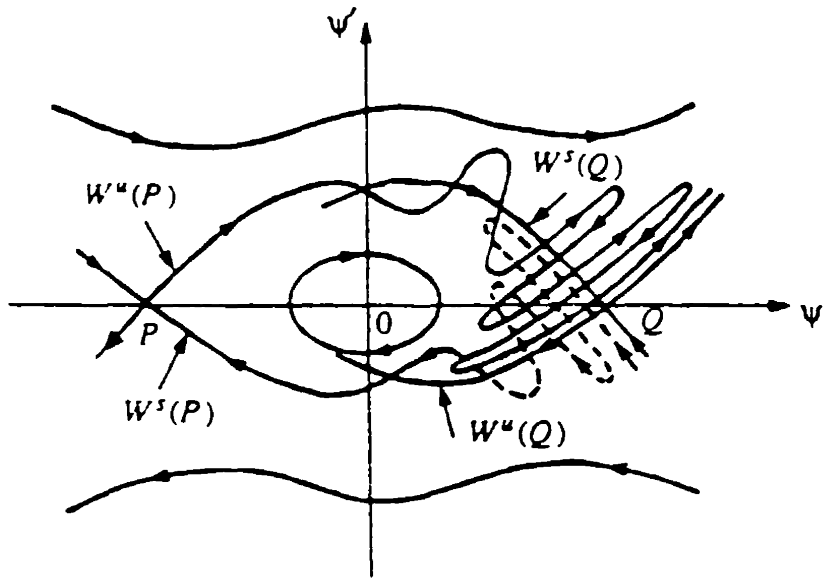

Figure 3.12: Sketch of Separation and Transverse Intersection of Stable and Unstable Manifolds of Saddle Point of Poincaré Section of Integrable System Under Integrability-Breaking Perturbation (figure from Tong and Rimrott, 1991a)

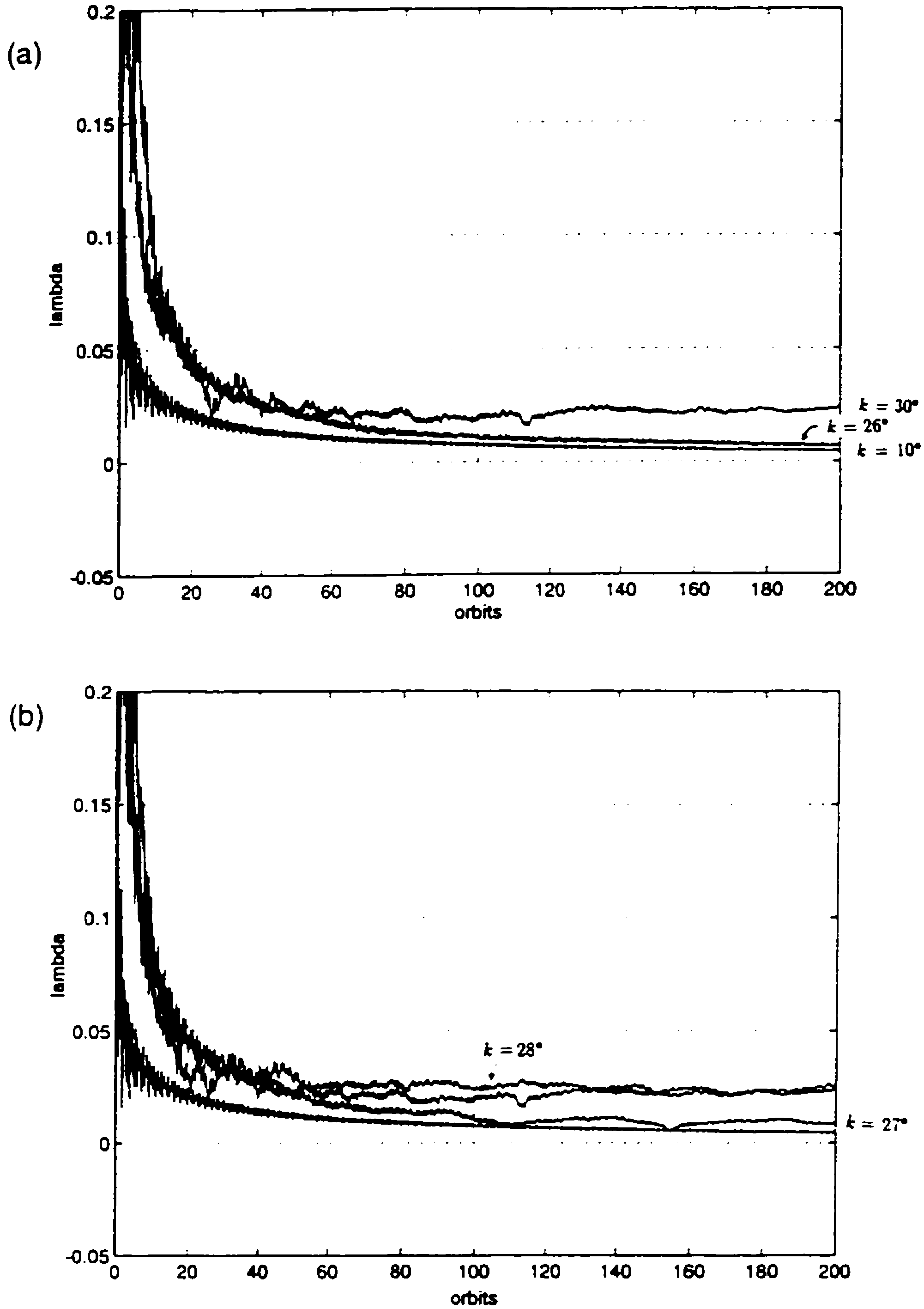

Figure 3.13: Lyapunov Exponents of Motion with Initial Conditions $\alpha(0) = \gamma(0) = k$, k as shown. $\alpha'(0) = \gamma'(0) = 0$. Plotted Over the Number of Orbits Shown. Constant Length Tethered System in an Orbit of $e = 0.1$

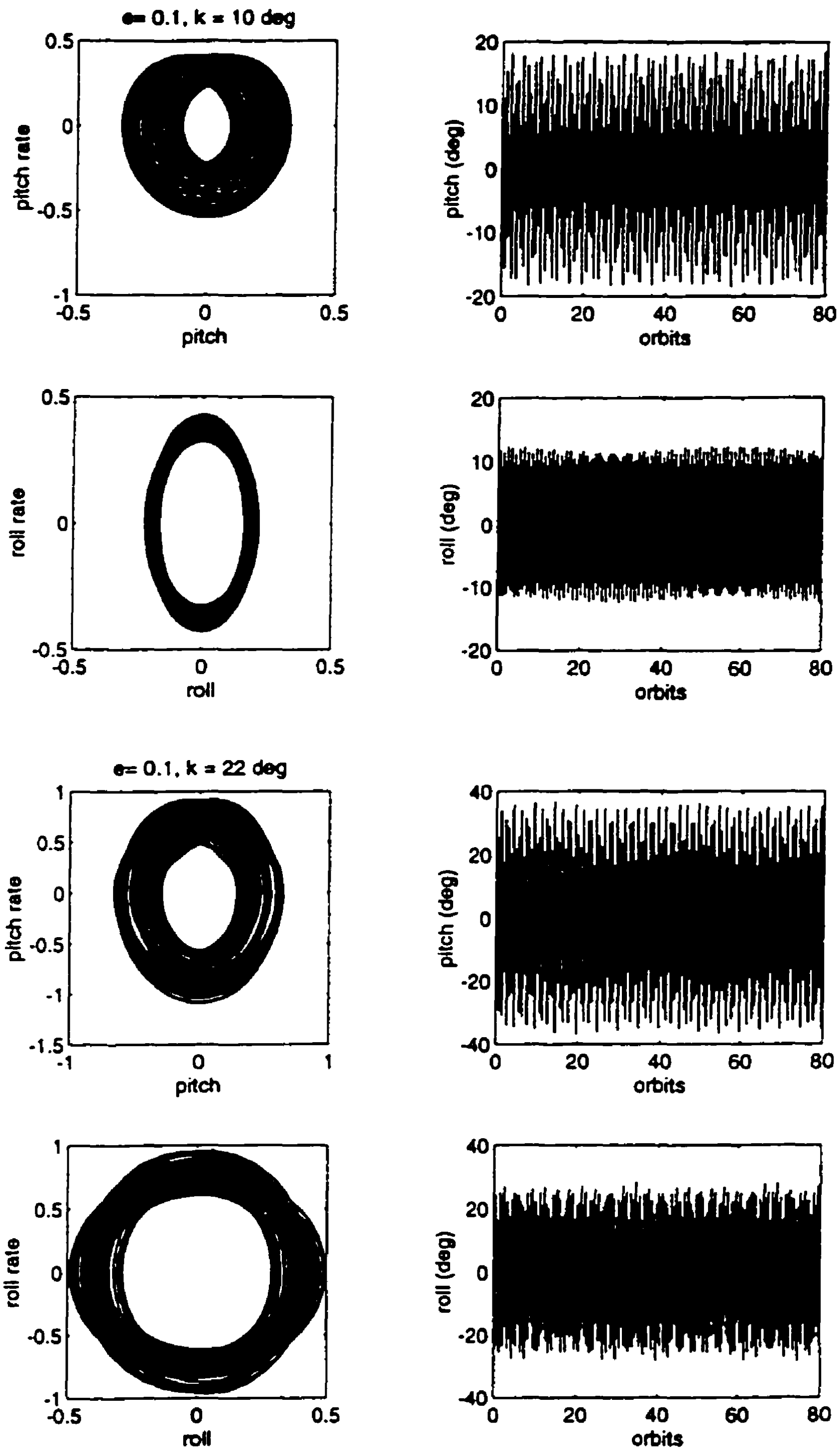

Figure 3.14: Phase Planes and Time Histories of Motion with Initial Conditions $\alpha(0) = \gamma(0) = k$, k as shown, $\alpha'(0) = \gamma'(0) = 0$, Constant Length Tethered System in an Orbit of $e = 0.1$

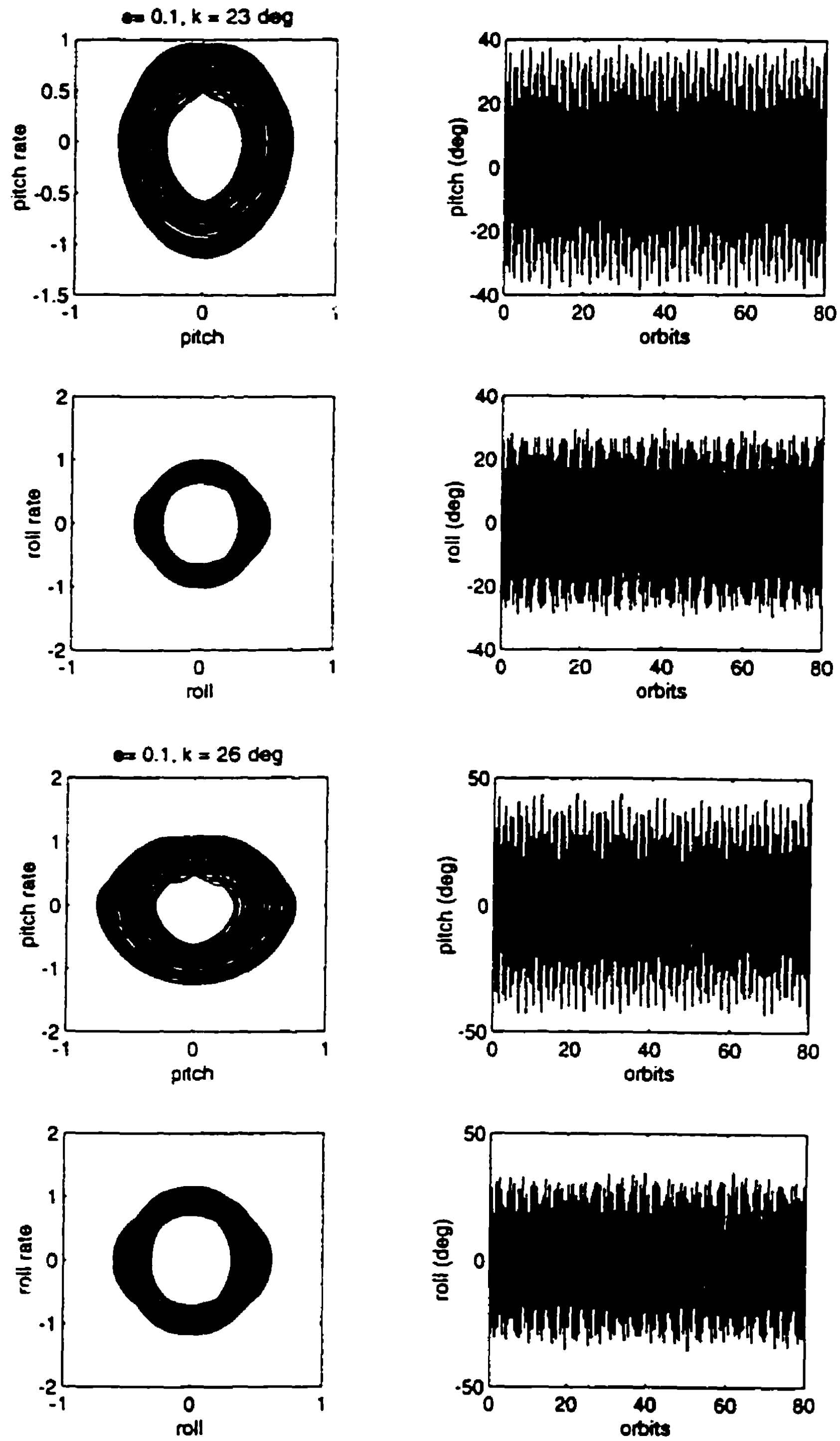

Figure 3.14 (continued)

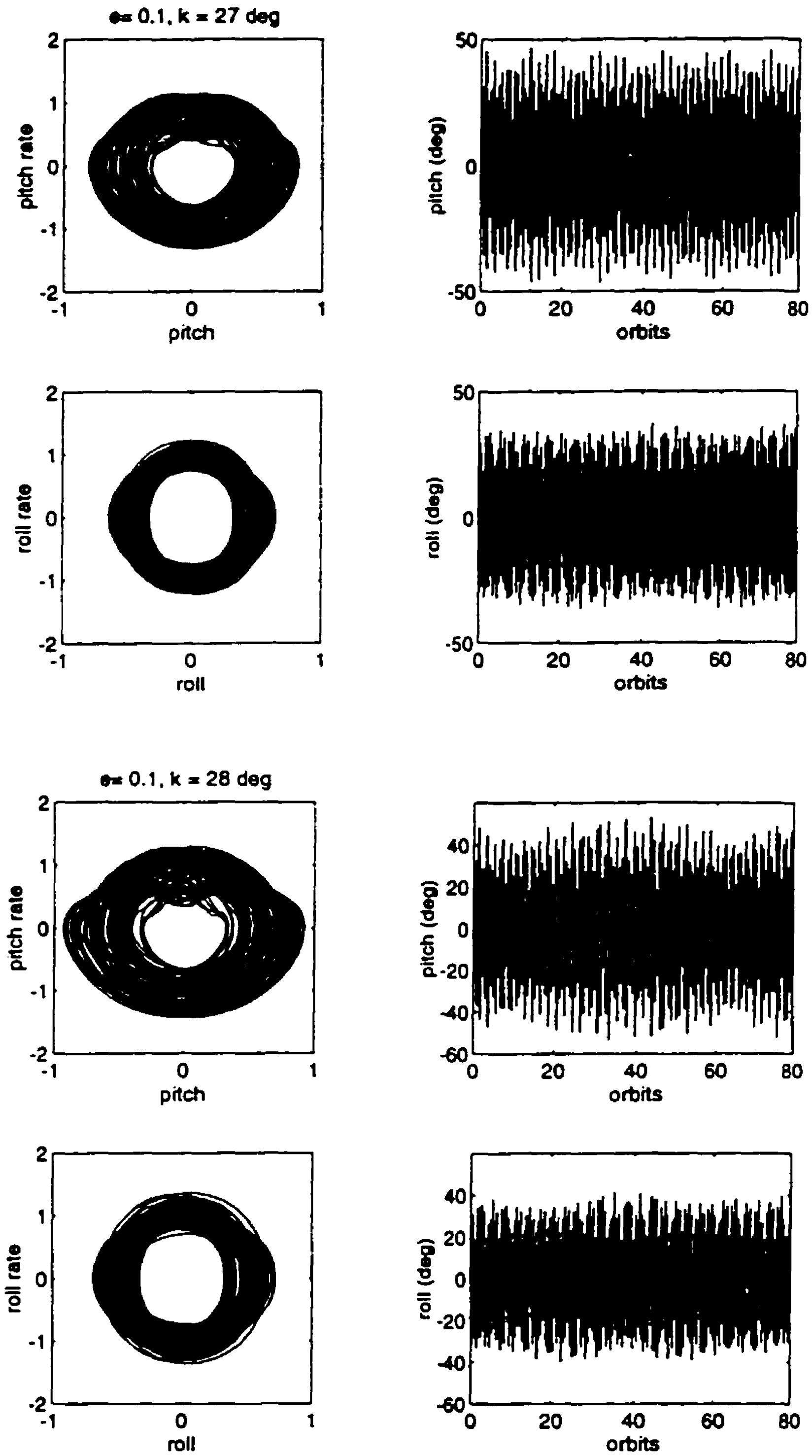

Figure 3.14 (continued)

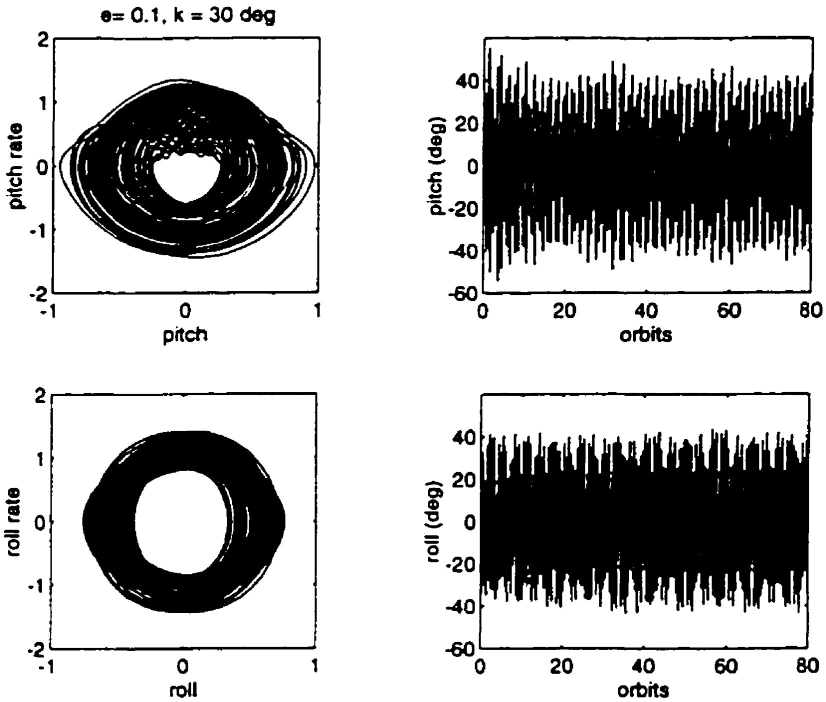

Figure 3.14 (continued)

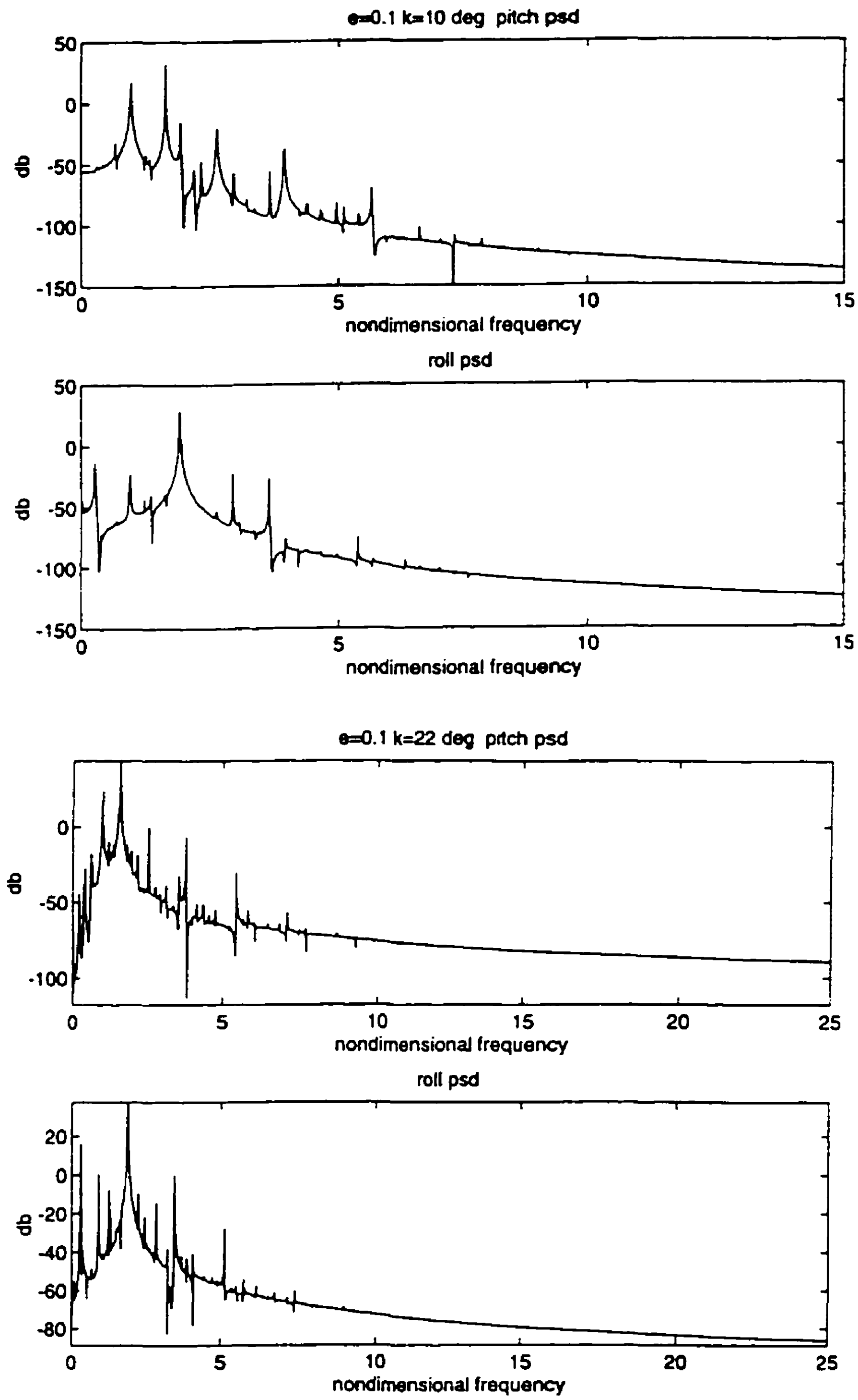

Figure 3.15: PSD's of Motion with Initial Conditions $\alpha(0) = \gamma(0) = k$, k as shown, $\alpha'(0) = \gamma'(0) = 0$. Constant Length Tethered System in an Orbit of $e = 0.1$

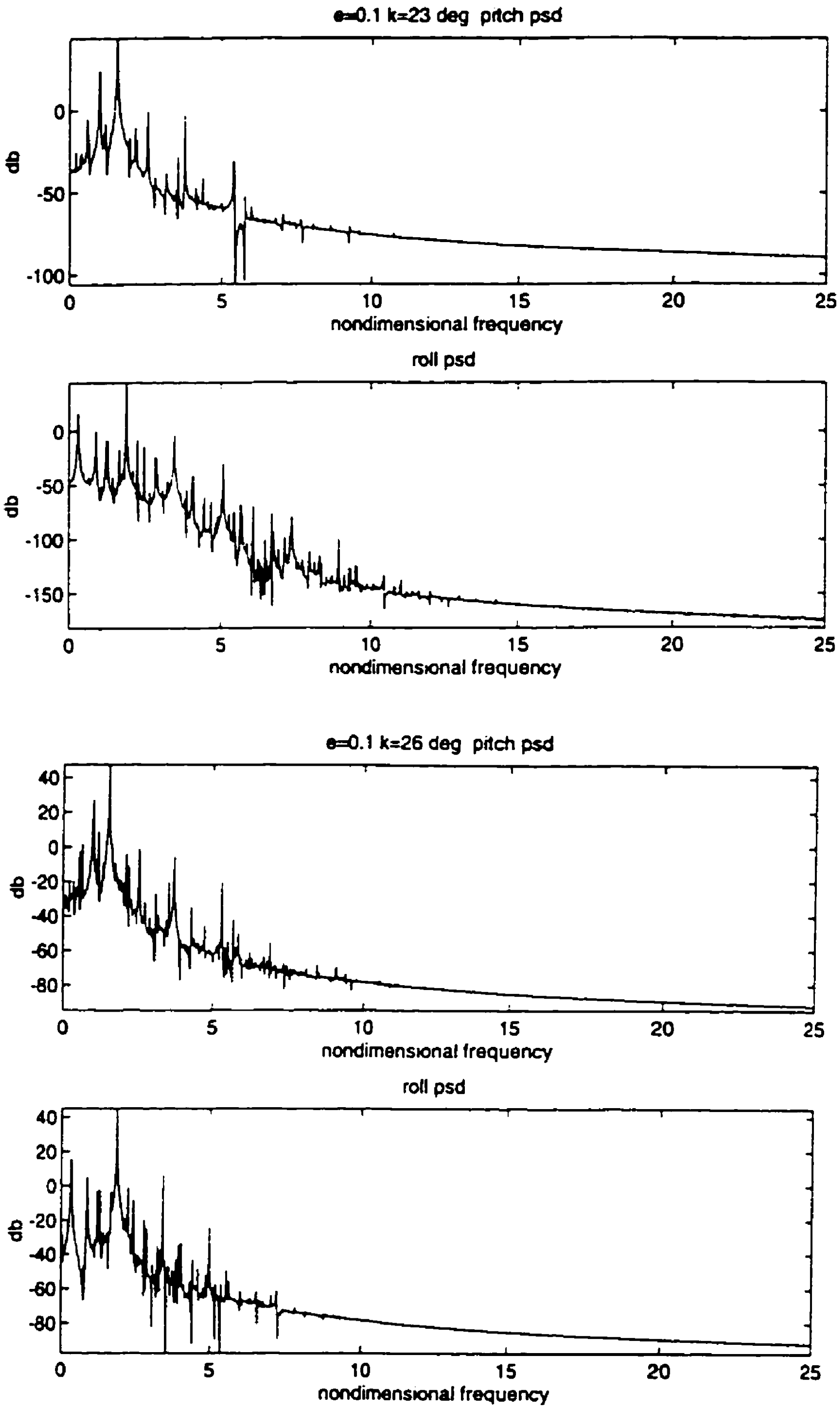

Figure 3.15 (continued)

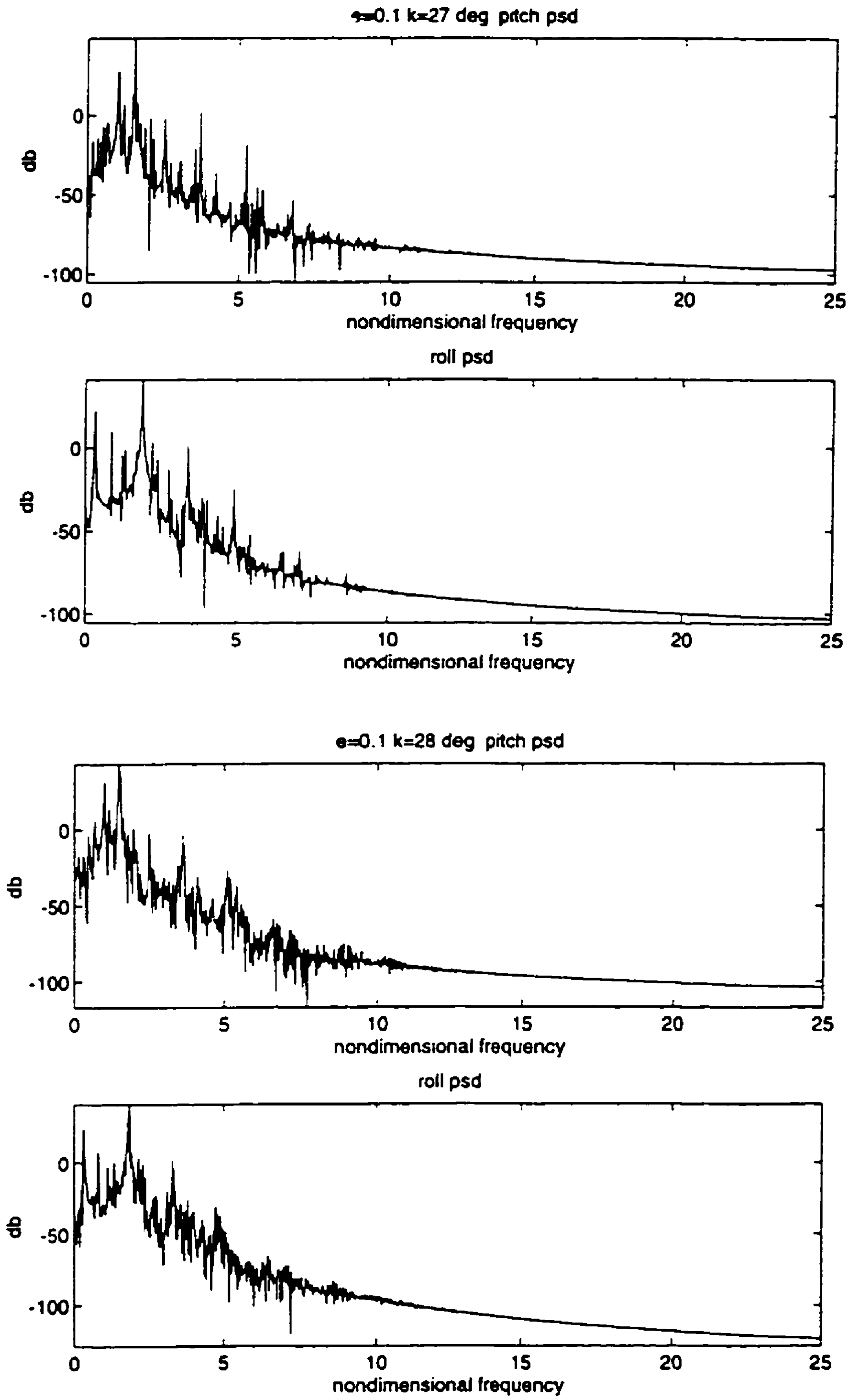

Figure 3.15 (continued)

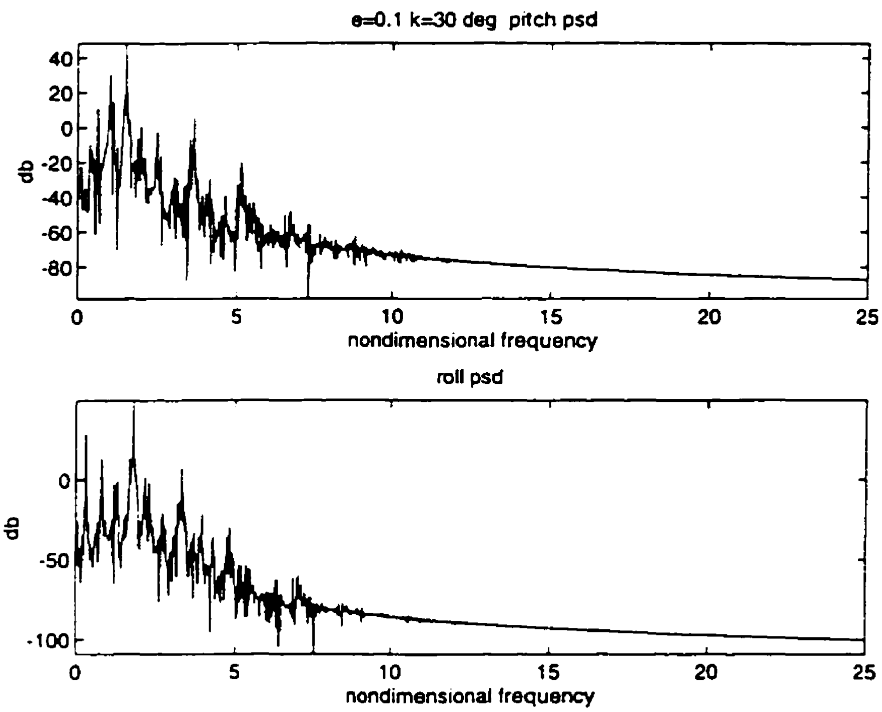

Figure 3.15 (continued)

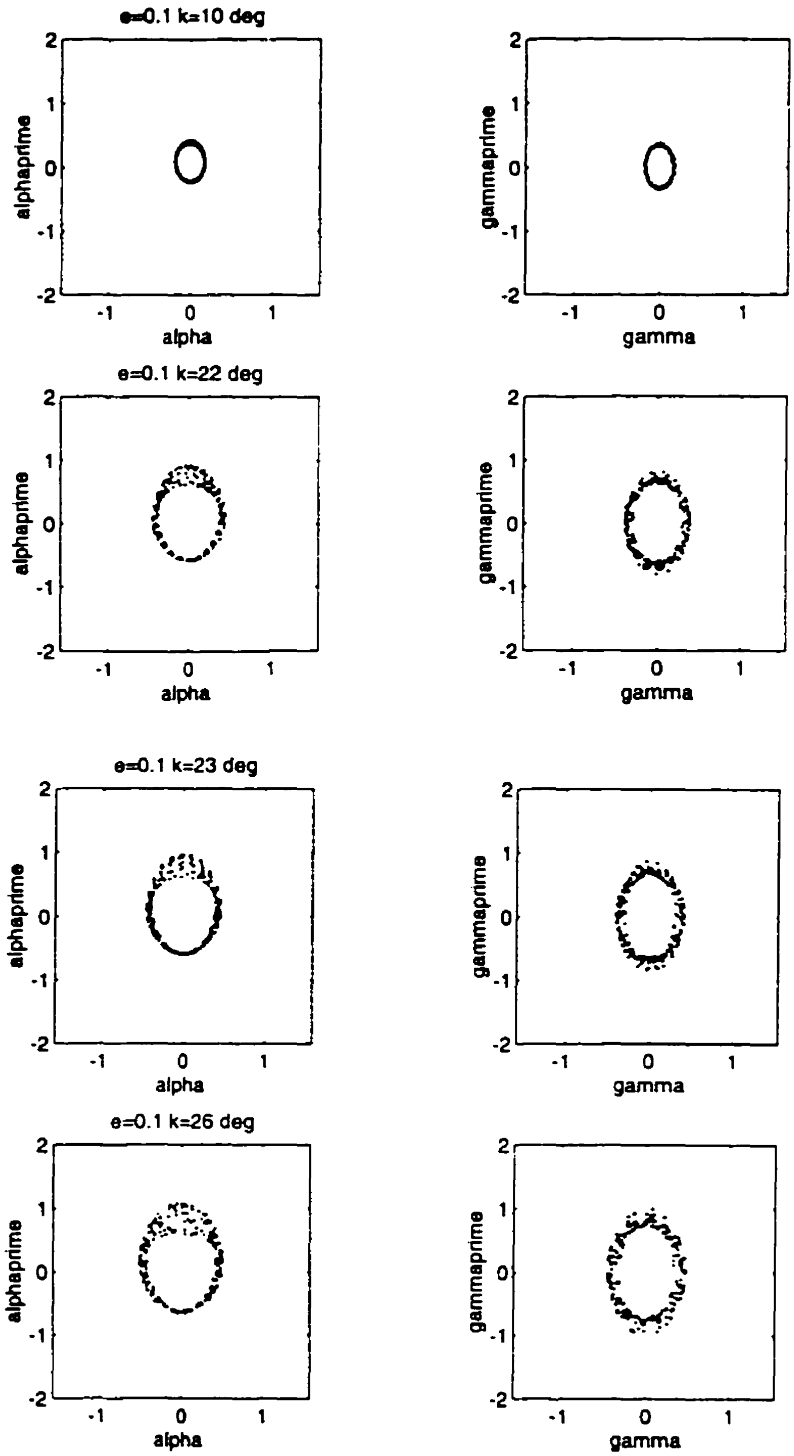

Figure 3.16: Projections of the Poincaré Sections of Motion with Initial Conditions $\alpha(0) = \gamma(0) = k$. k as shown. $\alpha'(0) = \gamma'(0) = 0$. Constant Length Tethered System in an Orbit of $\epsilon = 0.1$

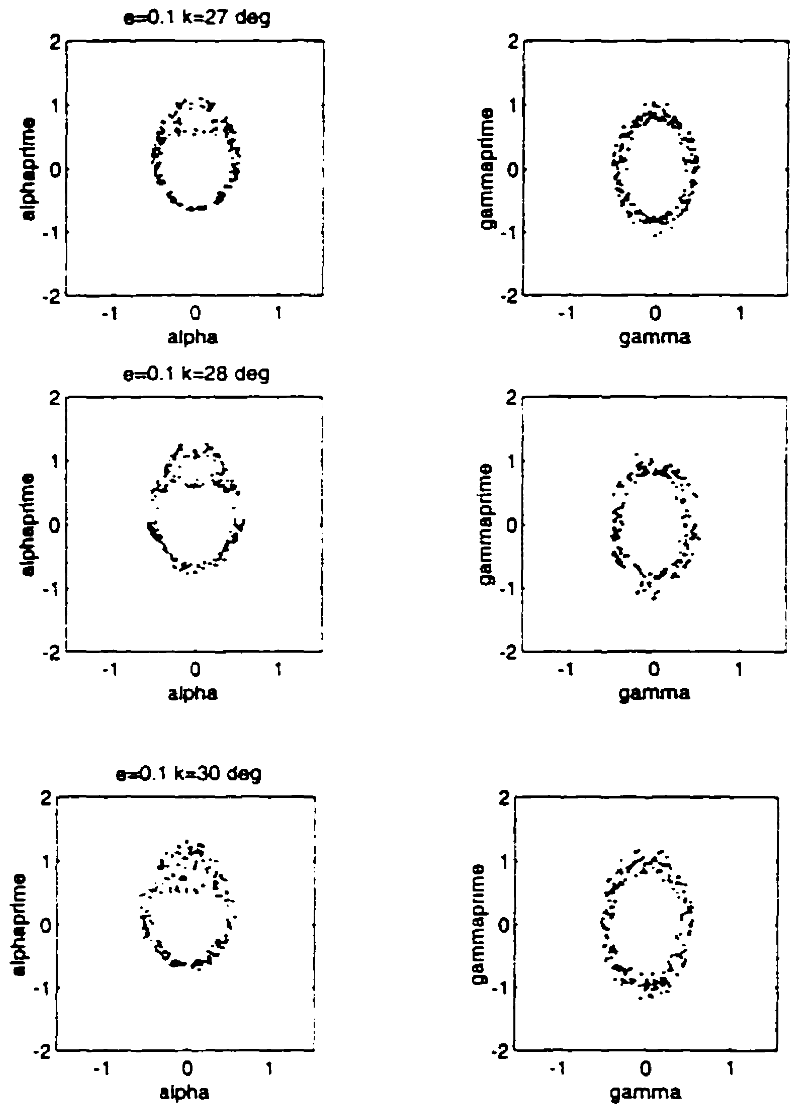

Figure 3.16 (continued)

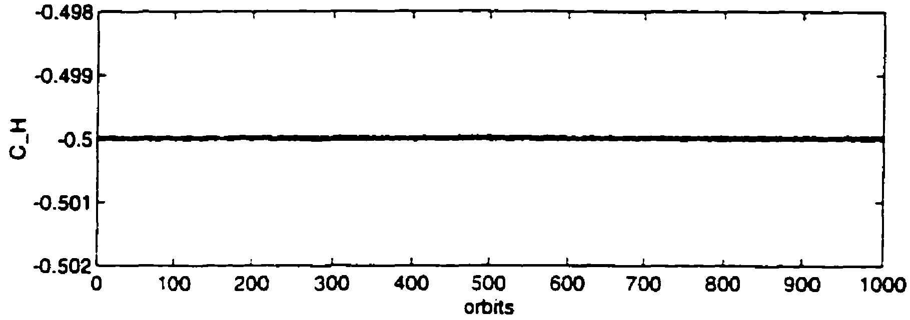

Figure 3.17: Hamiltonian Constant C_H as a Function of Time, for Chaotic Trajectory of Figure 3.5 (d). (Initial Conditions $C_H = -0.5$, $\alpha'(0) = 1.5$, $\alpha(0) = \gamma(0) = 0$)

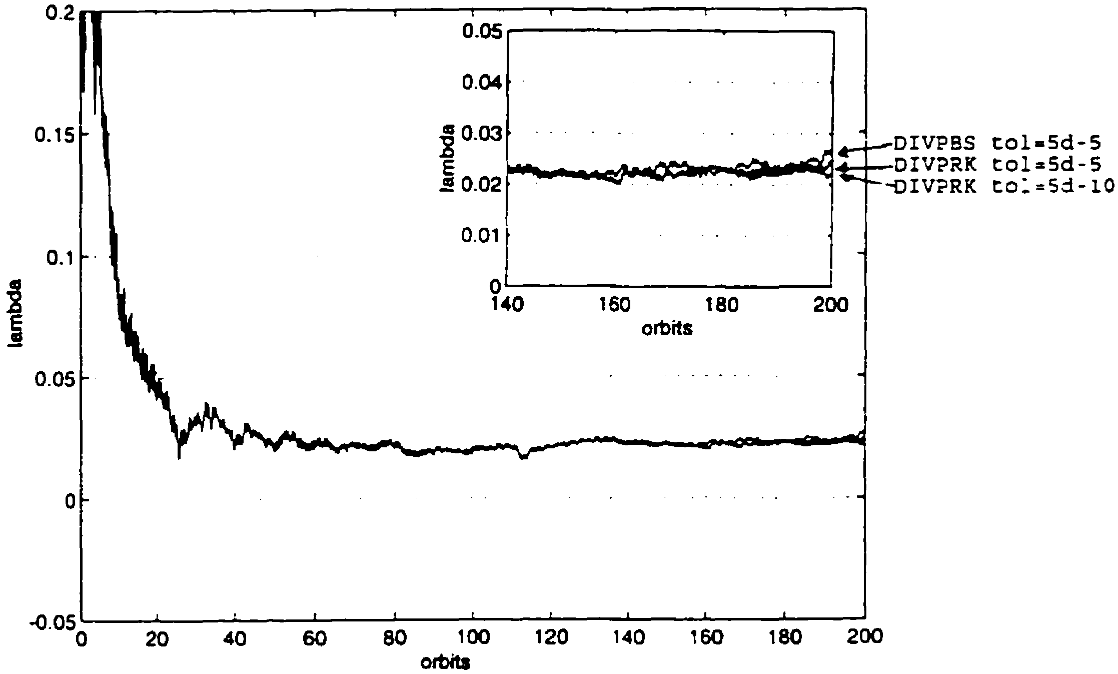

Figure 3.18: Lyapunov Exponents of Motion with Initial Conditions $\alpha(0) = \gamma(0) = 30°$, $\alpha'(0) = \gamma'(0) = 0$, in an Orbit of $e = 0.1$ Plotted Over 200 Orbits, For Numerical Integrators and Specified Tolerances as Shown

Chapter 4

Deployment and Retrieval

4.1 Introduction

While the previous chapter studied the nonlinear dynamics of the stationkeeping phase, where the tether length is constant, this chapter considers the deployment and retrieval phases, where the tether length varies. With the assumption of tether mass negligible compared to m_1 and m_2, the mass ratio $\left[m_1\left(m_2 + \frac{1}{2}\, m_t\right)/m\, m_e\right]$ appearing in the equations of motion Eqs. (2.26)-(2.27) reduces to unity, and the equations of motion reduce to

$$\begin{aligned}
\cos^2\gamma\,\{\alpha'' &- [2(\ell'/\ell) - 2\,\gamma'\tan\gamma - F](\alpha' + 1) \\
&- 3\,G\sin\alpha\,\cos\alpha\} = 0, \qquad (4.1) \\
\gamma'' &- [2(\ell'/\ell) - F]\,\gamma' \\
&- \left[(\alpha' + 1)^2 + 3\,G\cos^2\alpha\right]\sin\gamma\,\cos\gamma = 0. \qquad (4.2)
\end{aligned}$$

with the quantities F and G given by

$$F = 2\epsilon\,\sin\theta/(1 + \epsilon\,\cos\theta), \quad G = 1/(1 + \epsilon\,\cos\theta)\,.$$

Note that deployment (positive ℓ') leads to positive damping terms in Eqs. (4.1)-(4.2) and will tend to stabilize the motion, while the opposite is true for retrieval (negative ℓ').

Different cases governed by the above equations of motion, are considered in this Chapter. Planar motion in a circular orbit is considered first. Pitch stability is examined for varying exponential length rates, and for the unstable cases, compared to an equivalent uniform length rate scheme.

Application of Melnikov's Method to the case of planar motion in a slightly elliptic orbit with slow exponential deployment, to determine the conditions for chaotic motion, is carried out next.

Finally, the coupled motion of retrieval in a circular orbit under a length rate control law is examined. The limit cycle response characteristics are predicted from approximate analytical methods and compared with those obtained from numerical simulation.

4.2 Planar Motion in a Circular Orbit

If the motion is confined to the orbital plane (i.e., $\gamma = 0$) and the orbit is circular (i.e., $\epsilon = 0$), the governing equation, Eq. (4.1), becomes

$$\alpha'' + 2(\ell'/\ell)\,\alpha' + 3\,\sin\alpha\,\cos\alpha = -2(\ell'/\ell)\,. \tag{4.3}$$

As the damping term is proportional to ℓ'/ℓ, deployment causes stabilizing positive damping, retrieval destabilizing negative damping. Equilibrium points ($\alpha'' = \alpha' = 0$) satisfy

$$(3/2)\sin 2\alpha_e + 2(\ell'/\ell) = 0\,. \tag{4.4}$$

From the above equation, it is seen that there exist fixed equilibrium points only in the case where $\ell'/\ell = c =$ constant, that is when the deployment/retrieval is exponential, $\ell = \ell_i \exp(c\,\theta)$. Here ℓ_i is the initial length and $c = \ell'/\ell$ is a dimensionless constant governing the rate of deployment/retrieval. The equation of motion is autonomous. The first term of Eq. (4.4) represents the effect of gravity and centrifugal gradient forces which work to restore the configuration to the local vertical and the second term the effect of Coriolis forces induced by the deployment/retrieval. The resulting equilibrium position of the subsatellite is ahead of the orbiter for downward deployment and behind for upward deployment, and the opposite is true for retrieval. Note that if the length change rate is too large, $\|c\| > 3/4$, equilibrium points do not exist, since $\|\sin 2\alpha_e\|$ must be less than or equal to unity.

The equilibrium angles α_e are given by

$$\alpha_e = (1/2)\sin^{-1}(-4c/3) = (n\pi/2) + (-1)^n\,(1/2)\arcsin(-4c/3),$$

n integer. From linearized analysis about these equilibrium points, one can find that the singular points are saddle points if n is odd and are unstable for both deployment and retrieval; for even n they are foci for $0 < \|c\| < 0.74$, changing to nodes for $0.74 < \|c\| < 0.75$, and stable for deployment $c > 0$, unstable for retrieval $c < 0$. Figure 4.1 plots the fixed points against c, showing stability changes with c. The locus of fixed points undergoes bifurcations at $\|c\| = 3/4$, for $\alpha_e = p\pi + \pi/4$ at $c = -3/4$ and for $\alpha_e = p\pi - \pi/4$ at $c = 3/4$, and at $c = 0$ for $\alpha_e = p\pi$, p integer. At $\|c\| = 3/4$ the saddle points and nodes coalesce into saddle–nodes, with no fixed points existing for $\|c\| > 3/4$; at $c = 0$ centres separate the stable and unstable foci. Local bifurcation theory (see Wiggins (1990) for example) predicts bifurcations at these fixed points, the former case having a single zero eigenvalue with the other eigenvalue having a nonzero real part, while the latter has a pure imaginary pair of eigenvalues.

When $||c|| > 3/4$, there is no fixed point. The length rate is so large that the Coriolis forces overcome the gravity and centrifugal force gradient. While the retrieval dynamics are always unstable, this explains why for deployment too the dynamics become unstable for $||c|| \geq 3/4$, which has been observed in previous work (Baker et al., 1976). Figures 4.2 and 4.3 show the behaviour of phase plane trajectories and corresponding time histories, numerically obtained, for increasing the deployment constant c. Note the movement of the position of the equilibrium with increasing c, the change of focus to node at $c = 0.74$, and finally the change to unstable motion for $c > 3/4$. Figure 4.4 is the phase plane for $c = 3/8$, showing the saddle points, stable foci and separatrices. Figure 4.5 is the phase plane for $c = 1$: the saddles and foci have coalesced and disappeared, and no equilibrium exists. This figure is particularly interesting as it shows how instability occurs in deployment. Pitch grows unbounded in the negative direction along what appears to be the collapsed separatrices remaining from the saddle-node, with bounded pitch rate. Fleurisson et al. (1993) show corresponding phase planes for *retrieval* where the pitch angle and pitch rate grow away from these 'collapsed separatrices' either in the positive or negative directions depending on the initial conditions. Thus not only for $c < 0$ but also for $c > 0.75$, the exponential scheme leads to instability.

If the deployment/retrieval is uniform, $\ell' = \text{constant} = b\ell_{ref}$ and $\ell = \ell_i + b\ell_{ref}\theta$, where b is a dimensionless length rate constant and ℓ_{ref} is a reference tether length, usually taken as either the fully deployed or retrieved final length ℓ_f. Now the equation of motion is non-autonomous and strictly speaking, there is no equilibrium point; however, one can define an instantaneous equilibrium angle $\alpha_e(\theta) = (1/2)\sin^{-1}[(-4b/3)((\ell_i/\ell_{ref}) + b\theta)^{-1}]$. During deployment decaying oscillations occur around a gradually reducing equilibrium angle, while during retrieval growing oscillations occur around an increasing equilibrium angle. Some numerical simulations were carried out to make a comparison between the exponential and uniform schemes for the unstable values of the exponential constant c, such that the initial and final lengths as well as the time to complete the length change are identical in both schemes. Figure 4.6 (a)-(c) presents the phase plane plots and time histories for a series of numerical integrations taken for $c = 0.8$ with ℓ_i/ℓ_f =1/100; 1/1000; and 1/10,000 from a given set of initial conditions. The equivalent uniform case proved to be preferable with the motion bounded, as opposed to the exponential case. Figure 4.7 presents the phase plane plot and time history for $c = -0.1$, retrieval case, with ℓ_i/ℓ_f =10 from a given set of initial conditions; the growth in motion is much slower in the equivalent uniform case.

4.3 Planar Motion in a Slightly Elliptic Orbit with Slow Exponential Deployment - Solution by Melnikov's Method

The equation of motion for planar motion in an elliptic orbit is, from Eqs. (4.1)-(4.2) with $\gamma = \gamma' = 0$,

$$\alpha'' + [2(\ell'/\ell) - F](\alpha' + 1) + 3\,G\, \sin\alpha \, \cos\alpha = 0. \tag{4.5}$$

with

$$F = 2e\, \sin\theta/(1 + e\, \cos\theta), \quad G = 1/(1 + e\, \cos\theta)\,.$$

Consider exponential deployment, i.e., $\ell'/\ell = c > 0$. In an eccentric orbit the system is nonautonomous, hence has three dimensions, and chaos is possible.

Now consider a small eccentricity $e = \mathcal{O}(\epsilon)$. Also assume that the exponential deployment is slow, that is c is small, i.e., $c \equiv \bar{c}\, e$, where $\bar{c} = \mathcal{O}(1)$.

Then Eq. (4.5) becomes, to $\mathcal{O}(\epsilon)$

$$\alpha'' + [2\bar{c}\, e - 2e \sin\theta](\alpha' + 1) + (3/2)(1 - e\cos\theta)\sin 2\alpha = 0\,. \tag{4.6}$$

Rewriting,

$$\alpha'' + 3/2\ \sin 2\alpha = \epsilon[(-2\bar{c} + 2\sin\theta)(\alpha' + 1) + (3/2)\cos\theta \sin 2\alpha]\,. \tag{4.7}$$

This system, a perturbation of an integrable system with a saddle point and separatrix orbit, can be treated by Melnikov's Method, which was introduced and applied to a constant tether length system in Section 3.3.1.3.

The left hand side can be written as that of the normalized pendulum equation by making the substitutions $\phi = 2\alpha$ and $\tau = \sqrt{3}\theta$, and then after some algebra,

$$\frac{d^2\phi}{d\tau^2} + \sin\phi = \epsilon[\cos\omega\tau \sin\phi + a(-\bar{c} + \sin\omega\tau)(\frac{d\phi}{d\tau} + a)]\,. \tag{4.8}$$

where constants $\omega = 1/\sqrt{3}$, and $a = 2/\sqrt{3}$.

Comparing with Eqs. (3.16)-(3.17), one has $t = \tau$, $q \equiv \phi$ and $p \equiv v = d\phi/d\tau$, $g_1 = 0$ and $g_2 = \cos\omega\tau \sin\phi + a(-\bar{c} + \sin\omega\tau)(\frac{d\phi}{d\tau} + a)$.

The undamped, unforced problem ($\epsilon = 0$) is the same as for the system analyzed in Section 3.3.1.3, with Hamiltonian

$$H = (1/2)\, v^2 + (1 - \cos\phi)\,. \tag{4.9}$$

Thus

$$\frac{\partial H}{\partial v} = v, \quad \frac{\partial H}{\partial \phi} = \sin\phi\,. \tag{4.10}$$

and

$$\bar{g} \cdot \overline{\nabla} H = g_2 v. \tag{4.11}$$

As in Section 3.3.1.3, the unperturbed separatrix orbit is given by

$$\phi^* = 2\tan^{-1}(\sinh\tau) \tag{4.12}$$

$$v^* = \frac{d\phi^*}{d\tau} = 2\,\text{sech}\,\tau \tag{4.13}$$

Now

$$\begin{aligned}\sin\phi^* &= 2\frac{\tan(\phi^*/2)}{1+\tan^2(\phi^*/2)} \\ &= 2\tanh\tau\,\text{sech}\,\tau\ . \end{aligned} \tag{4.14}$$

where Eq. (4.12) and trigonometric and hyperbolic identities have been used.

The Melnikov function from Eq. (3.18) thus becomes

$$\begin{aligned} M(\tau_0) &= 4\int_{-\infty}^{+\infty}\cos\omega(\tau+\tau_0)\tanh\tau\,\text{sech}^2\tau d\tau \\ &+ 2a\left[-a\,c\int_{-\infty}^{+\infty}\text{sech}\,\tau d\tau - 2\bar{c}\int_{-\infty}^{+\infty}\text{sech}^2\tau d\tau\right. \\ &\left.-2\int_{-\infty}^{+\infty}\sin\omega(\tau+\tau_0)\,\text{sech}^2\tau d\tau + a\int_{-\infty}^{+\infty}\sin\omega(\tau+\tau_0)\,\text{sech}\,\tau d\tau\right] \end{aligned} \tag{4.15}$$

The integral

$$\int_{-\infty}^{+\infty}\cos\omega\tau\tanh\tau\,\text{sech}^2\tau d\tau = 0 \tag{4.16}$$

since the integrand is odd. The integral

$$\int_{-\infty}^{+\infty}\sin\omega\tau\tanh\tau\,\text{sech}^2\tau d\tau = \frac{\pi}{2}\omega^2\,\text{csch}\,\frac{\pi\omega}{2}\ . \tag{4.17}$$

evaluated by the method of residues. The following integrals can be easily evaluated

$$\int_{-\infty}^{+\infty}\text{sech}\,\tau d\tau = \pi\ . \tag{4.18}$$

$$\int_{-\infty}^{+\infty}\text{sech}^2\tau d\tau = 2\ . \tag{4.19}$$

Then, along with the integrals evaluated in Eqs. (3.27)-(3.30), the Melnikov function of the system is evaluated to be

$$M(\tau_0) = 2\pi\left[(-\omega^2+2\omega a)\,\text{csch}\,\frac{\pi\omega}{2} + a^2\,\text{sech}\,\frac{\pi\omega}{2}\right]\sin\omega\tau_0 - 2\bar{c}\,a[a\pi+4] \tag{4.20}$$

Transverse intersection and chaotic separatrix motion occurs if $M(\tau_0)$ changes sign at some τ_0; this occurs if $\bar{c} < \bar{c}_{cr}$, where $\bar{c}_{cr}$ is the critical value of $\bar{c}$

$$\bar{c}_{cr} = \frac{\pi}{a(a\pi + 4)} \left[(-\omega^2 + 2\omega a) \operatorname{csch} \frac{\pi\omega}{2} + a^2 \operatorname{sech} \frac{\pi\omega}{2} \right] . \tag{4.21}$$

Inserting the values of a and ω, one obtains

$$\bar{c}_{cr} = \frac{3\pi}{4(\pi + 2\sqrt{3})} \left[\operatorname{csch} \frac{\sqrt{3}\pi}{6} + \frac{4}{3} \operatorname{sech} \frac{\sqrt{3}\pi}{6} \right] . \tag{4.22}$$

Therefore chaos occurs if $c < c_{cr}$ where

$$c_{cr} = \frac{3\pi}{4(\pi + 2\sqrt{3})} \left[\operatorname{csch} \frac{\sqrt{3}\pi}{6} + \frac{4}{3} \operatorname{sech} \frac{\sqrt{3}\pi}{6} \right] \epsilon . \tag{4.23}$$

or alternatively, chaos occurs if $\epsilon > \epsilon_{cr}$ where

$$\epsilon_{cr} = \frac{4(\pi + 2\sqrt{3})c}{3\pi \left(\operatorname{csch} \frac{\sqrt{3}\pi}{6} + \frac{4}{3} \operatorname{sech} \frac{\sqrt{3}\pi}{6} \right)} . \tag{4.24}$$

The above result holds for small eccentricity and exponential deployment constant. The last equation reduces for $c = 0$ to the familiar criterion for chaos in the (planar motion) stationkeeping case, $\epsilon > 0$: the Melnikov analysis of Tong and Rimrott (1991a) applicable to the stationkeeping case, is a special case of the analysis here. Exponential deployment c introduces dissipation into the system, such that chaotic motion only appears for sufficiently large eccentricity ϵ.

4.4 Coupled Motion of Retrieval Under a Length Rate Control Law, in a Circular Orbit

If both out of plane as well as in plane motions are considered, the equations of motion in the variable length case can be obtained from Eqs. (2.26) and (2.27) for a circular orbit and for negligible tether mass, as follows:

$$\alpha'' + (\alpha' + 1)[-2\gamma' \tan\gamma + 2(\ell'/\ell)] + 3 \sin\alpha \cos\alpha = 0 . \tag{4.25}$$

$$\gamma'' + 2(\ell'/\ell)\gamma' + \left[(1+\alpha')^2 + 3\cos^2\alpha\right]\sin\gamma\cos\gamma = 0 \,. \tag{4.26}$$

This system of equations has equilibrium points $\alpha_e = (1/2)\sin^{-1}[(-4/3)(\ell'/\ell)]$, $\gamma_e = n\pi/2$. From the roll equation, it may be noted that the roll motion is negatively damped and unstable during retrieval. The same can be seen from the pitch equation for small roll motion. This is illustrated by the phase planes and time histories of Figure 4.8.

Pitch and roll motions can be confined to limit cycles by using a length change control law involving linear feedback of pitch rate and quadratic feedback of roll rate (Monshi (1992), Monshi et al. (1991)):

$$\ell' = c[1 - K_\alpha\alpha' - K_\gamma\gamma'^2]\ell, \; c < 0 \tag{4.27}$$

The system of equations remains autonomous.

In the following, the characteristics of the pitch and roll limit cycle response (respective position, amplitude, frequency and the phase difference) are determined using approximate analytical methods. For specific sets of system parameters, predicted values are compared with the values of the actual response as obtained from numerical integration of the equations of motion. In the previous work (Monshi, 1992, Monshi et al., 1991), approximate analytical methods were applied to pure in-plane and out-of-plane motions only, and study of the coupled limit cycle motion was mainly limited to numerical simulation.

For small motions (α, γ and their derivatives of $\mathcal{O}(\epsilon)$), the system of equations Eqs. (4.25)-(4.26), with length change control law Eq. (4.27), can be written to $\mathcal{O}(\epsilon^3)$ as:

$$\alpha'' + \alpha'[-2c(K,-1+K_\alpha\alpha'+K_\gamma\gamma'^2)-2\gamma'\gamma] + \alpha[3-2\alpha^2] = 2cK_\gamma\gamma'^2+2\gamma'\gamma-2c, \tag{4.28}$$

$$\gamma'' - \gamma' 2c[-1 + K_\alpha\alpha' + K_\gamma\gamma'^2] + \gamma[4 - \frac{8}{3}\gamma^2 + 2\alpha' + \alpha'^2 - 3\alpha^2] = 0 \,. \tag{4.29}$$

Note that the linearized equations.

$$\alpha'' - 2c(K_\alpha - 1)\alpha' + 3\alpha = -2c\,. \tag{4.30}$$

$$\gamma'' + 2c\gamma' + 4\gamma = 0\,.\ c < 0 \tag{4.31}$$

predict that pitch executes damped (if $K_\alpha > 1$) oscillations approaching $\alpha_e = -2c/3$, and roll executes negatively damped (unstable) oscillations about $\gamma_e = 0$. The limit cycles occur when nonlinearities are considered.

An approximation of the roll limit cycle motion can be made by considering a pure roll motion. linear in roll except for the control term.

$$\gamma'' - \gamma' 2c[-1 + K_\gamma \gamma'^2] + 4\gamma = 0\,. \tag{4.32}$$

or

$$\gamma'' + 4\gamma = -c[2(\gamma' - K_\gamma \gamma'^3)]\,. \tag{4.33}$$

and assuming small c. For small c the method of variation of parameters can be applied to the above equation. This was carried out by Monshi (1992): according to this method. a limit cycle oscillation of the following form occurs:

$$\gamma = b\cos(\omega\tau)\,. \tag{4.34}$$

where frequency ω and amplitude b are

$$\omega = 2. \tag{4.35}$$

$$b = [1/(3K_\gamma)]^{1/2}\,. \tag{4.36}$$

An approximation of the pitch limit cycle motion can be made by considering the pitch equation. linearized in terms of pitch but retaining the $\mathcal{O}(\epsilon^2)$ roll forcing terms.

$$\alpha'' - 2c(K_\alpha - 1)\alpha' + 3\alpha = -2cK_\gamma \gamma'^2 + 2\gamma'\gamma - 2c\,. \tag{4.37}$$

and assuming a roll limit cycle motion $\gamma = b\cos\omega\tau$. Substituting $\gamma = b\cos\omega\tau$ and its derivative into the right hand side of Eq. (4.37) and expanding using trigonometric identities, Eq. (4.37) becomes

$$\alpha'' - 2c(K_\alpha - 1)\alpha' - 3\alpha = -2c(1 - K_\gamma b^2\omega^2/2) - cK_\gamma b^2\omega^2\cos 2\omega\tau - \omega b^2 \sin 2\omega\tau. \quad (4.38)$$

or, rewriting the forcing terms,

$$\alpha'' - 2c(K_\alpha - 1)\alpha' - 3\alpha = -2c(1 - K_\gamma b^2\omega^2/2) + b^2\omega\sqrt{c^2K_\gamma^2\omega^2 + 1}\cos(2\omega\tau + \beta), \quad (4.39)$$

where

$$\beta = \tan^{-1}\left(\frac{-1}{cK_\gamma\omega}\right). \quad (4.40)$$

This linear, damped ($K_\alpha > 1$), harmonically forced equation has the steady state solution

$$\alpha = \frac{-2c}{3}(1 - K_\gamma b^2\omega^2/2) + b^2\omega\sqrt{\frac{c^2K_\gamma^2\omega^2 + 1}{(3 - 4\omega^2)^2 + 16\omega^2c^2(K_\alpha - 1)^2}}\cos[2\omega\tau + (\beta - \psi)], \quad (4.41)$$

where

$$\psi = \tan^{-1}\left(\frac{-4c\omega(K_\alpha - 1)}{3 - 4\omega^2}\right). \quad (4.42)$$

Thus for roll motion executing a limit cycle motion $\gamma = b\cos\omega\tau$, the approximate pitch equation of motion predicts a steady state limit cycle motion of the form $\alpha = \alpha_0 + a\cos(2\omega\tau + \Phi)$ ($K_\alpha > 1$), where α_0, a and Φ are known explicitly. If the phase angle between the two motions is transferred to the roll expression, one obtains

$$\gamma = b\cos(\omega\tau + \phi), \quad \alpha = \alpha_0 + a\cos 2\omega\tau. \quad (4.43)$$

with $\phi = -\Phi/2$. Then

$$\alpha_0 = \frac{-2c}{3}(1 - K_\gamma b^2\omega^2/2) \quad (4.44)$$

$$a = b^2\omega\sqrt{\frac{c^2K_\gamma^2\omega^2 + 1}{(3 - 4\omega^2)^2 + 16\omega^2c^2(K_\alpha - 1)^2}} \quad (4.45)$$

$$\phi = (\psi - \beta)/2 = \frac{1}{2}\left[\tan^{-1}\left(\frac{-4c\omega(K_2 - 1)}{3 - 4\omega^2}\right) - \tan^{-1}\left(\frac{-1}{cK_\gamma\omega}\right)\right] \tag{4.46}$$

Note that α_0 is the average value of the pitch oscillations, and expression Eq. (4.44) will also result if Eq. (4.37) is averaged over a period of pitch, assuming the respective harmonic expressions for pitch and roll found above. The roll motion leads to an average value of pitch α_0 less than $\alpha_e = -2c/3$.

Now, by assuming periodic solutions of the form Eq. (4.43)

$$\gamma = b\cos(\omega\tau - \phi), \quad \alpha = \alpha_0 + a\cos 2\omega\tau \ .$$

as suggested by the above analyses, and substituting into the $\mathcal{O}(\epsilon^3)$ equations of motion Eq. (4.28)-(4.29), the method of harmonic balance is used to obtain more accurate expressions determining ω, b, α_0, a, and ϕ. Details of the method of harmonic balance, which is closely related to the Galerkin method, can be found in any reference on approximate analytical methods of nonlinear analysis; Nayfeh and Mook (1979) is an example.

Proceeding, the pitch and roll approximations Eqs. (4.43) and their derivatives are substituted into Eqs. (4.28)-(4.29), which are then expanded by use of the appropriate trigonometric identities in terms of sine and cosine harmonics of $\omega\tau$. The pitch equation is composed of constant terms and even harmonics; the roll equation is composed of odd harmonics. The constant terms and second harmonics of the pitch equation, and the first harmonics of the roll equation are collected. Based on the assumption of pitch and roll, Eq. (4.43), the method of harmonic balance requires that the constant term and coefficients of those harmonics be equated to zero (to balance the zero values on the right hand sides of the equations). A higher accuracy solution would have been found if higher harmonics had been included in the assumption, in which case the coefficients of these harmonics are also equated to zero.

In this way, the following five equations in the five unknowns ω, b, α_0, a, and ϕ, are obtained:

Constant (from pitch equation):

$$2c + 3\alpha_0 - 2\alpha_0^3 - 3\alpha_0 a^2 - 4c\omega^2 a^2 K_\alpha - cK_\gamma \omega^2 b^2 \\ + c\omega^3 ab^2 K_\gamma \sin 2\phi - \omega^2 ab^2 \cos 2\phi = 0 \qquad (4.47)$$

$\cos 2\omega\tau$ (from pitch equation):

$$-4\omega^2 a - 6\alpha_0^2 a + 3a - \frac{3}{2}a^3 + cK_\gamma \omega^2 b^2 \cos 2\phi + \omega b^2 \sin 2\phi = 0 \qquad (4.48)$$

$\sin 2\omega\tau$ (from pitch equation):

$$4c\omega a(K_\gamma - 1) + 2c\omega^2 ab^2 K_\gamma - cK_\gamma \omega b^2 \sin 2\phi + b^2 \cos 2\phi = 0 \qquad (4.49)$$

$\cos \omega\tau$ (from roll equation):

$$\cos\phi(-\omega^2 - 2cK_\gamma \omega^2 a + 4 - 2b^2 - 3\alpha_0^2 - 3\alpha_0 a + 2\omega^2 a^2 - \frac{3}{2}a^2) \\ + \sin\phi(-2c\omega + \frac{3}{2}cK_\gamma \omega^3 b^2 + 2\omega a) = 0 \qquad (4.50)$$

$\sin \omega\tau$ (from roll equation):

$$\sin\phi(-\omega^2 + 2cK_\alpha \omega^2 a + 4 - 2b^2 - 3\alpha_0^2 + 3\alpha_0 a + 2\omega^2 a^2 - \frac{3}{2}a^2) \\ + \cos\phi(2c\omega - \frac{3}{2}cK_\gamma \omega^3 b^2 + 2\omega a) = 0 \, . \qquad (4.51)$$

This is a system of nonlinear algebraic equations which will have multiple solutions. It is third order in α_0, a, and b; ω appears up to the third power. An analytical solution, which would best be attempted with the aid of computer algebra, was not attempted.

Consideration up to the second order in α_0, a, and b would simplify the first three equations, and correspond to having considered the pitch equation only to $\mathcal{O}(\epsilon^2)$.

The first equation (i.e., Eq. (4.47), from the constant terms of the pitch equation) would then immediately yield a solution for α_0 explicitly, as a function of a, b and ω:

$$\alpha_0 = \frac{-2c}{3}(1 - K_\gamma b^2\omega^2/2 - 2K_\alpha a^2\omega^2) \,. \tag{4.52}$$

This expression for α_0, the average value of pitch, also results by averaging the $\mathcal{O}(\epsilon^2)$ equation over a period of pitch, assuming the respective harmonic expressions for pitch and roll, as shown by Monshi (1992). It shows that α_0 is reduced from $\alpha_e = -2c/3$ by the presence of steady-state oscillations of both pitch and roll: this is a more accurate approximation of α_0 than obtained previously, Eq. (4.44), where no $\mathcal{O}(\epsilon^2)$ pitch terms were considered.

Eq. (4.52) from the first equation (from pitch) would reduce the second order system of equations to four unknowns ω, b, a, and ϕ. Further analytical solution remains complex and was not carried out in this work.

The nonlinear system of five equations Eqs. (4.47)-(4.51) in the five unknowns ω, b, α_0, a, and ϕ, second or third (as they are shown) order in α_0, a and b can be solved numerically, given a particular set of system parameters c, K_α, K_γ, where an estimate of the desired solution is provided. Such numerical solutions were obtained here using the 'fsolve' M-file function of MATLAB and are given presently.

Note that Eqs. (4.35)-(4.36), (4.44)-(4.46), from the approximate solutions presented earlier, or, preferably, Eqs. (4.35)-(4.36), (4.45)-(4.46), along with Eq. (4.52), together provide an explicit 'first approximation' or estimate of the five unknowns for a given set of parameters.

Figure 4.9 and Figure 4.10 show the pitch and roll phase planes and time histories from numerical integration of the equations of motion for $c = -0.3$, $K_\alpha = 2$, and $K_\gamma = 9$, and for $c = -0.5$, $K_\alpha = 1$, and $K_\gamma = 27$ respectively. First considering the former, initially when angles are small, motion follows the linearized equations of motion, that is, pitch motion exhibits damped oscillations toward $\alpha_e = -2c/3 = 11.5°$ and roll negatively damped oscillations about $\gamma_e = 0$. When the roll motion reaches its limit cycle, it excites the pitch limit cycle as well. Considering the second case, where $K_\alpha = 1$, the initial pitch oscillations about $\alpha_e = 19°$ show little damping. Damping is provided by higher order terms in the pitch equation of motion and ensures that when the roll motion reaches its limit cycle, pitch assumes the steady state limit cycle also. The roll and pitch oscillations can be formulated as Eq. (4.43) of the approximate solutions

$$\gamma = b\cos(\omega\tau + \phi), \quad \alpha = \alpha_0 + a\cos 2\omega\tau .$$

Tables 4.1 and 4.2 compare, for the cases $c = -0.3$, $K_\alpha = 2$, $K_\gamma = 9$ and $c = -0.5$, $K_\alpha = 1$, $K_\gamma = 27$ respectively, the actual values of ω, b, α_0, a and ϕ as obtained from numerical simulation, with three approximations. The 'first approximation' refers to the explicit expressions Eqs. (4.35)-(4.36), (4.45)-(4.46), along with Eq. (4.52). These were derived using a combination of methods applied to lower order approximations of the equations of motion. The nonlinear system of equations Eqs. (4.47)-(4.51) for the two cases second and third order in α_0, a and b respectively was solved numerically, using the first approximation values as estimates. The system of equations was derived using the method of harmonic balance applied to higher order approximations of the equations of motion. These predicted the values more accurately as might be expected, although sometimes the second order solution seemed to be closer to the numerical integration results, as compared to the third order solution (perhaps error was introduced when extracting the values of the numerical integration solutions). However, the values obtained from the explicit expressions, which did not require numerical solution, are indeed an excellent first approximation, at least for these cases where motions are sufficiently small.

	First Approximation Eqs. (4.35)-(4.36), (4.45)-(4.46), (4.52)	Numerical Solution of Eqs. (4.47)-(4.51) to 2nd order	3rd order	Numerical Integration of Equations of Motion
ω	2.00	1.95	1.96	1.95
b	11.0 °	12.2 °	12.2 °	12.5 °
a	1.8 °	2.2 °	2.1 °	2.1 °
α_0	3.6 °	2.2 °	2.5 °	2.3 °
σ	80 °	79 °	75 °	75 °

Table 4.1: Comparison for case $c = -0.3$, $K_\alpha = 2$, $K_\gamma = 9$

	First Approximation Eqs. (4.35)-(4.36), (4.45)-(4.46), (4.52)	Numerical Solution of Eqs. (4.47)-(4.51) to 2nd order	3rd order	Numerical Integration of Equations of Motion
ω	2.00	1.94	1.96	1.93
b	6.4 °	7.0 °	6.7 °	7.3 °
a	2.9 °	3.6 °	3.4 °	3.4 °
α_0	6.0 °	4.2 °	4.4 °	3.8 °
σ	89 °	89 °	82 °	76 °

Table 4.2: Comparison for case $c = -0.5$, $K_\alpha = 1$, $K_\gamma = 27$

Monshi (1992) and Monshi et al. (1991) introduced a second reel rate law involving absolute value, rather than quadratic, out-of-plane feedback. Future work could similarly apply approximate analytical methods to predict the limit cycle response characteristics using this control law.

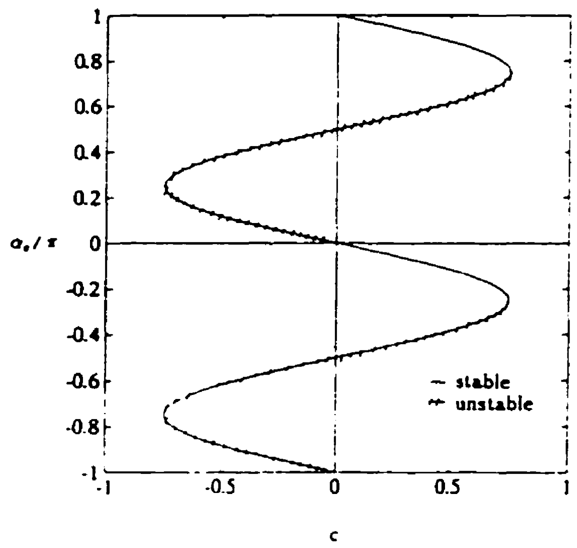

Figure 4.1: Bifurcation Diagram of Fixed Points for Planar Exponential Deployment/Retrieval in a Circular Orbit

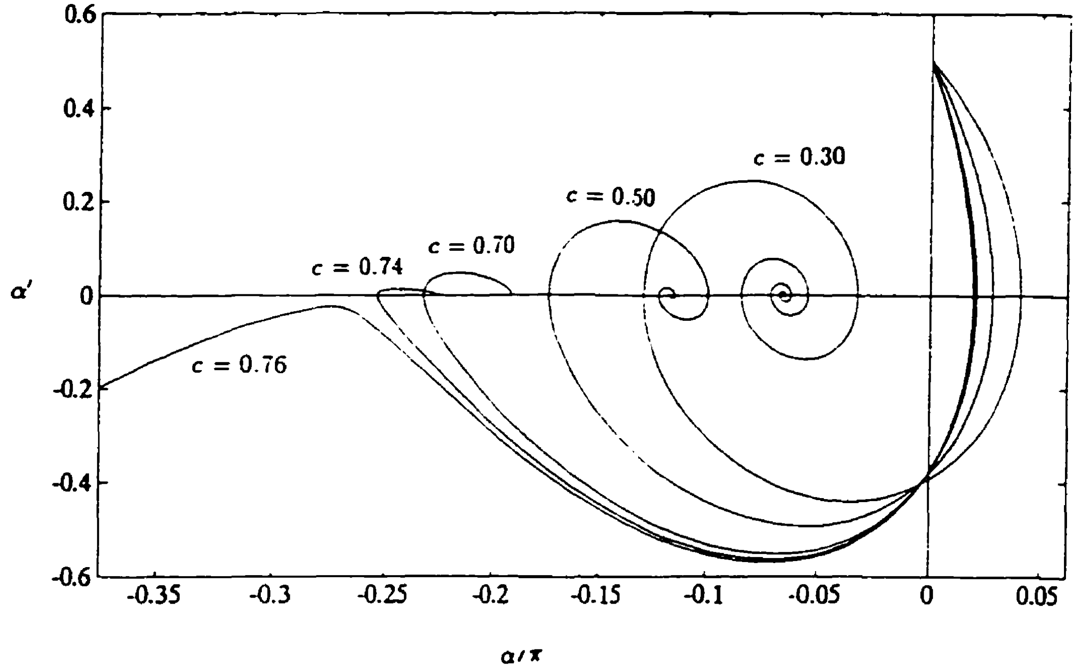

Figure 4.2: Phase Plane Trajectories for Increasing Deployment Constant c, Planar Motion in a Circular Orbit. Showing Change in Position and Type of Equilibrium Point and Change to Instability

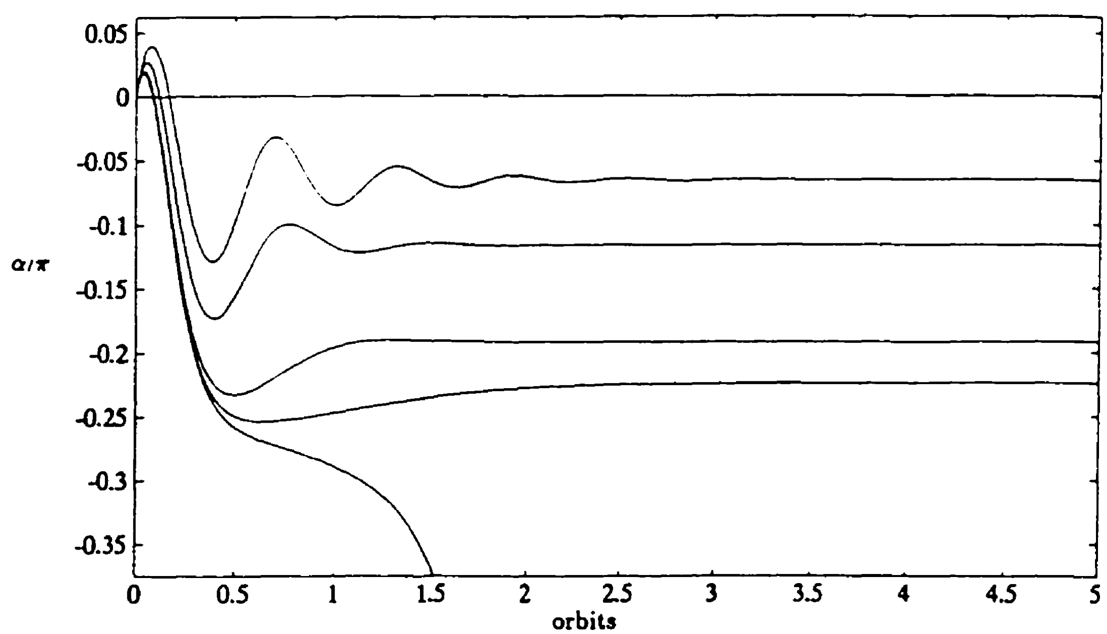

Figure 4.3: Corresponding Time Histories

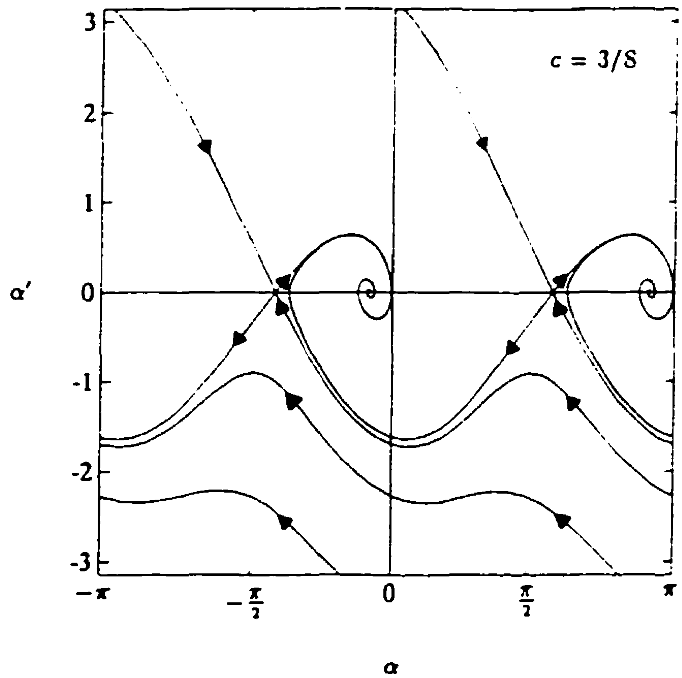

Figure 4.4: Phase Plane for Deployment Constant $c = 3/8$, Planar Motion in a Circular Orbit, Showing the Stable Foci, Saddle Points and Separatrices

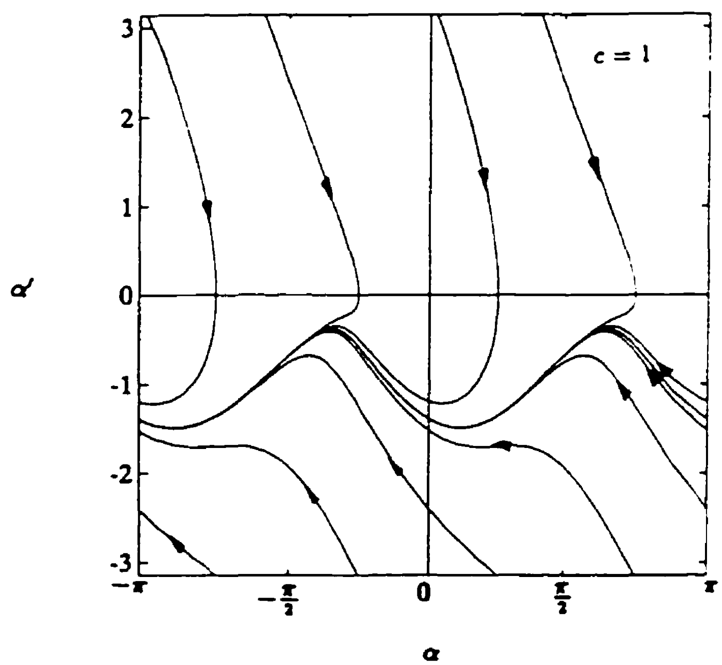

Figure 4.5: Phase Plane for Deployment Constant $c = 1$, Planar Motion in a Circular Orbit, Showing the Disappearance of Equilibrium Points and Occurrence of Instability

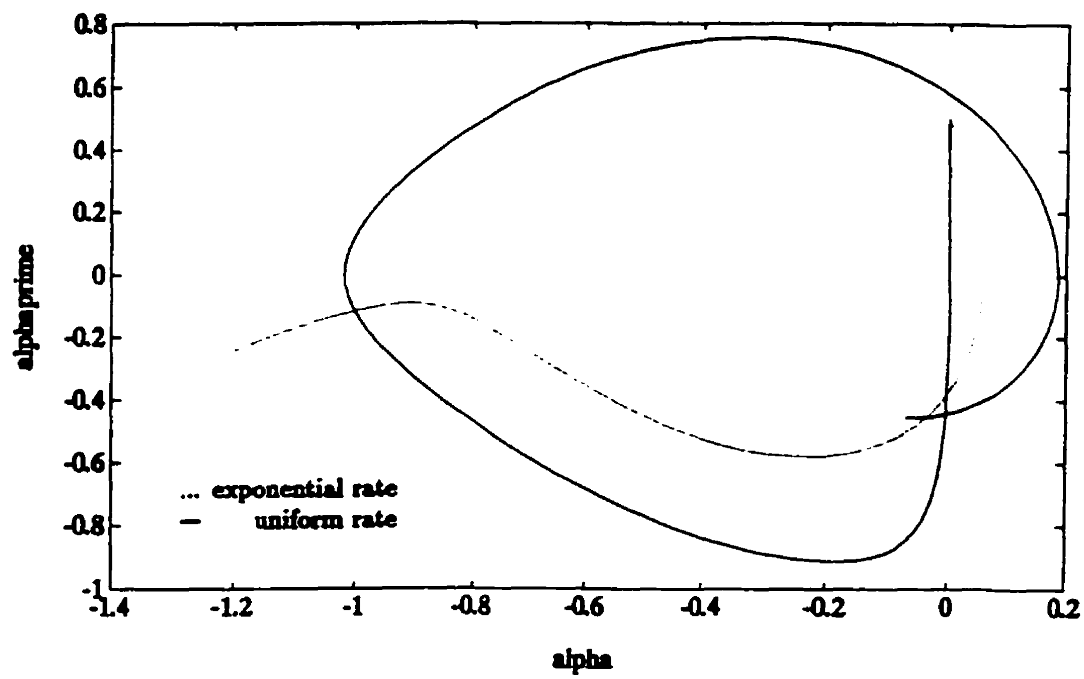

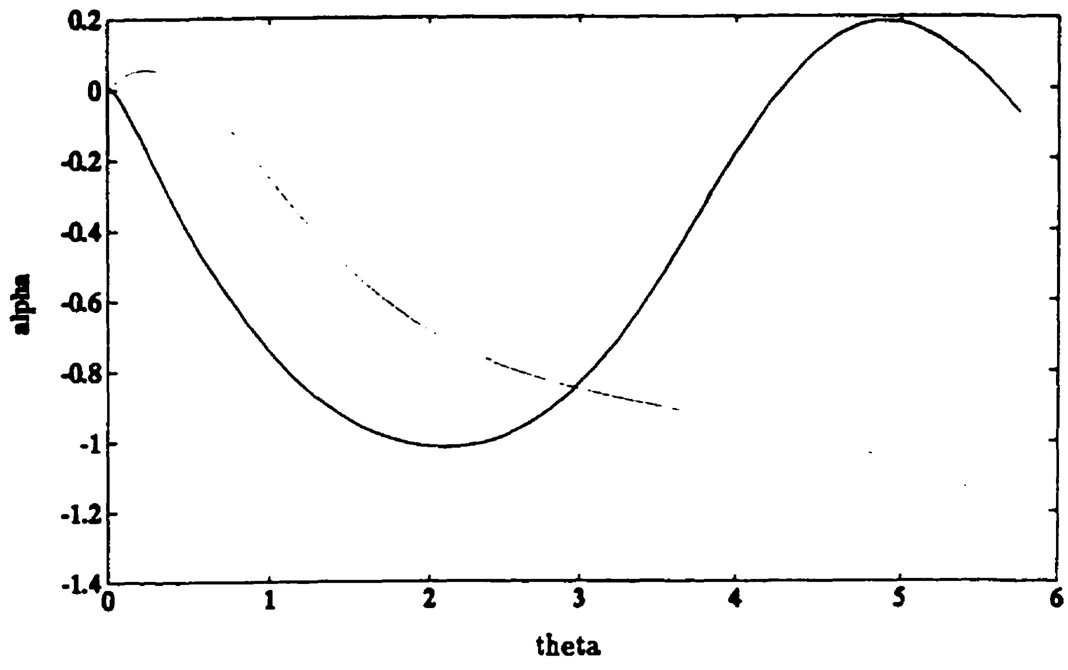

Figure 4.6: Phase Planes and Time Histories for Comparison of Exponential and Uniform Fast Deployment, Planar Motion in a Circular Orbit, $c = 0.8$, $\alpha(0) = 0$, $\alpha'(0) = 0.5$; (a) $\ell_i/\ell_f = 1/100$.

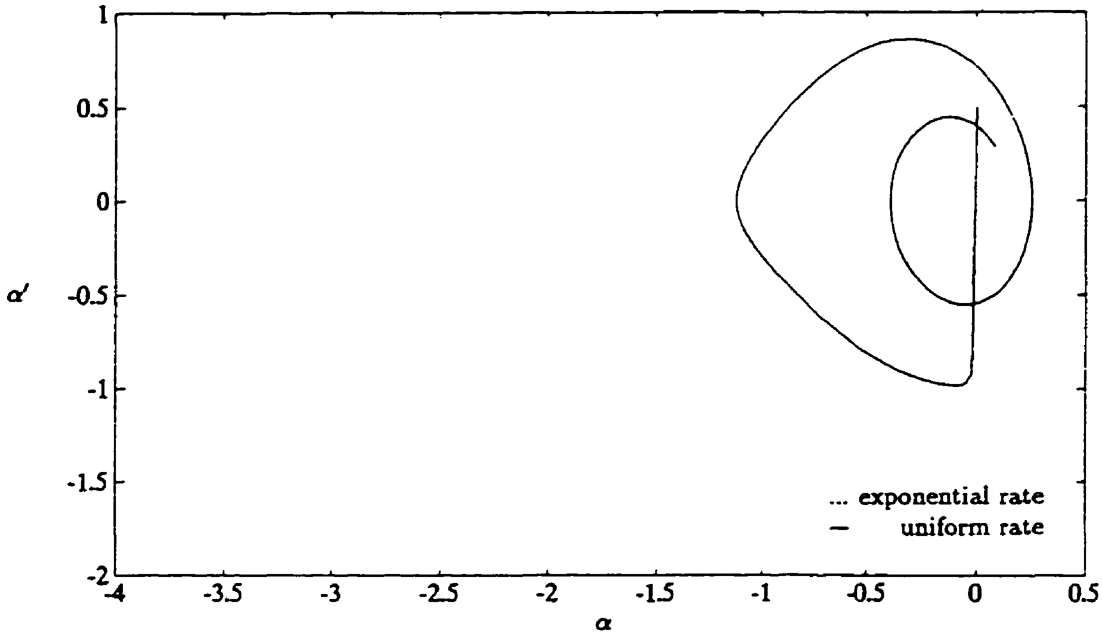

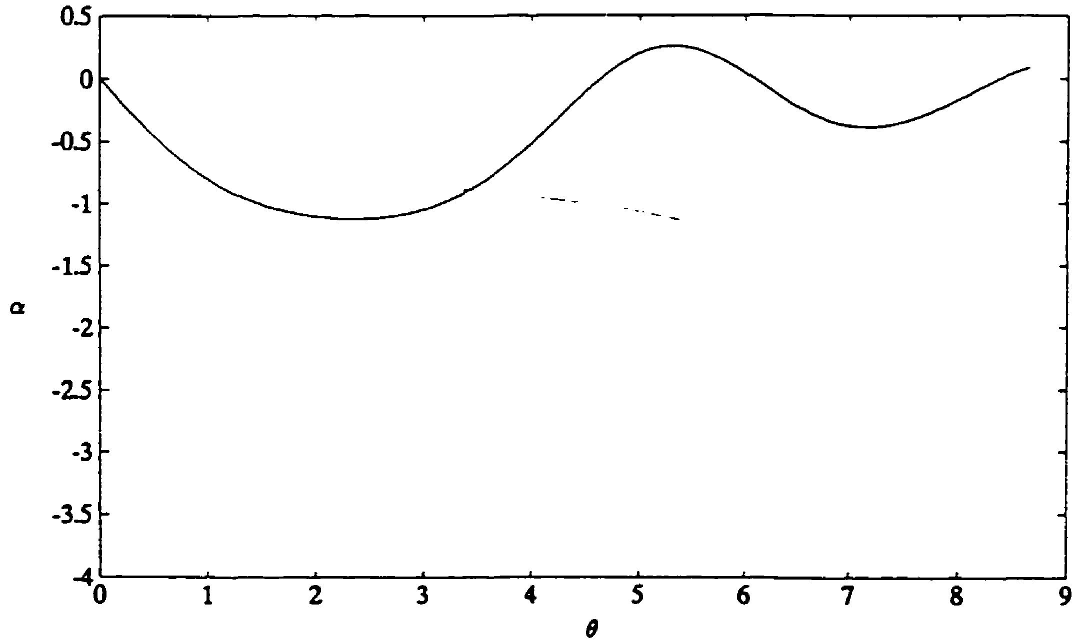

Figure 4.6 (continued) (b) $\ell_i/\ell_f = 1/1000$.

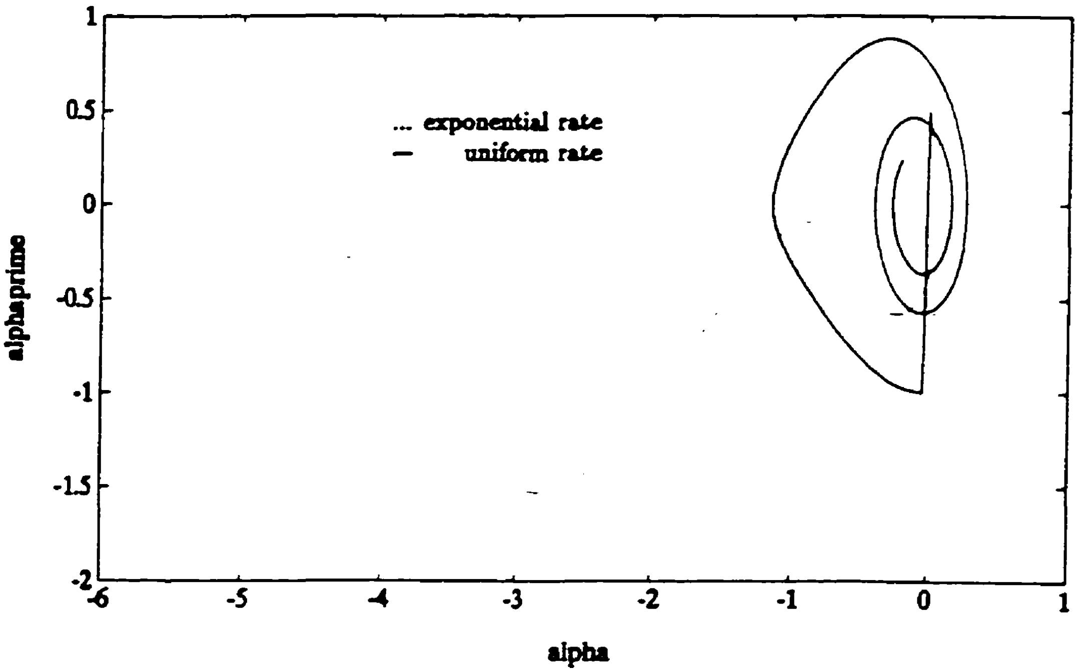

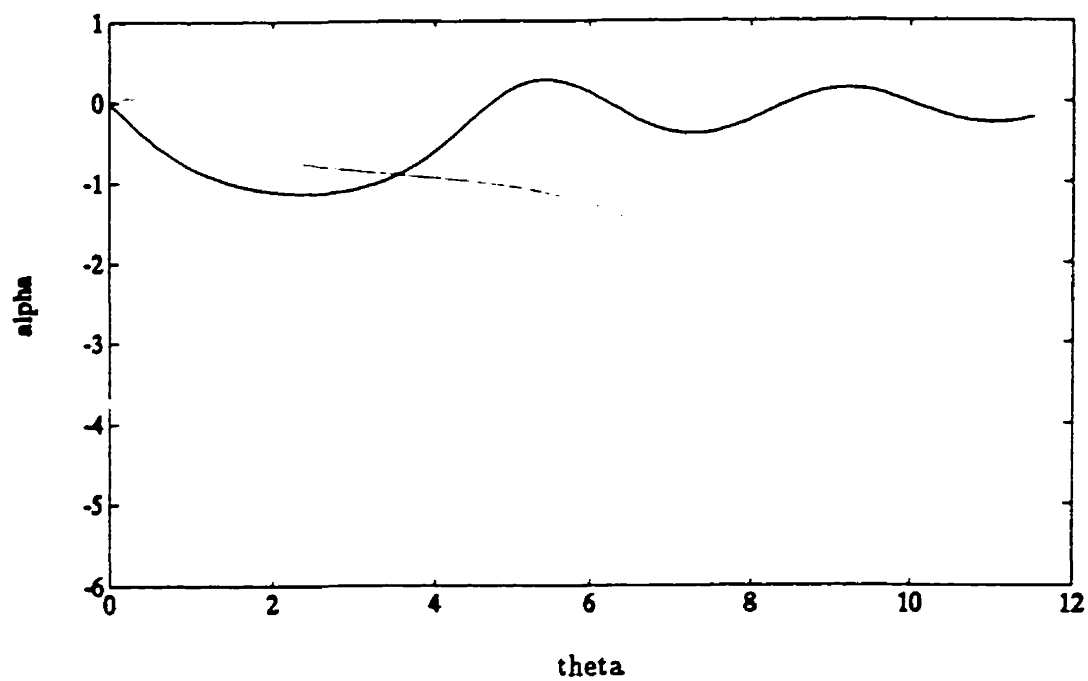

Figure 4.6 (continued) (c) $\ell_i/\ell_f = 1/10,000$.

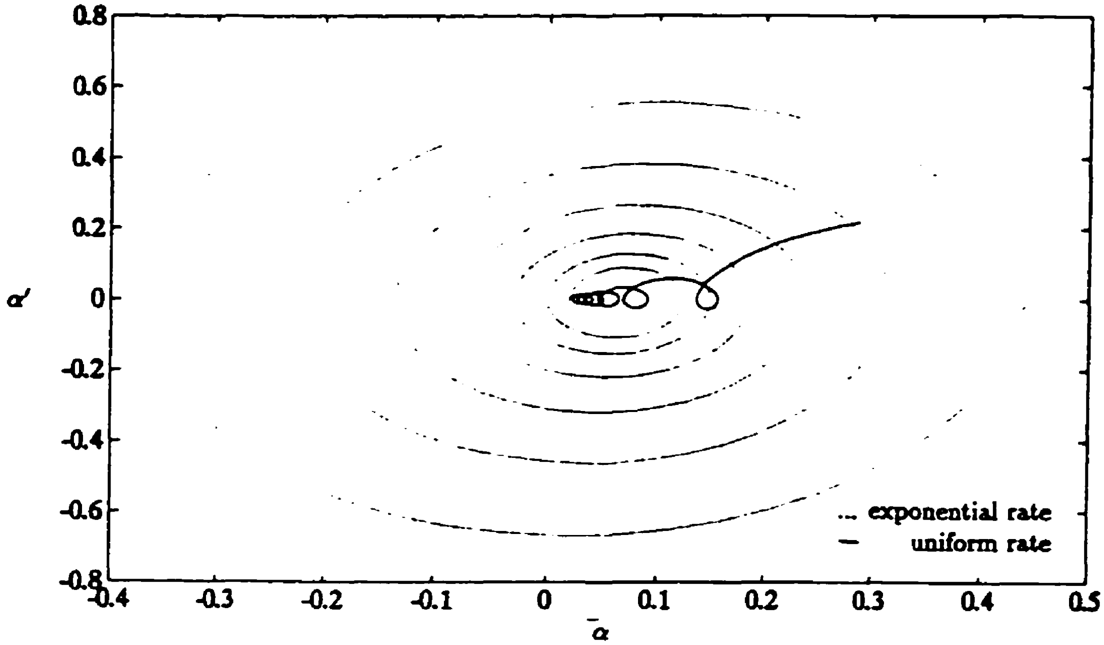

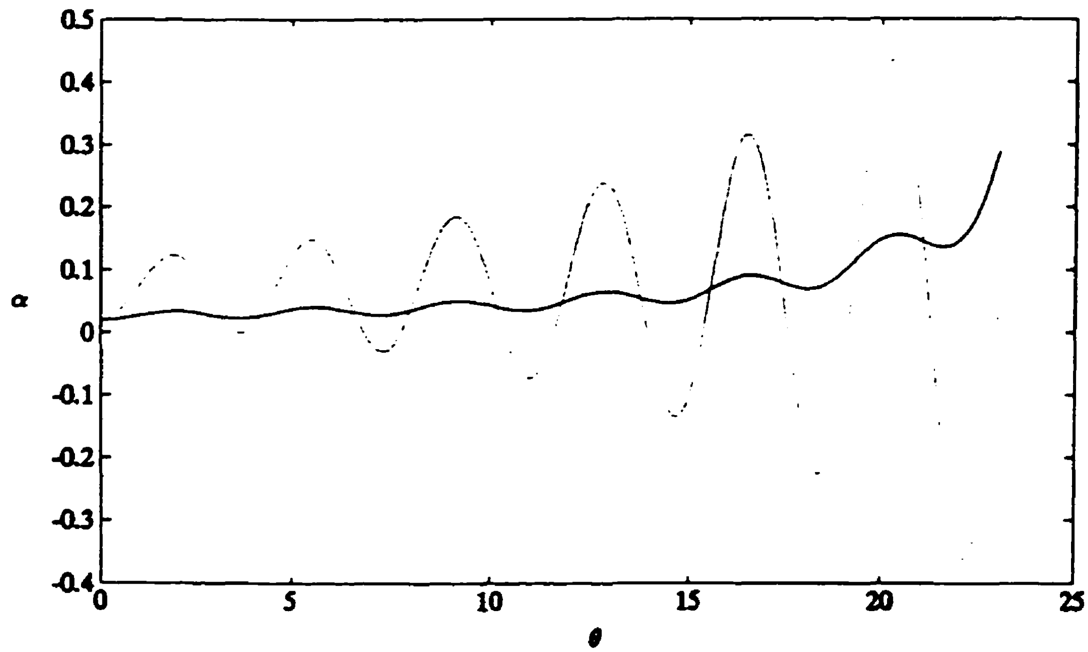

Figure 4.7: Phase Plane and Time History for Comparison of Exponential and Uniform Retrieval, Planar Motion in a Circular Orbit, $c = -0.1$, $\ell_i/\ell_f = 10$, $\alpha(0) = 0.02$ rad, $\alpha'(0) = 0$

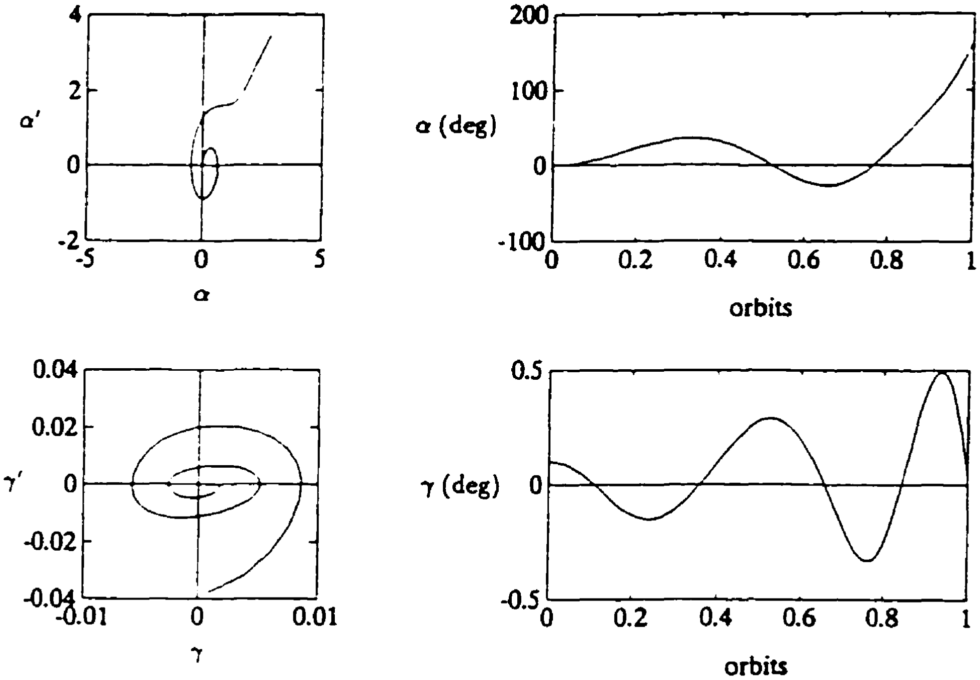

Figure 4.8: Phase Plane and Time Histories for Uncontrolled Retrieval in a Circular Orbit. $\ell'/\ell = c = -0.3$; $\ell_i = 100$ km, $\ell_f = 15$ km; $\alpha(0) = \alpha'(0) = 0$, $\gamma(0) = 0.1$ deg, $\gamma'(0) = 0$

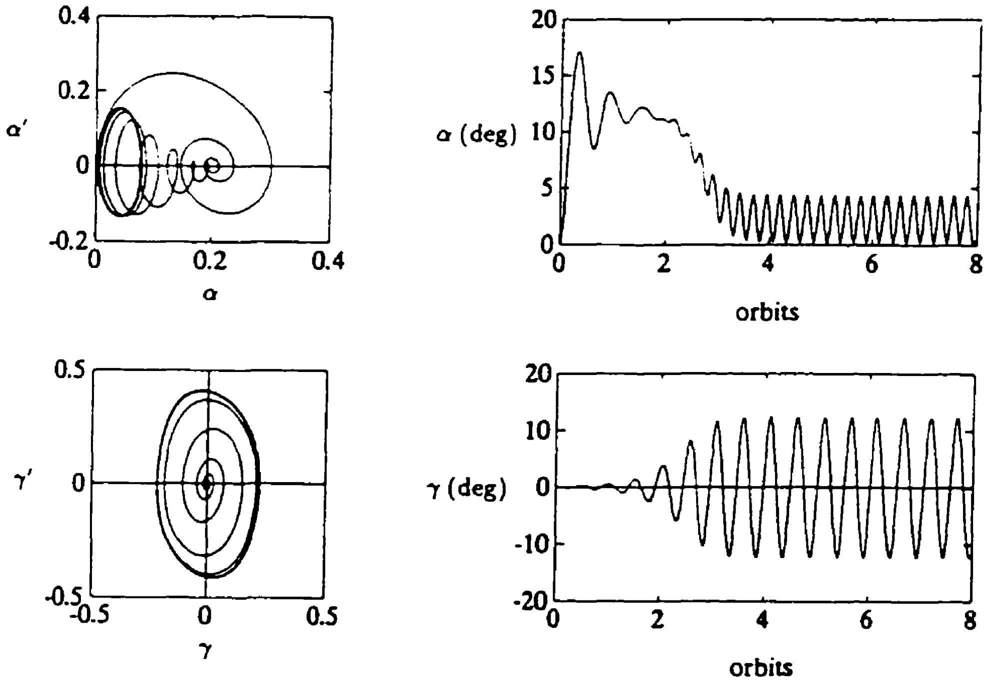

Figure 4.9: Phase Plane and Time Histories for Controlled Retrieval Eq. (4.27) in a Circular Orbit. $K_\alpha = 2$, $K_\gamma = 9$; $c = -0.3$; $\ell_i = 100$ km, $\ell_f = 0.1$ km; $\alpha(0) = \alpha'(0) = 0$, $\gamma(0) = 0.1$ deg, $\gamma'(0) = 0$

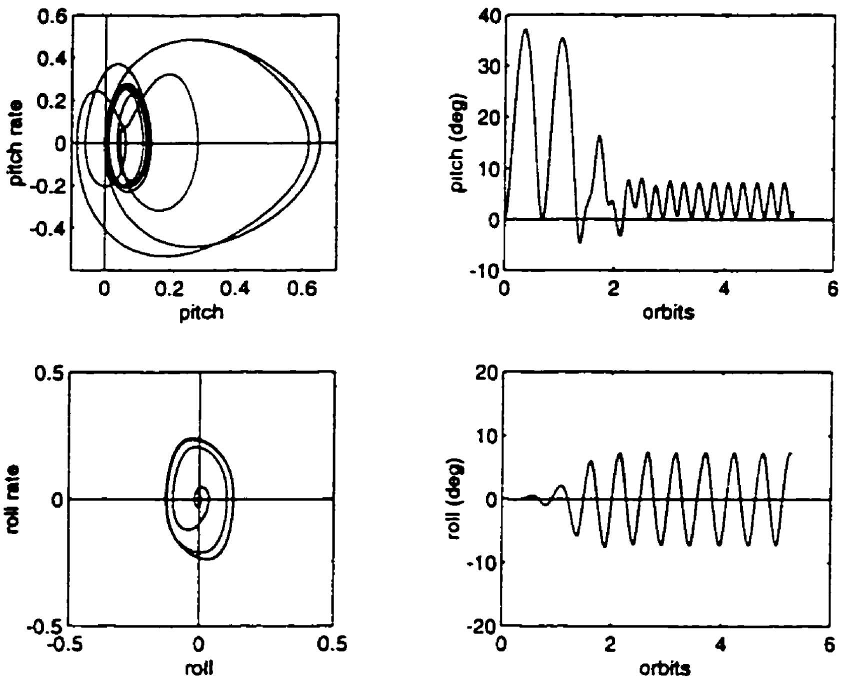

Figure 4.10: Phase Plane and Time Histories for Controlled Retrieval Eq. (4.27) in a Circular Orbit, $K_\alpha = 1$, $K_\gamma = 27$; $c = -0.5$; $\ell_i = 100$ km, $\ell_f = 0.1$ km; $\alpha(0) = \alpha'(0) = 0$, $\gamma(0) = 0.1$ deg, $\gamma'(0) = 0$

Chapter 5

Conclusions

5.1 Summary of the Findings

This thesis has examined the three-dimensional librational dynamics of two-body tethered satellite systems, mainly through a modern nonlinear dynamics approach.

The governing pitch and roll equations of motion are highly nonlinear. Hence, both numerical and approximate analytical methods have been used to analyze these equations. Primarily, numerical tools of nonlinear dynamics analysis have been used: phase plane plots, time histories, Poincaré sections, PSD's and Lyapunov exponents were constructed from numerical integration of the equations of motion. The analytical method of Melnikov, as well as classical approximate methods of solution, have also been applied.

The stationkeeping phase as well as the deployment and retrieval phases have been studied. The dynamical model considers a system of two point masses connected by a rigid tether, in a Keplerian orbit, and ignores aerodynamic effects. The tether is considered to have negligible mass in the variable length analyses.

Motion in the stationkeeping phase, in which the tethered system is just a gravity gradient pendulum. was analyzed first considering only pitch dynamics. and then considering both pitch and roll degrees of freedom. for both the circular and elliptic orbit cases.

In the stationkeeping phase the behaviour can be understood from Hamiltonian nonlinear dynamics. In a near-integrable Hamiltonian system the phase space and surface of section is made up of regular (periodic or quasi-periodic) and chaotic regions of motion. The chaotic layers exist near the separatrices associated with the resonances of motion and grow with increasing perturbation away from integrability.

In the case of planar motion and a circular orbit. the system is integrable and the motion is entirely regular. It was shown that periodic libration and tumbling solutions exist. separated by separatrices in the phase plane.

For planar motion. nonzero eccentricity case. Poincaré sections showed that a chaotic tumbling region appears to grow from the separatrices of the circular orbit case. this region growing with increasing eccentricity. For smaller initial conditions. the solutions are those of regular libration.

In the case of coupled motion. for a circular orbit. the region of possible motion in the phase space and surface of section is dependent on the Hamiltonian constant C_H. For a given C_H. the nature of motion depends on the mix of initial conditions. Surfaces of section showed that as C_H was increased. the region of possible motion changed from mainly regular libration. to regular and chaotic libration. to regular libration along with regular and chaotic tumbling. For trajectories starting from rest with equivalent initial pitch and roll angles. a series of Poincaré sections. PSD's. and Lyapunov exponents were presented to document a change from regular to chaotic motion. and subsequent increase in the degree of chaotic motion. as the angle is increased.

If roll is assumed to be small and harmonic, the system can be considered as a perturbation of the integrable, planar system. Melnikov's method applied to this idealized version of the coupled system, showed that such a system will always have chaotic motion near the separatrix.

For the coupled motion, nonzero eccentricity case, the numerical techniques were applied to examine the nature of motion of libration trajectories starting from rest with equivalent initial pitch and roll angles, for an orbit of a specified eccentricity. Librations change from regular motion to weakly chaotic motion as the initial angles are increased. The phenomenon of Arnold diffusion, predicted in this system by theory, was not observed for the chaotic trajectories and time frame studied.

Eccentricity and out-of-plane motion reduced the size of the observed region of regular libration solutions; they introduce additional resonances and chaotic solutions to the phase space.

Chaotic libration, observed in the coupled motion cases, limits the regular libration region to a region smaller than just the libration region of non-tumbling motion. Therefore in terms of determining the desirable region of operation of the system, it is important to consider the nature of motion (regular or chaotic motion).

The variable length case (deployment and retrieval) was studied next. Planar motion in a circular orbit was first considered. For an exponential length rate, linear analysis about the fixed points and phase planes showed that the system is stable when stable foci or nodes exist: deployment is stable only for exponential length rate constant $0 < c < 3/4$, while retrieval is unstable for all values of length rate $c < 0$. For the unstable values of c, the exponential length rate scheme was compared to an equivalent uniform length rate scheme, where a given length change is completed in an equal amount of time in both schemes, using time histories and phase planes. The uniform case remained stable for $c \geq 3/4$ and showed slower growth in motion for $c < 0$. and is thus preferable regarding motion growth.

Application of Melnikov's method to the planar motion of slow exponential deployment in a slightly elliptic orbit, showed that chaotic separatrix motion occurs only for eccentricity greater than a determined critical value e_{cr}, which is proportional to c: deployment introduces dissipation into the system which has a regularizing effect.

Finally, the thesis examined the coupled motion of retrieval in a circular orbit under a given length rate control law, involving linear feedback of pitch rate and quadratic feedback of roll rate. The pitch and roll limit cycle response characteristics were determined by approximate analytical methods of solution: for specified system parameters the values predicted compared well with those of the actual response as obtained from numerical simulation.

In summary, the thesis shows that the tethered satellite systems have very rich dynamical behaviour due to the nonlinearity of the governing equations, understanding of which may help in mission design and planning.

5.2 Recommendations for Future Work

The material presented in this work covered only a part of the nonlinear dynamics of tethered satellite systems. Some recommendations for future work are given below.

- Extend the numerical analysis of the regular libration region for the stationkeeping, coupled motion, elliptic orbit case to more general initial conditions and eccentricities.

- Investigate numerically the occurrence of chaos in the exponential deployment, planar motion, elliptic orbit case.

- Study the phase space of the coupled motion of controlled retrieval further.
- Apply approximate analytical methods to predict the limit cycle response characteristics for the retrieval length rate control law involving absolute value, rather than quadratic, out-of-plane feedback.
- The present work ignored the elastic vibrations of the tether. Investigate the nonlinear dynamics for the case of a *flexible* tether.
- Investigate the nonlinear dynamics of multi-body tethered satellite systems.
- Carry out experimental or flight verification of the dynamical behaviour predicted in the thesis.

Bibliography

[1] Baker, W. P., Dunkin, J. A., Galaboff, Z. J., Johnston, K. D., Kissel, R. R., Rheinfurth, M. H. and Siebel, M. P. L. (1976). "Tethered Subsatellite Study," *NASA TMX* -73314.

[2] Bekey, I. (1983). "Tethers Open New Space Options," *Astronautics and Aeronautics* **21**(4), 32–40.

[3] Beletskii, V. V., and Levin, E. M. (1993). "Dynamics of Space Tether Systems", *Advances in the Astronautical Sciences*, **83**.

[4] Benettin, G., Galgani, L., Giorgilli, A. and Strelcyn, J.-M. (1980). "Lyapunov Characteristic Exponents for Smooth Dynamical Systems and for Hamiltonian Systems: A Method for Computing all of Them. Part 2: Numerical Application," *Meccanica*, March, 21-30.

[5] Brereton, R.C., and Modi, V. J. (1967). "Stability of the Planar Librational Motion of a Satillite in an Elliptic Orbit," *Proc. of the XVII Inter. Astronautical Congress*, Gordon and Breach Science Publishers, New York, 179-192.

[6] Cole, J. W. and Calico, R. A. (1992). "Nonlinear Oscillations of a Controlled Periodic System," *Journal of Guidance, Control, and Dynamics* **15**(3), 627–633.

[7] Colombo, G., Gaposchkin, E. M., Grossi, M. D., and Weiffenbach, G. C. (1974). "Shuttle-Borne Skyhook: A New Tool for Low-Orbital-Altitude Research." *Smithsonian Astrophysical Observatory* report.

[8] Contopoulos, G., Galgani, L. and Giorgilli, A. (1978). "On the number of isolating integrals in Hamiltonian systems." *The American Physical Society* **18**(3), 1183-1189.

[9] Fleurisson, E. J., von Flotow, A. H., and Pines, D. J. (1993). "Trajectory Design, Feedforward, and Feedback Stabilization of Tethered Spacecraft Retrieval." *Journal of Guidance, Control and Dynamics* **16**(1), 160–167.

[10] Gray, G. L. and Stabb, M. C. (1993). "Chaos in Controlled, Gravity Gradient Satellite Pitch Dynamics via the Method of Melnikov, Part 1 – Center Stabilization." *AAS/AIAA Spaceflight Mechanics Meeting*, Pasadena, California, Paper No. AAS-93-132.

[11] Grossi, M. D. (1986). "Historical Background Leading to the Tethered Satellite System (TSS)." *AIAA 24th Aerospace Sciences Meeting*, Reno, Nevada, Paper No. 86-0048.

[12] Guckenheimer, J., and Holmes, P. J. (1983). *Nonlinear Oscillations, Dynamical Systems and Bifurcations of Vector Fields*. Springer-Verlag, New York.

[13] Guran, A. (1993). "Chaotic Motion of a Kelvin Type Gyrostat in a Circular Orbit." *Acta Mechanica* **98**, 51–61.

[14] Henon, M., and Heiles, C. (1964). "The Applicability of the Third Integral of Motion: Some Numerical Experiments." *Astronomical Journal* **69**(1), 73-79.

[15] Hughes, P. C. (1986). *Spacecraft Attitude Dynamics*. John Wiley and Sons, New York.

[16] Karasopoulos, H. and Richardson, D. L. (1992). "Chaos in the Pitch Equation of Motion for the Gravity-Gradient Satellite." *AIAA/AAS Astrodynamics Conference*. Hilton Head, South Carolina, Paper No. AIAA-92-4369.

[17] Karasopoulos, H. A., and Richardson, D. L. (1993). "Numerical Investigation of Chaos in the Attitude Motion of a Gravity-Gradient Satellite." *AAS/AIAA Astrodynamics Specialist Conference*. Victoria, B.C., Paper No. AAS-93-581.

[18] Koch, B. P. and Bruhn, B. (1989). "Chaotic and Periodic Motions of Satellites in Elliptic Orbits." *Zeitschrift für Naturforschung A* **44A**(12), 1155–1162.

[19] Lang, D. L., and Nolting, R. K. (1967). "Operations with Tethered Space Vehicles." *NASA* SP-138, Gemini Summary Conference.

[20] Lichtenberg, A. J., and Lieberman, M. A. (1992). *Regular and Chaotic Dynamics*. Applied Mathematical Sciences **38**, Springer-Verlag, New York.

[21] Lin, W. A., and Reichl, L. E. (1985). *Physical Review*, A31, 1136.

[22] Melvin, P. J. (1988a). "The Figure–of–8 Librations of the Gravity Gradient Pendulum and Modes of An Orbiting Tether." *Quarterly of Applied Mathematics* **XLVI**(4), 637–663.

[23] Melvin, P. J. (1988b). "The Figure–of–8 Librations of the Gravity Gradient Pendulum and Modes of An Orbiting Tether: II. Geodetic, Mass Distribution, and Eccentricity Effects." *AIAA/AAS Astrodynamics Conference*. Minneapolis, Minnesota, Paper No. AIAA-88-4283-CP.

[24] Misra, A. K. and Modi, V. J. (1987). "A Survey on the Dynamics and Control of Tethered Satellite Systems." *Tethers in Space. Advances in the Astronautical Sciences* **62**, 667-720.

[25] Modi, V. J. and Brereton, R. C. (1968). "The Stability Analysis of Coupled Librational Motion of An Axi-Symmetric Satellite in a Circular Orbit." *Proceedings of the XVIII International Astronautical Congress*, Pergamon Press, London, 109-120.

[26] Modi, V. J., and Brereton, R. C. (1969a). "Periodic Solutions Associated with the Gravity-Gradiant Oriented System. Part I: Analytical and Numerical Determination." *AIAA J.* **7**, 1217-1225.

[27] Modi, V. J., and Brereton, R. C. (1969b). "Periodic Solutions Associated with the Gravity Gradiant Oriented System. Part I: Stability Analysis." *AIAA J.* **7**, 1465-1468.

[28] Modi, V. J., Chang-Fu, G., Misra, A. K. and Xu, D. M. (1982). "On the Control of the Space Shuttle Based Tethered Systems." *Acta Astronautica*, Vol. 9, June–July, pp. 437–443.

[29] Modi, V. J., and Shrivastava, S. K. (1971a). "Effect of Inertia on Coupled Librations of Axi-Symmetric Satellites in Circular Orbits." *C.A.S.I. Transactions* **4**(1), 32-38.

[30] Modi, V. J., and Shrivastava, S. K. (1971b). "Librations of Gravity-Oriented Satellites in Elliptic Orbits through Atmosphere." *AIAA J.* **9**(11), November, 2208-2216.

[31] Modi, V.J., and Shrivastava, S.K. (1972), "On the Limiting Regular Stability and Periodic Solutions of a Gravity System in the Presence of the Atmosphere." *C.A.S.I. Transactions*, **5**(1), March, 5-10.

[32] Monshi, N. (1992), "Three–dimensional Librational Dynamics and Control of Multi-body Tethered Satellite Systems," Master's Thesis, Department of Mechanical Engineering, McGill University, Montreal, Canada.

[33] Monshi, N., Misra, A., and Modi, V. J. (1991), "On the Reel Rate Control of Retrieval Dynamics of Tethered Satellite Systems", *Spaceflight Mechanics 1991, Advances in the Astronautical Sciences* **75**, 1053-1075.

[34] Moon, F. C. (1992), *Chaotic and Fractal Dynamics: An Introduction for Applied Scientists and Engineers*, John Wiley and Sons, Inc., New York.

[35] Nayfeh, A. H., and Mook, D. T. (1979), *Nonlinear Oscillations*, John Wiley and Sons, New York.

[36] Penzo, P. A., and Ammann, P. W. (1989), *Tethers in Space Handbook*, Second Edition, NASA, Office of Space Flight, Advanced Program Development, NASA Headquarters, Washington, DC.

[37] Percival, I.C. (1987), "Chaos in hamiltonian systems." *Proceedings of the Royal Society of London*, **A**(413), 131-144.

[38] Rasband, S. N. (1990), *Chaotic Dynamics of Nonlinear Systems*, John Wiley and Sons, New York.

[39] Reichl, L. E. (1992), *The Transition to Chaos In Conservative Classical Systems: Quantum Manifestations*, Springer–Verlag, New York.

[40] Seisl, M. and Stendl, A. (1989). "The Chaotic Vibrations of Satellites." *Zeitschrift für angewandte Mathematik und Mechanik* **69**(5), 352–354.

[41] Starly, W. H., and Adlhoch, R. W. (1963). "Study of the Retrieval of an Astronaut from an Extra-Vehicular Assignment." *TMC* Report No. S-356, The Marquardt Corporation, Van Nuys, California.

[42] Tabor, M. (1989). *Chaos and Integrability in Nonlinear Dynamics*, John Wiley and Sons, New York.

[43] Tong, X. and Rimrott, F. P. J. (1991a). "Numerical Studies on Chaotic Planar Motion of Satellites in an Elliptic Orbit." *Chaos, Solitons & Fractals* **1**(2), 179–186.

[44] Tong, X. and Rimrott, F. P. J. (1991b). "Some Observations of Chaotic Motion of Satellites with Damping in an Elliptic Orbit." *Proceedings of 13th CANCAM*, Winnipeg, Canada, 750–751.

[45] Tong, X. and Rimrott, F. P. J. (1993). "Chaotic Planar Motion of Satellites with Damping in an Elliptic Orbit." *Proceedings of 14th CANCAM*, Winnipeg, Canada, 783–784.

[46] Tsiolkovsky, K. E. (1895). (reprinted in 1959). "Speculations Between Earth and Sky." Isd-vo AN-SSSR, Moscow, 35.

[47] von Tiesenhausen, G. (1984). "Tethers in Space - Birth and Growth of a New Avenue to Space Utilization." *NASA* TM-82571, Marshall Space Flight Center.

[48] Wiggins, S. (1988). *Global Bifurcations and Chaos*, Springer–Verlag, New York.

[49] Wiggins, S. (1990). *Introduction to Applied Nonlinear Dynamical Systems and Chaos*, Texts in Applied Mathematics Series, Vol. 2, Springer–Verlag, New York.

[50] Xu, D. M. (1984). "Dynamics and Control of Shuttle Supported Tethered Satellite Systems." Ph.D. Thesis, Department of Mechanical Engineering, McGill University, Montreal, Canada.

IMAGE EVALUATION TEST TARGET (QA-3)

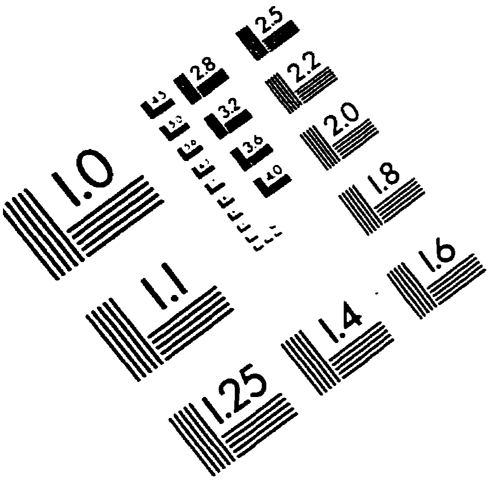

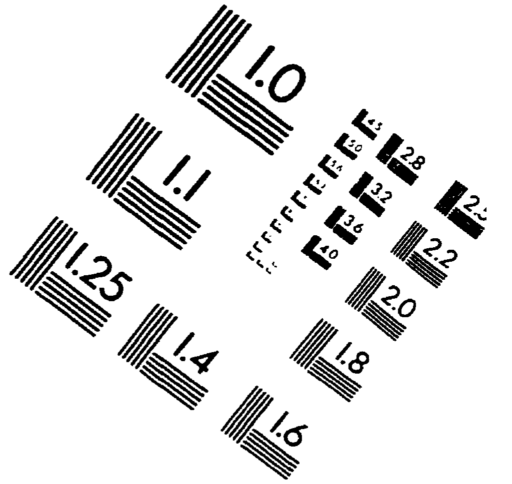

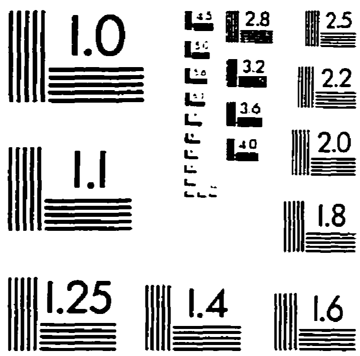

150mm

6″

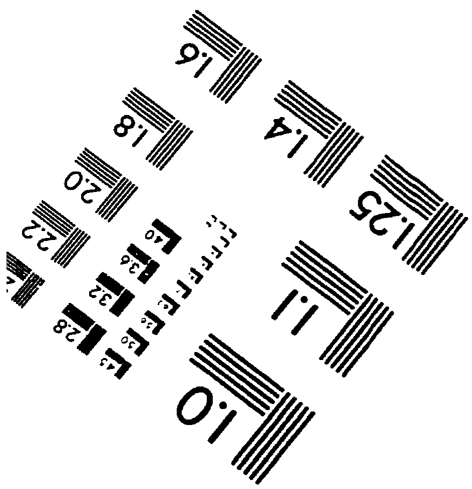

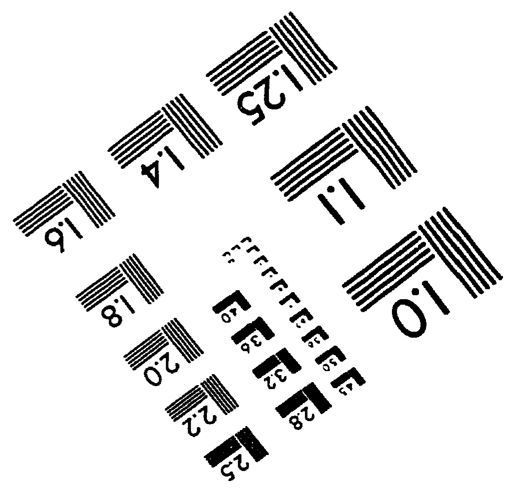

APPLIED IMAGE . Inc
1653 East Main Street
Rochester, NY 14609 USA
Phone: 716/482-0300
Fax: 716/288-5989